Silicon-Micromachined Flow Sensors

Thesis by

Fukang Jiang

In Partial Fulfillment of the Requirements

for the Degree of

Doctor of Philosophy

California Institute of Technology

Pasadena, California

1998

(Submitted July 17, 1997)

© 1998

Fukang Jiang

All rights reserved

To my beloved parents and wife

Acknowledgments

I would like to thank all the people that have supported and helped me during the six years of study and research at Caltech. In particular, I would like to acknowledge my academic advisor, Dr. Yu-Chong Tai. It was Dr. Tai who brought me into this exciting field of micromachining. More importantly, he has provided the key ideas, professional guidance and supports through all these years that made this work successful. I have also received tremendous help and valuable advice from Dr. Chih-Ming Ho, professor at the Department of Mechanical and Aerospace Engineering, University of California at Los Angeles, and the prime investigator of all the research projects involved in this work.

I thank the fellow members of the research project teams at UCLA, especially Dr. Steve Tung and Vincent Lee who gave me numerous help on the sensor characterization and on the understanding of the basic concepts in fluid dynamics. This thesis would not be complete without their efforts. I am also indebted to Wen Li, Karan Rainer and Michael Garstenauer who helped me in using the wind-tunnel at UCLA for the testing of the hot-wire anemometers.

I also thank my research partners in our group, Tom Tsao who has been working closely with me on two projects in the recent two years and proofread most chapters of the thesis, and Ken Walsh, who impressed me with his great photo-taking skill for small samples and helped me in the development of the flexible skins.

I deeply appreciate the past fellow members of our Lab, Drs. Jianqiang Liu, Chang Liu and Raanan Miller, for their many useful help in using the computers, design tools and processing equipment. The same thanks also go to all of the current fellow members of our group, especially Charles Grosjean, Shuyun Wu, Wen Hsieh, John Wright and Xuanqi Wang, and the guests of the group, Drs. Weilong Tang and Hsu-Tseng Yang. I am also grateful to our technician, Mr. Trevor Roper, who maintains all the processing equipment in good condition with his diligence and skill.

My thanks also go to our collaborators in Dr. Rodney Goodman's Microsystem Group at Caltech, Dr. Bhusan Gupta and Vincent Koosh, for the circuit and layout design of the M^3 system.

I would like to thank the Defense Advanced Research Programs Agency (DARPA) and the Air Force Office of Scientific Research (AFOSR) for providing me the financial support in the past four years.

Finally, I would like to thank my wife, Heng Ji, for her support and patience in the preparation of the thesis, and my parents for their constant encouragement over the many years of my education.

Silicon-Micromachined Flow Sensors

By

Fukang Jiang

In Partial Fulfillment of the Requirements

for the Degree of

Doctor of Philosophy

Abstract

A new generation of silicon-micromachined or micro-electro-mechanical-system (MEMS) sensors for the general purpose of microflow measurement and control is presented here. The first one is a polysilicon hot-wire anemometer made by a combined bulk and surface micromachining process. The new devices feature batch-fabricated free-standing micro polysilicon hot wires that are similar to conventional metal hot wires. Both the theoretical analysis and experimental (steady-state and dynamic) results show that MEMS hot wires have order-of-magnitude better frequency response, finer spatial resolution, and higher sensitivity over conventional hot-wire anemometers.

A novel MEMS thermal shear-stress sensor featuring vacuum-cavity insulation has been developed. The device is a polysilicon wire thermistor embedded in a silicon-nitride diaphragm which sits on top of a vacuum cavity. The vacuum cavity is to improve the thermal isolation between the polysilicon wire and substrate. To characterize the devices, both steady-state and transient heat-transfer theories have been established and used to calibrate wind-tunnel results, temperature sensitivities and frequency responses. Shear-stress sensor array chips have also been developed. Each of the shear-stress imagers has more than 100 sensors integrated on a 1×2.85 cm^2 chip. Our measurement results from a fully developed 2-D channel flow are well agreeable with previously published results.

For the first time, real-time 2-D wall shear-stress images in a turbulent flow have been experimentally obtained.

A new technology for the integration of micro-sensors, micro-actuators and microelectronics (M^3) on a single chip has been explored. Prototype M^3 chips including shear-stress sensors, magnetic actuators and CMOS circuits have been fabricated. This technology sets a base for the future development of a fully functional M^3 chip drag reduction.

Finally, a novel flexible MEMS skin technology fully compatible with IC process has been developed. Mechanically, the skin is made of metal leads sandwiched between polyimide layers that connect a number of silicon islands together. The skin can be applied conformablly on non-planar surfaces. The first application of this technology is a flexible shear-stress sensor skin that has been successfully used for the real-time measurement of shear-stress distribution on the leading edge of a delta wing model.

Table of Contents

List of Figures

List of Tables

Chapter 1

Introduction

Fluid flow is important in many fields of engineering, industries and scientific research such as meteorology, astronomy, chemistry, geology and physics. As a result, the interest in fluid mechanics by scientists and engineers has continued to grow throughout many years of study. Recently, the emphasis of interest has changed from that in traditional fluid mechanics. This change is taking place mainly due to two reasons. Firstly, with the development of fast and large-capacity computing technology, numerical methods have become a powerful tool for fluid mechanists. In fact, it has developed to a new field of flow study, the computational fluid dynamics (CFD). Secondly, the microscopic fluid flow study (microfluidics) is rapidly expanding, motivated by the demand from biomedical study and chemical analysis, and made possible by the micromachining technology developed over the past decade [1,2,3,4]. Finally, the active control of fluid flows has recently become a hot topic in fluid mechanics [5,6,7,8], as opposed to the passive control in the past [9,10,11]. This is because of the emerging CFD and also the fast development of available hardware, due to the availability of the microfabrication technology.

1. 1 Fluid Mechanics Measurements

Some form of flow measurements are always required to improve our understanding of the physical processes in turbulent and three-dimensional flow systems, as well as to determine the flow quantities needed in a variety of industrial applications. Even the advent of sophisticated numerical methods in CFD for studying and predicting turbulent flow has not diminished the requirement for flow measurement, but rather enhanced this

need because the development of turbulence models still requires much experimental input and eventually verification in many different flows.

Many different flow parameters are required to describe fluid flows. The most important ones are pressure, p, and flow velocity, U. From these two parameters, many other physical parameters can be computed for a single-phase flow. For example, the lift force is a function of pressure; the surface shear stress is proportional to the normal gradient of the flow velocity on the surface; the volumetric flow rate is the integral of the flow velocity over a cross-sectional area. This is probably why pressure sensors and flow velocimeters (hot-wire and hot-film anemometers, Laser-Doppler Velocimeter) are the most widely used instruments in fluid mechanics measurement.

In reality, however, measurement of the spatial and temporal distribution of pressure and velocity is complicated and sometimes, not possible. Meanwhile, this type of measurement and correlation is not always necessary in order to know a specific physical parameter. For example, it is possible to perform shear stress and volume flow rate measurements without knowing the flow velocity field. This is why there exist many other instruments besides pressure sensors and flow velocimeters such as shear stress sensors and flow meters.

1.2 Flow Control

1.2.1 Basic Fluid Mechanics Concept

Some basic fluid mechanics notations that are used in this section and throughout the thesis are briefly explained here.

Laminar and Turbulent Flow In laminar flow, fluid particles move very smoothly parallel to each other. There is basically no mixing between different layers of fluids. Therefore, a dye stream injected in a laminar flow field would move in a thin line. Low velocity flow in a smooth channel is usually laminar.

Turbulent flow is an irregular condition of flow in which fluid particles move randomly and the various quantities show a random variation with time and space coordinates, so that statistically distinct average values can be discerned [12]. Usually turbulent flow occurs at high velocity. Much effort has been spent in the study of this difficult topic in fluid mechanics. For example, computational fluid dynamics has been introduced to study and predict turbulence. In addition, experimental methods are also used to investigate the turbulence structures and explore the possibility of turbulence manipulation.

Boundary Layer and Shear Stress Boundary layer is defined as the thin layer of viscous fluid adjacent to the solid surface which has a velocity shear. The velocity u is zero at the surface and increases with increasing distance (y) from the surface. The boundary layer thickness δ is defined as the normal distance from the surface to a point where the local fluid velocity is 99% of the free stream velocity. Boundary layers are thinner at the leading edge of a flat plate or the entrance of a pipe and thicker toward the trailing edge. Flow in boundary layers is generally laminar at the leading or upstream portion and turbulent in the trailing or downstream portion. Inside the turbulent boundary layer, there is an extremely thin layer of fluid attached to the surface called the viscous sub-layer in which the velocity distribution in direction normal to the surface is linear.

The shear stress in laminar flow is defined as

$$\tau = \mu \left.\frac{\partial u}{\partial y}\right|_{y=0} \tag{1.1}$$

and the shear stress in turbulent flow is defined as

$$\tau = (\mu + \rho\varepsilon) \left.\frac{\partial u}{\partial y}\right|_{y=0} \tag{1.2}$$

where ε is the eddy viscosity. The shear stress in turbulent is higher than that in laminar flow not only because of the eddy viscosity, but also because of the high velocity gradient in the viscous sub-layer.

Reynolds Number In discovering the difference between laminar and turbulent flows in 1883, Osborne Reynolds noted that the quality of the flow in a pipe of diameter D depended on the dimensionless parameter UD/ν, where U is the average fluid velocity, $\nu \equiv \mu/\rho$ is the kinematic viscosity, μ is the dynamic viscosity, and ρ is the density of the fluid. More generally, the Reynolds number is defined as

$$\mathbf{Re} = \frac{Ul}{\nu} \tag{1.3}$$

where l is the characteristic length scale. In a pipe flow, the flow is usually turbulent for **Re** > 2000. In flow over a flat plate, when the plate length is taken as the characteristic length, the transition from laminar to turbulent commonly occurs at $3\times10^5 < \mathbf{Re} < 6\times10^5$. Two flows are considered to be similar if their Reynolds numbers are identical in a geometrically similar, incompressible (ρ = constant) pipe flow.

Flow Separation For a flat plate submerged in a flow, the boundary layer remains attached to the surface and grows throughout its length. However, this is not always the case when the fluid path is oblique to the surface [13]. For example, for the blunt-nosed body of Figure 1.1(a) the boundary layer detaches, separating from the surface at the up-stream end and produce a wake, while for the round-nosed body of Figure 1.1(b), the boundary layer remains attached to the surface. The airfoil of Figure 1.1(c) experiences accelerating flow from point *A* to *B* and deceleration from point *B* to the trailing edge. At point *C*, known as the separation point, the velocity gradient is zero, i.e.,

$$\left.\frac{\partial u}{\partial y}\right|_{y=0} = 0 \tag{1.4}$$

and the flow actually reverses in direction between point *C* and *D*. The corresponding pressure gradients shown in the figure come from the Bernoulli's equation in potential flow theory. Separation can only occur in decelerating flow. Beyond the separation point the pressure gradient is said to be adverse. From Eq. (1.1), one would conclude that the shear stress at a separation point is zero. However, this is true only in two-dimensional

flow. For three-dimensional flow, the shear stress usually has a local minimum at the separation point, because there may still be a gradient of the velocity component in the second dimension.

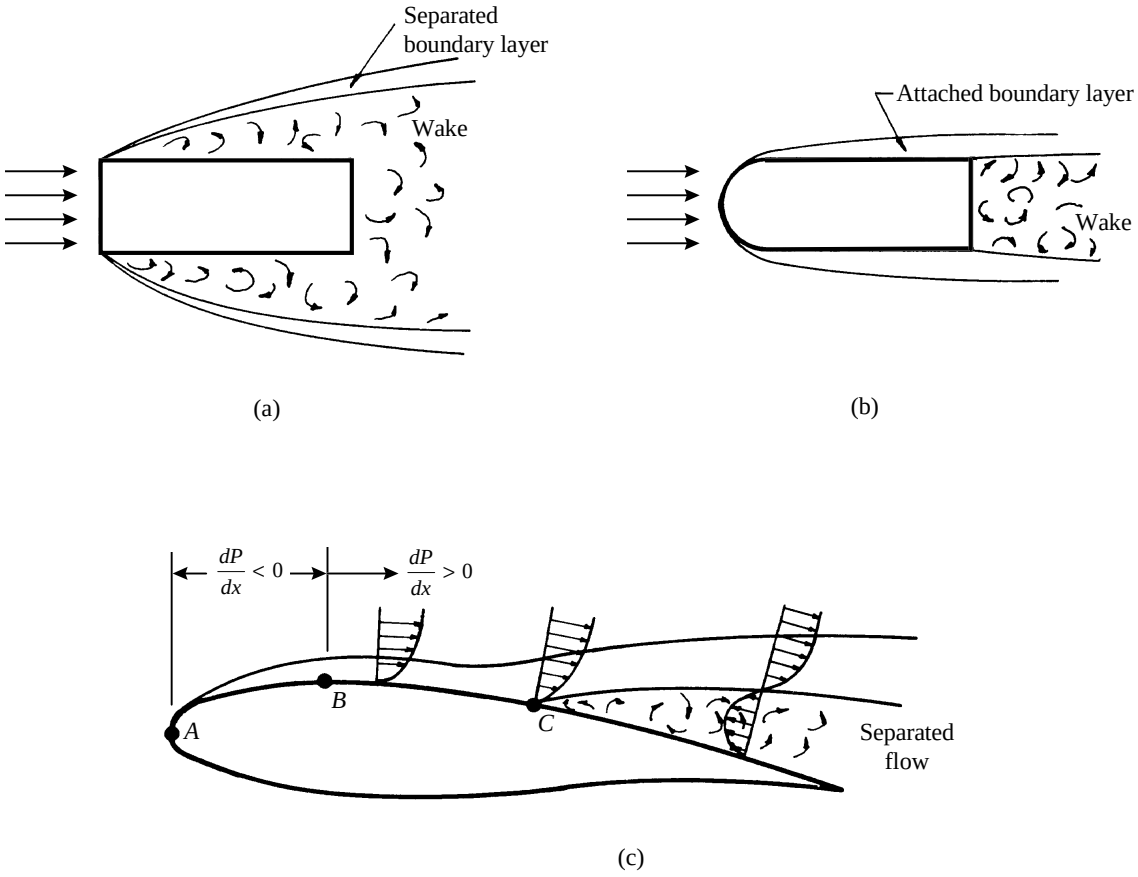

Figure 1.1 Flow over (a) blunt-nosed body, (b) round-nosed body and (c) airfoil.

1.2.2 Flow Control

Flow control is currently attracting increased attention in connection with a variety of applications. In flow control application one may want to destabilize the flow, in order to achieve better mixing, or to stabilize the flow in order to eliminate undesirable unsteady loads. Several studies have appeared on the subject, and one can classify the techniques used into two major categories: passive control, in which flow control is achieved by

altering the geometry of the flow; and active control, in which a time-dependent forcing is applied to the flow, by means, for instance, of a loudspeaker.

Passive control can suppress unsteadiness in a flow [14,15,16]. In practical application, however, no matter how careful the design is, flow separation and unsteadiness behind moving bodies are often unavoidable because of maneuvering motion, or encountering ambient turbulence.

Active control can be divided into open-loop schemes, in which the forcing is a prescribed function of time, and closed-loop schemes, in which the forcing is a function of some real-time measurement of the response of the flow. Open-loop schemes rely on an accurate knowledge of the basic fluid mechanics of the problem in order to prescribe the appropriate forcing function for the controller [17]. In closed-loop schemes, on the other hand, a sensor is placed in the flow field, and its output, after going through a controller, is fed back into the actuator [18]. Closed-loop schemes thus do not necessarily require the detailed knowledge of fluid mechanics that open-loop schemes do. However, in addition to the issue of closed-loop stability, the very important question of observability of the flow remains open. In fact, Roussopoulos [19] recently presented convincing evidence that, when a single sensor is used, the flow is not observable, in the sense that unsteady patterns are present without being detected by the sensor. Therefore, in order to perform closed-loop active control, it is essential to have a large number of sensors for the detection of flow patterns.

1.3 MEMS and Its Application in Fluid Mechanics

The emerging micro-electro-mechanical system (MEMS) technology has been used to fabricate mechanical structures in micrometer scales, such as beams, diaphragms, grooves, orifices, sealed cavities, pyramids, needles, springs, gears, joints and motors. It provides us with micro-sensors and micro-actuators which match the length scales of the investigated phenomena in the exploration of all areas of science so that enough spatial resolution can be achieved for sensing and effective momentum and energy transfer to the

controlled subjects can be accomplished for actuation. Furthermore, these miniature transducers can be integrated with microelectronics to complete the loop of sensing, information processing, actuation and sensing on a single chip. This type of mass-producible systems enables us to perform real-time control of time-varying events common in fluid dynamics.

The basic MEMS fabrication techniques includes bulk and surface micromachining, wafer bonding and micromolding (LIGA). Detailed information about MEMS fabrication techniques can be found in many excellent reviews papers [20,21]. Here, silicon bulk and surface micromachining technologies are briefly introduced because they will be used throughout the thesis. Moreover, the materials commonly used in these technologies and the compatibility issue of the MEMS processes with microelectronics will be discussed. Finally the potential MEMS applications in fluid mechanics are listed.

1.3.1 Silicon Micromachining

Si micromachining technology is dominant in the fabrication of MEMS devices because of its similarity with the Si microelectronics fabrication technology. As a matter of fact, it is regarded as being derived from IC technology. Historically, Si micromachining is divided into two categories, bulk and surface micromachining.

Bulk Micromachining Silicon bulk micromachining uses wet and dry silicon etching techniques, with etch masks and etch stops, to sculpt mechanical devices from a silicon wafer. The mixture of hydrofluoric acid, nitric acid and acetic acid (HNA) is an isotropic silicon etchant with silicon nitride as the etch mask. Certain other chemicals, such as ethylene-diamine-pyrocatechol with water (EDP or EPW), tetramethyl ammonium hydroxide (TMAH), hydrazine solution and potassium hydroxide (KOH) solution, etches in (100) and (110) silicon crystallographic directions much faster than in the (111) direction, which allows the design of microstructures to be naturally bounded by {111} crystalline planes. Silicon dioxide and silicon nitride generally have very low etch rate in these anisotropic etchants and make good etch masks. The vertical etch stop can be heavily boron-doped layer buried under epitaxial layer, silicon dioxide in SIMOX wafers

and p-n junction (for electrochemical etching). It is generally agreed that Si bulk micromachining using wet chemical etching is a mature technology and many Si microstructures including beams, diaphragms, nozzles, etc. have been made. These microstructures have formed the building blocks of many MEMS devices.

Nevertheless, there are some disadvantages for bulk micromachining using wet anisotropic etching. For example, the geometry that can be made by are generally limited by the silicon crystalline orientations; bulky corner compensation structures are often needed in order to make convex structures such as beams; the choices of etch masks are extremely limited. In contrast, dry etching processes do not have these problems and have recently attracted more attention. These include laser drilling, reactive ion etching (RIE), ion milling and even micro electro-discharge-machining (EDM).

Surface Micromachining In silicon surface micromachining, microstructures are fabricated on the surface of the Si substrate by consecutive deposition and patterning of thin-film structural and sacrificial layers. The Si substrate, however, only serves as a mechanical support and usually does not participate in the processing. At a certain stage, the sacrificial layers are removed by wet or dry etching that does not attack the structural layers. Silicon dioxide is the most often used sacrificial materials, while polysilicon and some metals are occasionally used as sacrificial materials. The most common structural materials are polysilicon and silicon nitride.

1.3.2 Integration with IC

The integration of MEMS devices with IC has many advantages. First, it can greatly reduce the total number of external electrical leads. This is especially important for a distributed control system where a large number of sensor arrays are involved. Second, on chip electronics reduces the electromagnetic interference from outside and parasitic effects from the external leads. Finally, since integration is a batch fabrication process, it saves time and reduces the production cost.

The integration of MEMS devices with IC is also very challenging because they usually do not share the same fabrication process. It requires careful design of the whole

fabrication process to ensure good compatibility. Major considerations should be on the sequence of the processing steps, effect of high temperature post-processing on the electronics, protection of fabricated devices during the fabrication of other types of devices and the effect of surface profile of fabricated devices on the fabrication of other types of devices.

1.3.3 MEMS in Fluid Mechanics

Many MEMS devices have been developed in the past decade for fluid flow study, including pressure sensors and various types of flow sensors. Among them, Si piezoresistive pressure sensors have been successfully used in fluid mechanics measurements. Other devices, such as MEMS anemometers developed by other researchers, do not have comparable performances as their conventional counterparts. This does not mean that MEMS technology is not suitable for fluid mechanics. It only implies that more effort needs to be put in their development. In fact, MEMS technology can be used to solve the most difficult problems in fluid mechanics such as flow control [22,23,24,25]. The reason is twofold. First, the flow structures are generally small. As we pointed out earlier, length scale matching between the transducers used and the investigated phenomena is essential. Therefore, the transducers used in flow control have to be small. Second, the capability of providing large numbers of sensors and actuators by MEMS technology allows us to perform active distributed control, which is the only effective way of flow control due to the distributive nature of the flow. This potential, however, remains to be explored.

1.4 Overview of Chapters

Chapter 2 describes the design and fabrication of micromachined polysilicon hot-wire anemometers. These hot wires have the same basic structure as that of a conventional hot wire, but with greatly reduced dimensions. They are different from many existing surface mount micromachined hot-wires which can only be used to measure the velocity a few

microns above the surface. Many performances including the sensitivity and frequency response are improved. More importantly, they are batch-fabricated and mass-producible, as compared to the painstaking manual fabrication of conventional hot wires. A thorough calibration has been presented to validate the use in flow velocity measurement.

Chapter 3 presents the design and fabrication of the vacuum-isolated flush-mounted hot-film shear-stress sensor. Detailed heat transfer analysis for this special structure combined with calibration results has clarified the applicable dynamic range of the sensor. The theoretical model also points out possible improvement on the performances of this type of sensors.

As a demonstration of the application of the micromachined shear stress sensors, we have fabricated an array of such sensors to map out the wall shear stress distribution in a fully-developed 2-D channel flow. The use of the shear stress sensor array for underwater measurement has also been explored. These are all presented in Chapter 4.

Chapter 5 is dedicated to the integration of the shear stress sensors, micromachined micro-actuators and the CMOS control electronics for turbulent flow drag-reduction study. Emphasis is on the compatibility of the processing steps for the shear stress sensor with those for the other two types of devices.

Chapter 6 describes our effort on the development of a new microfabrication technology that enables the integration of MEMS devices, including CMOS electronics, on a flexible polyimide skin. The major lead failure that occurred in previously-reported technologies has been eliminated through the proper shaping of Si islands. Moreover, Si islands as small as 100 μm can be defined with good accuracy, which allows the skins to be applied on small surfaces with large curvatures. The first application of this technology in aerodynamics has produced a flexible shear stress sensor array that was used for the real-time measurement of the shear stress distribution on 3-D surfaces.

Bibliography

[1] S. C. Terry, J. H. Jerman, and J. B. Angell, "A Gas Chromatographic Air Analyzer Fabricated on a Si Wafer," *IEEE Trans. Electron. Devices*, Vol. ED-26, pp. 1880-1886, 1979.

[2] J. Liu, Y. C. Tai, K. C. Pong, and C. H. Ho, "Micromachined Channel/Pressure Sensor Systems for Microflow Study," *Tech. Digest 7th Int. Confer. Solid-State Sensors & Actuators (Transducer' 93)*, Yokohama, Japan, pp. 995-997, 1993.

[3] P. Gravesen, J. Branebjerg, and O. S. Jensen, "Microfluidics - a Review," *Proc. MME' 93*, 1993.

[4] E. B. Arkilic, M. A. Schmidt, and K. S. Breuer, "Gaseous Flow in Microchannels," *ASME Application of Microfabrication to Fluid Mechanics, 1994 Int. Mech. Eng. Congress and Expo.*, Chicago, pp. 57-66, 1994.

[5] P. Moin, J. Kim, and H. Choi, "On the Active Control of Wall-Bounded Turbulent Flows," AIAA Paper 89-0960, 1989.

[6] P. R. Bandyopadhyay, "Development of a Microfabricated Surface for Turbulence Diagnostics and Control," *ASME Application of Microfabrication to Fluid Mechanics, 1994 Int. Mech. Eng. Congress and Expo.*, Chicago, pp. 67-74, 1994.

[7] B. F. Farrell, P. J. Ioannou, "Turbulence Suppression by Active Control," *Phys. Fluids*, Vol. 8 (5), pp. 1257-1268, 1996.

[8] H. A. Carlson and J. L. Lumley, "Active Control in the Turbulent Wall Layer of a Minimal Flow Unit," *J. Fluid Mech.*, Vol. 329, pp. 341-371, 1996.

[9] S. R. Park and J. M. Wallace, "Flow Alteration and Drag Reduction by Riblets in a Turbulent Boundary-Layer," *AIAA J.*, Vol. 32 (1), pp. 31-38, 1994.

[10] P. Vukoslavcevic, J. M. Wallace, and J. L. Balint, "Viscous Drag Reduction Using Streamwise-Aligned Riblets," *AIAA J.*, Vol. 30 (4), pp. 1119-1122, 1992.

[11] B. Lazos and S. P. Wilkinson, "Turbulent Viscous Drag Reduction with Thin-Element Riblets," *AIAA J.*, Vol. 26 (4), pp. 496-498, 1988.

[12] J. Hinze, *Turbulence*, 2nd ed., MacGraw-Hill, 1975.

[13] D. R. Pitts and L. E. Sissom, *Heat Transfer*, McGraw-Hill, 1977.

[14] Y. Y. Chen and J. T. Templin, "Suppression of Spatial Waves by Distortion of Jet Velocity Profile," *Phys. Fluids*, Vol. 17, pp. 2124-2125, 1974.

[15] M. M. Zdravkovich, "Review and Classification of Various Aerodynamic and Hydrodynamic Means of Suppressing Vortex Shedding," *J. Wind Eng. Indust. Aero.*, Vol. 7, pp. 145-189, 1981.

[16] P. J. Strykowski and K. R. Sreenivasan, "On the Formation and Suppression of Vortex Shedding at Low Reynolds Number," *J. Fluid Mech.*, Vol. 218, pp. 71-107, 1990.

[17] P. T. Tokumaru and P. E. Dimotakis, "Rotary Oscillation Control of a Cylinder Wake," *J. Fluid Mech.*, Vol. 224, pp. 77-90, 1991.

[18] J. E. Ffowcs Williams and B. C. Zhao, "The Active Control of Vortex Shedding," *J. Fluid Struct.*, Vol. 3, pp. 115-122, 1989.

[19] K. Roussopoulos, "Feedback Control of Vortex Shedding at Low Reynolds Number," *J. Fluid Mech.*, Vol. 248, pp. 267-296, 1993.

[20] K. E. Petersen, "Silicon as a Mechanical Material," *Proc. IEEE*, Vol. 70 (5), pp. 420-456, 1982.

[21] L. O'Connor, "MEMS: Microelectromechanical Systems," *Mechanical Engineering*, Vol. 114, pp. 40-47, 1992.

[22] S. A. Jacobson and W. C. Reynolds, "Active Boundary Layer Control Using Mounted Surface Actuators," *Bulletin of American Physical Society*, Vol. 38, pp. 2197-, 1993.

[23] B. L. Smith and A. Glezer, "Jet Vectoring by Synthetic Jet Actuators," *Bulletin of American Physical Society*, Vol. 40, pp. 2025-, 1995.

[24] J. M. McMichael, "Progress and Prospects for Active Flow Control Using Microfabricated Electro-Mechanical Systems (MEMS)," AIAA Paper 96-0306, 1996.

[25] C. H. Ho and Y. C. Tai, “REVIEW: MEMS and Its Application for Flow Control,” *J. Fluid Eng.*, Vol. 118, pp. 437-447, 1996.

Chapter 2

Micromachined Hot-Wire Anemometers

2.1 Introduction

A hot-wire anemometer is a device for measurement of air flow velocity, velocity fluctuation, and sometimes flow direction. In a typical hot-wire anemometer, there is a small-diameter, temperature-sensitive, resistive metal wire which is heated by passing an electric current through it. When exposed to a gas flow, the heated wire loses heat to the flow by convection and its electrical parameters such as voltage change. The velocity of the flow is then correlated to the measurement results of those parameters. Typically, the electrical arrangements are in either a constant current (CC) mode or a constant temperature (CT) mode. The CC mode is easy to implement but the CT mode performs better and hence is widely used. The documented use of hot-wire anemometer can be traced back to more than 80 years ago [1] and numerous forms of hot-wire anemometers have been devised. Nowadays, they are simply the most popular flow instruments used for laboratory fluid mechanics study. The main reason is because of their unique advantages of being simple, small, highly sensitive and relatively inexpensive.

Figure 2.1 shows an example of today's typical hot-wire anemometers used for wind-tunnel flow measurements. A metal wire is welded or soldered to two metal needles that are molded to a probe body. The wire is often made of platinum, tungsten or some special alloy. The size of the wire is about 5 μm in diameter and 1mm in length. It can have a resistance ranging from 10 Ω to 30 Ω and a temperature coefficient of resistance (TCR) about 0.1%/°C at room temperature. Such a wire would normally need a current from 10 to 40 mA to operate and a cut-off frequency of the anemometer in the tens of kHz range is obtainable using high speed electronics [2,3,4,5].

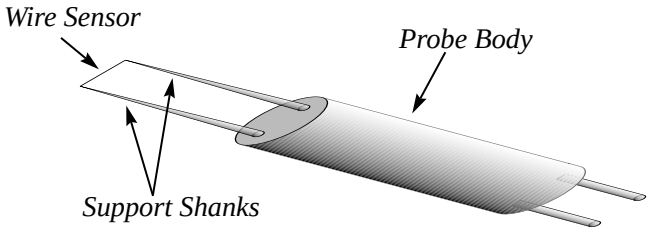

Figure 2.1 Schematic of conventional hot-wire probe.

Nevertheless, there is a major disadvantage of this type of hot wire anemometers; they need to be individually hand-assembled. This also means that it is difficult to build an array of wires for the simultaneous measurements of velocity distribution. In addition, because the wire dimensions do vary significantly, hot-wire probes are often not interchangeable without major re-calibration of the whole instrument.

As a result, to improve hot-wire anemometers, one can then look into three directions. First, future anemometers should be further down-sized. Since the spatial resolution of the anemometers for flow velocity distribution measurement is determined by its dimensions, it is advantageous if the wire size can be further reduced. This would also decrease power consumption and thermal interference to the flow and increase frequency response. However, the traditional technique can no longer make smaller hot wires with reasonable consistency. Second, techniques to build arrayed hot-wires should be developed. Third, new fabrication processes should avoid hand assembly and allow the mass production of the devices. Considering these requirements, our group then has conducted research on applying silicon micromachining technology to the manufacture of smaller and better hot-wire anemometers.

Silicon micromachining is a relatively new technology that is derived from VLSI technology [6] for making micro-electro-mechanical devices [7,8]. This is a proven technology for making chip-type or chip-supported free-standing-wire flow sensors [9,10,11,12]. Interestingly, though, no one has worked on micromachined hot-wire anemometers that possess the optimal features of a free wire in space without anything nearby except the two support shanks so that maximum thermal isolation and minimum

flow disturbance are obtained.

We present our work on the batch-fabricated and further down-sized hot wires that simulate the real structures of a conventional hot wire anemometer. Our hot wires are made with a new process that combines both surface and bulk micromachining technologies [13,14,15], and precisely doped low-pressure-chemical-vapor-deposited (LPCVD) polysilicon is used as the new wire material. Extensive electrical and wind-tunnel characterizations of these devices have been done and it is confirmed that these micron-sized hot wires do have much improved spatial resolution, sensitivity, and frequency response. In the following, we will discuss their design and fabrication, steady-state characteristics, dynamic characteristics, and directional dependency based on our experimental results.

2.2 Design and Fabrication

2.2.1 Structures and Materials

Our micromachined hot-wire anemometers have a structure similar to that of conventional hot-wire anemometers. It consists of a sensing wire, two parallel supports, a Si beam, and the thick Si handle, as shown in Figure 2.2. The Si beam acts as a thermal and mechanical buffer between the supports (0.5 μm thick) and the handle (500 μm thick) to avoid interference with the flow. The sensing wires are about 0.5 μm thick, 1 μm wide, 10-160 μm long, and are free standing to optimize the interaction with the flow and to minimize the thermal conduction to the handle. Heavily doped polysilicon, instead of platinum or tungsten, is used as the sensing and supporting material because of its compatibility with existing micromachining technologies and because of its good electrical and mechanical properties. For example, its Young's modulus is about 165 GPa and its TCR is 0.1-0.2%/^{o}C. The metal leads may extend all the way to the tips of the support shanks to reduce the voltage drop.

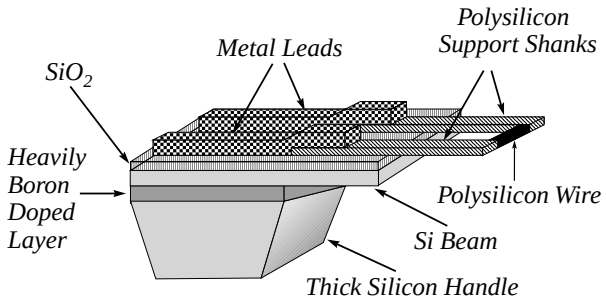

Figure 2.2 Schematic of the micromachined hot-wire probe.

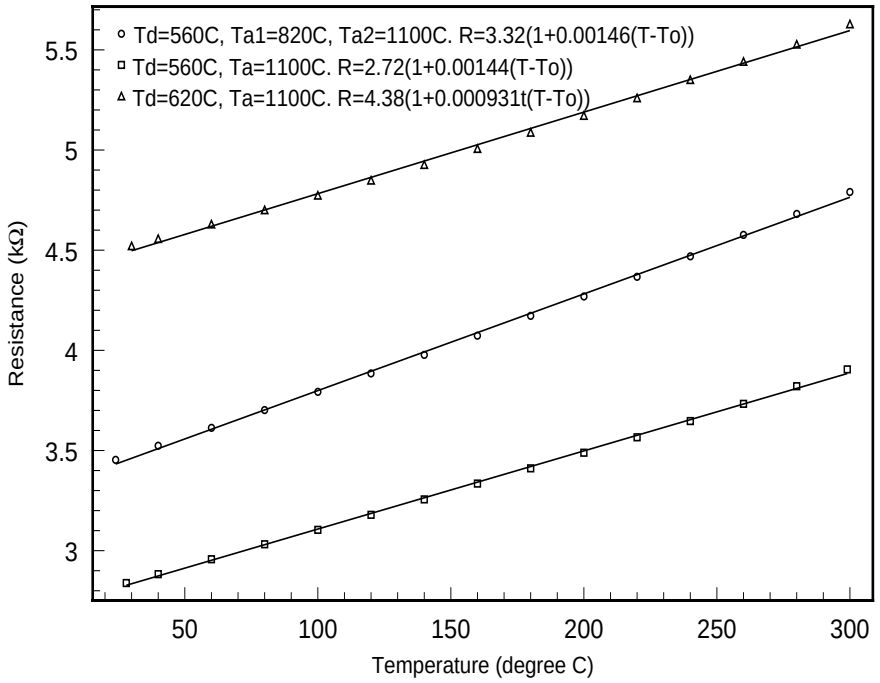

Figure 2.3 The temperature coefficient of boron doped ($2\times10^{20}cm^{-3}$) polysilicon resistors (50 squares) under different deposition and annealing conditions.

It has been reported that polysilicon, deposited in an amorphous state at low temperature and then crystallized at high temperature, has more controllable qualities than as-deposited polysilicon with the deposition temperature at 620^{o}C [16]. We choose to use the former polysilicon, and its electrical properties were calibrated before the fabrication of our anemometers. It is found that the TCR is about 50% higher and the resistance-temperature characteristic is more linear than the normal polysilicon

(deposited at 620^{o}C) at a doping concentration of 2×10^{20} cm^{-3}, as shown in Figure 2.3. Moreover, the stress distribution in this polysilicon along the depth is much more uniform, as we will see from the SEM picture in the discussion section. The calibration results also show that 2×10^{20} cm^{-3} is the doping concentration which gives the lowest sheet resistivity (resistivity divided by film thickness) of 30 Ω/square and highest positive TCR, and therefore, is the optimum doping concentration for hot wires.

2.2.2 Fabrication Process

Two generations of anemometers have been fabricated at the Caltech Micromachining Lab. The first generation has silicon nitride encapsulating the polysilicon wire and support shanks. The polysilicon wires of the second generation are directly exposed to air and consequently the frequency response is improved by an order of magnitude. Figure 2.4 is the simplified fabrication process flow with cross-sections. The detailed process steps are listed in Appendix A.

The fabrication process starts with the deposition of 0.2 μm low-stress silicon nitride and 2 μm low temperature silicon dioxide (LTO) on (100) Si wafers with a 70 μm lightly doped epitaxial layer on top of a 8 μm heavily boron-doped etch stop layer. A 0.6 μm thick amorphous Si layer is deposited at 560^{o}C and doped by boron ion implantation with a dose of 1×10^{16} cm^{-2} at energy of 80 keV. Annealing is done at 1100^{o}C, followed by the patterning of polysilicon by Reactive Ion Etching (RIE). This results in 0.5 μm thick polysilicon resistors with a uniform boron concentration of 2×10^{20} cm^{-3}. After the aluminum or gold metallization, a 3 μm LTO is deposited at 450^{o}C, and the front-side and backside Si substrate windows are opened using both wet and dry (plasma) etchings. A 10 hour EDP anisotropic etching at 95^{o}C removes the Si underneath the polysilicon probe. Finally, RIE etching and pad etchant are used to strip the heavily doped boron layer, nitride and LTO layer respectively. Figure 2.5 shows the SEM pictures of the tips of some hot-wire anemometers fabricated using this process, and Figure 2.6 is the photograph of the tilted devices, which corresponds to the sketch in Figure 2.2.

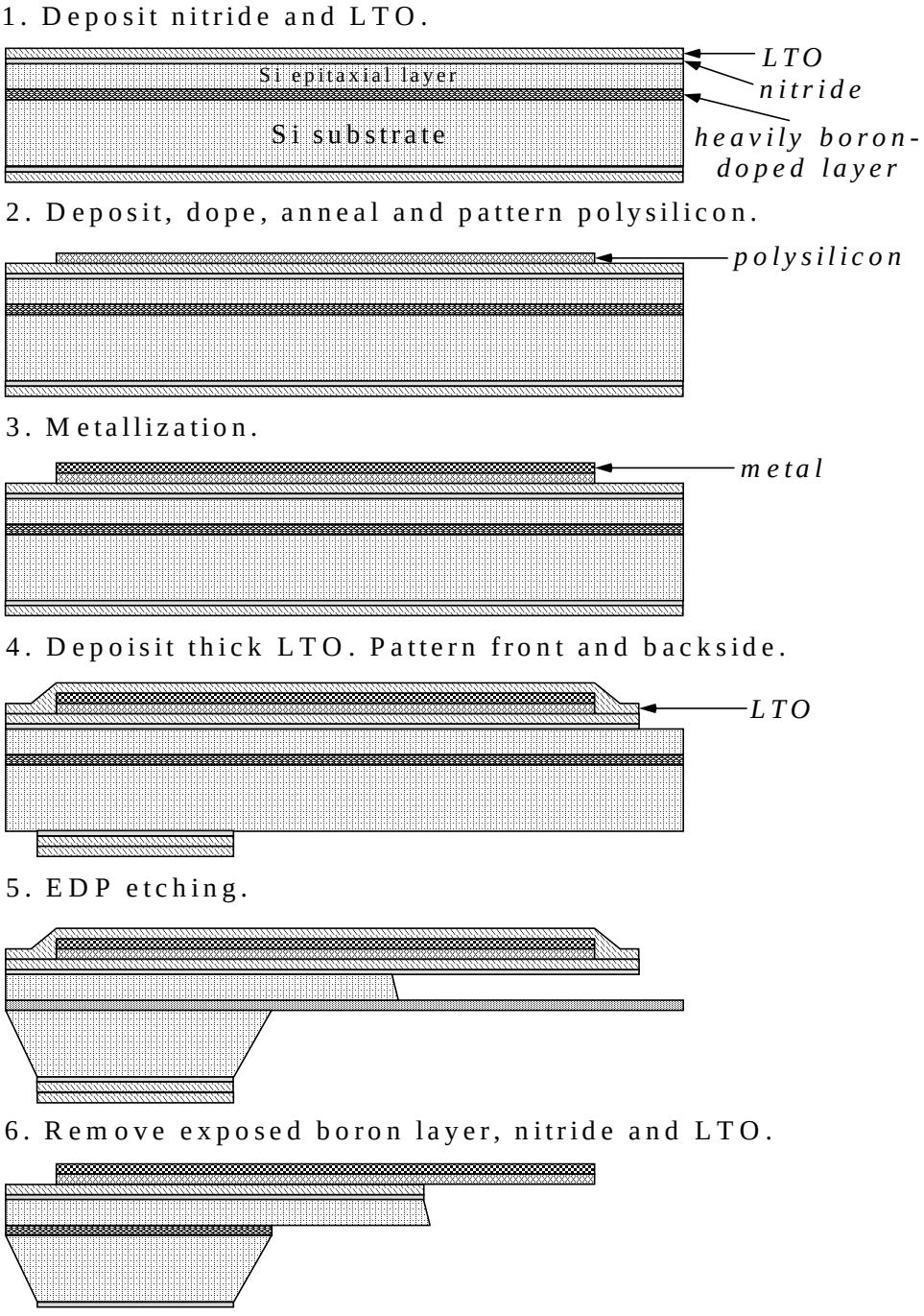

Figure 2.4 Simplified process flow with cross-sections for the fabrication of the micromachined hot-wire anemometers.

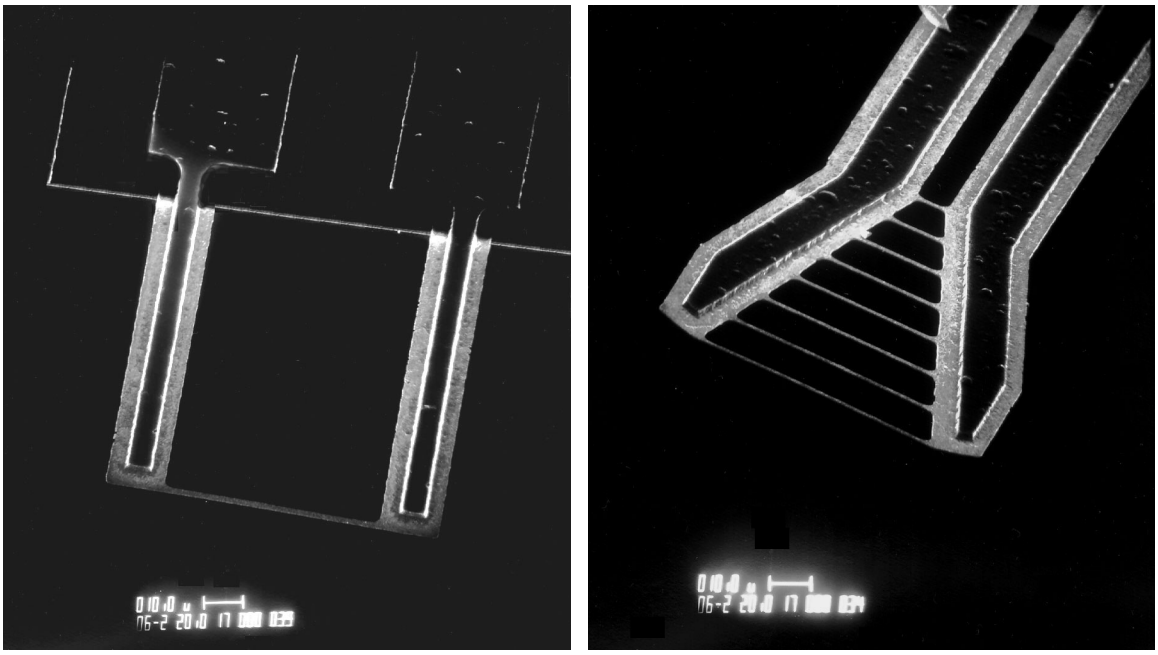

(a) (b)

Figure 2.5 SEM pictures of (a) a 70 μm long hot wire and (b) a multiple-wire probe.

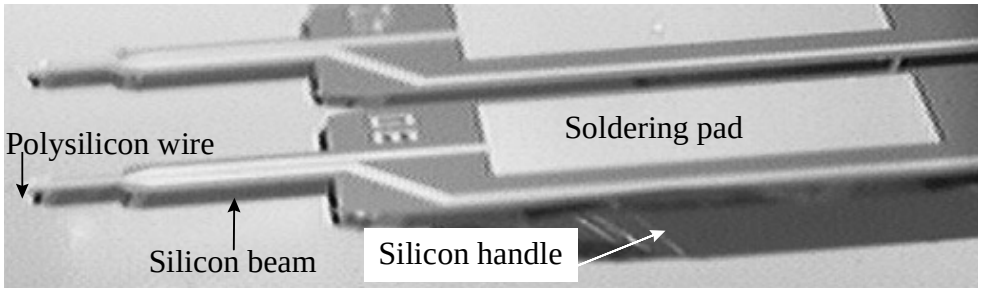

Figure 2.6 Photograph of tilted hot wires.

2.2.3 Corner Compensation

It is worthwhile to discuss more about the Si anisotropic etching used in this process. The convex corners of a single crystal silicon structure consist of crystallographic planes with different orientations. Among them, the (211) plane has the fastest etching in Si isotropic etchants such as EDP and TMAH. As a result, the convex corners is undercut at a significant rate and the final structure may be very different from what has been designed. The solution is to add compensation structures to the corners on the mask to

delay the formation of convex corners on the real structures to the last minute of the etching. Typical compensation structures include squares and long beams. Their dimensions are determined by calibration. Basically, a wide structure can stand longer etching.

In the layout design of the hot wires, we have included the corner compensation structures shown in Figure 2.7. On the backside, they are wide and long straight beams and stand more than 10 hours of etching in EDP or TMAH for the designed structures to be formed. On the front side, they are 80 μm wide and 2000 μm long folded beams and can stand slightly longer time of etching. The etching is stopped as soon as the compensation structures on the front side are consumed completely.

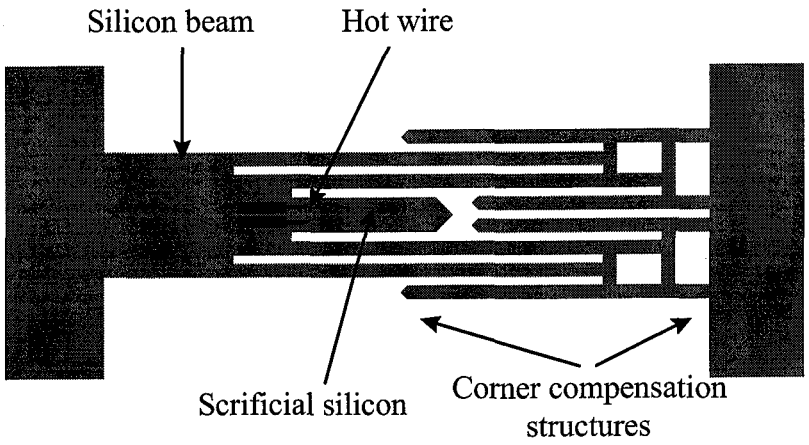

Figure 2.7 Long corner compensation structures on the front side for a 10 hour or more EDP etching.

The above corner compensation scheme works well if the Si isotropic etching is repeatable and uniform. In reality, it is not always the case. For example, the etching properties of EDP, including the etching rate and the ratio of etching rates for different crystallographic planes change as the solution gets aged. TMAH is better, but is still far from ideal. To make the fabrication process more robust, the front and back side etchings need to be separated. For example, pattern and etch the back side; deposit chrome or gold to protect back side; Pattern and etch front side. This way, the corner compensation

structures on the front side can be much shorter, thus greatly reducing the bad effect of non-uniform etching.

2.2.4 Packaging

After the fabrication process is finished, each individual probe is connected to the wafer frame or other probes by four 70 μm thick narrow Si beams and can be easily separated by hand without causing damage to the delicate probes. The package of the anemometers is a ceramic tube a few centimeters long and 3 mm in diameter. The anemometer handle is soldered with electrical cables, placed inside the tube and then epoxy-fixed. During handling, all mechanical vibrations are avoided so as not to damage the wires. Figure 2.8 shows the prototype of a packaged anemometer. This is, of course, the very preliminary packaging scheme for laboratory testing purpose only. More delicate packaging can be developed, such as using thermal compression wire bonding, etc..

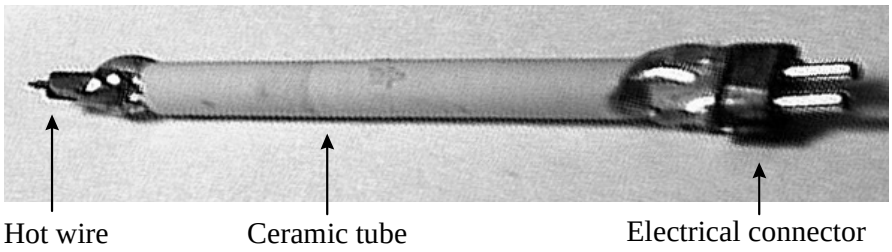

Figure 2.8 Prototype of packaged hot wires.

2.3 Steady-State Characteristics

2.3.1 Operation Modes and Operating Points

Traditionally, there are two operation modes for hot wires. One is the constant current (CC) mode and the other is the constant temperature (CT) mode. The CC bias circuit is very simple and always stable due to the lack of feedback. It does not generate much noise in the output. However, its low frequency response (only a few hundred Hz for

conventional hot wires) has limited its use to very few occasions. CT bias, on the other hand, uses the most advanced feedback electronics to achieve high frequency response. It is the dominating operation mode of practical hot wire anemometers, even though the circuit is less stable and more noisy. However, for our new micromachined hot wires, it is important that we investigate their characteristics in both CC and CT modes because this would help us understand the new hot wires more completely.

The acceptable operating temperature range of hot wires determine the operating points. The wire has to be heated up to certain temperature well above the ambient in order to have reasonable sensitivity to velocity. However, that temperature can not be too high so as to burn the wire or cause deterioration and constant drift in material properties. For polysilicon, the operating temperature should be kept below 250^{o}C, even though its melting temperature is around 1400^{o}C. Therefore, a reasonable operating temperature range of our hot wires in air should be 100 - 250^{o}C, which corresponds to resistance over-heat ratios (defined as $a_R = \frac{R - R_a}{R_a}$, where R is the wire resistance at the operating temperature, R_a is the wire resistance at the ambient temperature) of 0.15 - 0.35.

2.3.2 Sensitivity to Velocity

The steady-state characteristics of hot wires with lengths between 20-160 μm have been measured in wind-tunnels. For example, Figure 2.9 and Figure 2.10 are the responses of an 80 μm long hot-wire anemometer at different over-heat ratios without any electronic gain in CC and CT modes, respectively. As a comparison, Figure 2.11 gives the responses of a conventional hot wire 1 mm in length and 5 μm in diameter in CC mode. The two types of hot wires needs about 2-3 mW and 4-8 mW respectively to reach the over-heat ratios of 0.15-0.35. The significantly smaller power consumption of our hot wire is mainly due to its smaller size. Furthermore, our hot wire only needs less than 1.5 mA of bias current, while the conventional hot wire needs more than 10 mA. This is because our hot wire has much higher resistance as well as smaller size (less power).

Since almost all commercial operational amplifiers can supply a few mA of current, the current booster used in most conventional hot wire anemometer circuits can be omitted for our hot wire. Finally, and most importantly, our hot wire is more sensitive than the conventional one. This is simply because the output voltage is proportional to the square root of wire resistance, i.e., $V = \sqrt{PR}$, when the total power P is given.

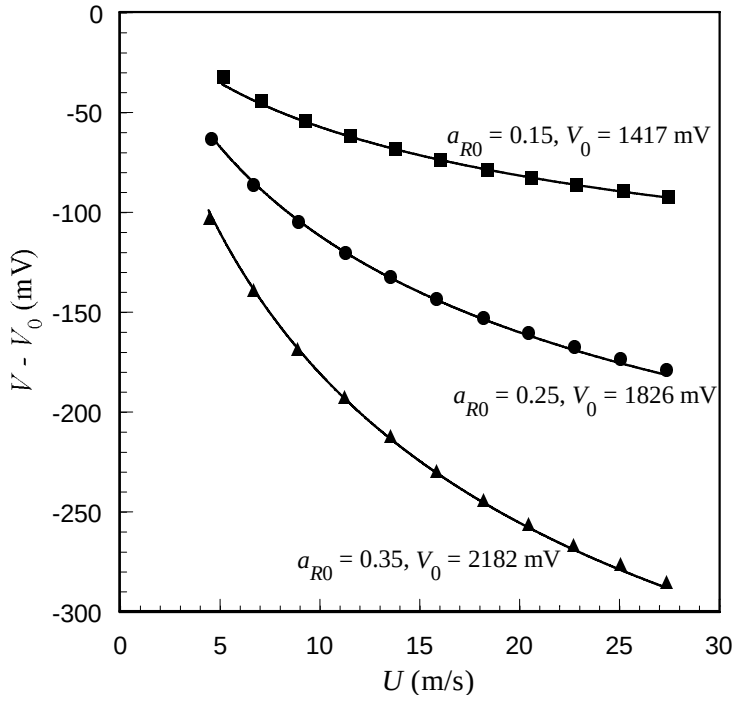

Figure 2.9 Output characteristics of a 80 μm long hot wire in CC mode.

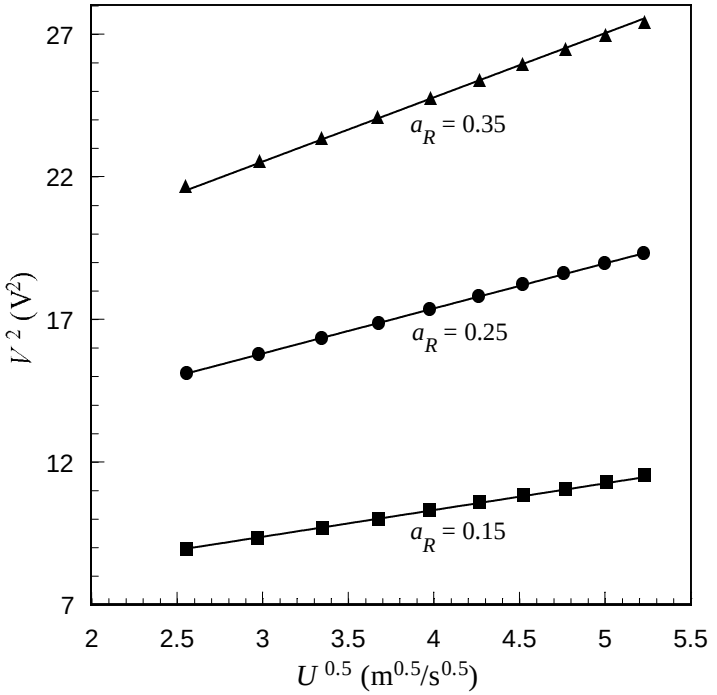

Figure 2.10 Output characteristics of the 80 μm long hot wire in CT mode.

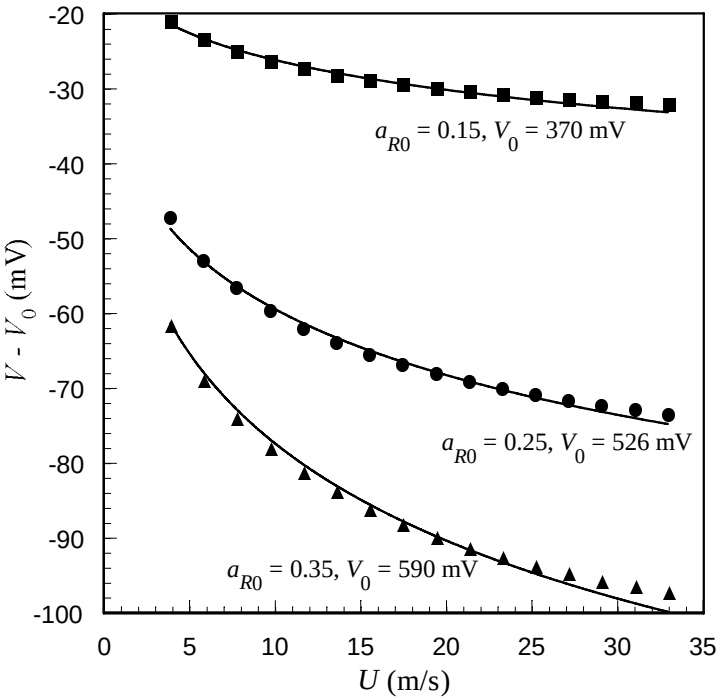

Figure 2.11 Response of a conventional hot wire (5 μm in diameter, 1mm in length) in CC mode. The currents are 10 mA, 13 mA and 14 mA respectively for over-heat ratios of 0.15, 0.25 and 0.35.

Figure 2.12 shows the absolute and normalized output voltages at a flow velocity of 27 m/s for hot wires with lengths from 20 μm to 160 μm in CT mode with a_R = 0.25. It is obvious that longer (larger aspect ratio) hot wires are more sensitive than shorter ones. This is one of the reasons why conventional hot wires always have large aspect ratio (> 200). However, for the micromachined hot wires, even the short ones have reasonable sensitivities. For example, the output of a 20 μm long hot wire in CT mode at a velocity of 27 m/s is about 200 mV. According to the trend of the data in Figure 2.12, the output for a 10 μm hot wire should be over 100 mV. Unfortunately, the experimental data is not available for hot wires of this length.

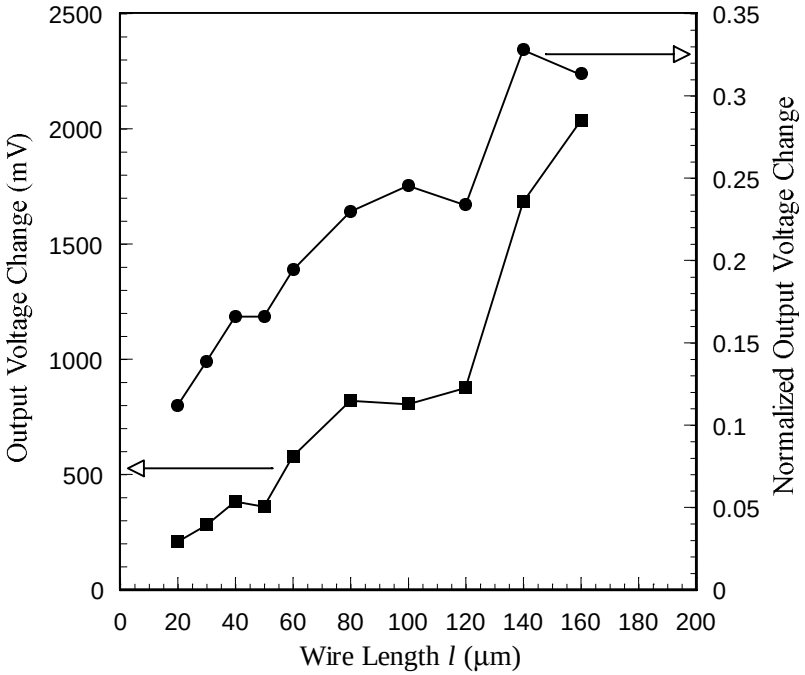

Figure 2.12 Output voltages at the air flow velocity of 27 m/s for hot wires with different lengths in CT mode.

2.3.3 King's Law

To interpret the above experimental results, we have to work out the theoretical relationship between the hot wire output and flow velocity using heat transfer theory. In

steady state, power generation and heat dissipation of a hot wire is balanced, i.e.,

$$P = \frac{V^2}{R} = K_{eff}(U)(T - T_a) \qquad (2.1)$$

where R is the wire resistance, V is the voltage across the wire, T is the average wire temperature, T_a is the ambient temperature, U is the flow velocity, and $K_{eff}(U)$ is the effective heat transfer coefficient. In a laminar flow, King's law applies,

$$K_{eff}(U) = K_0 + K_1 U^n \qquad (2.2)$$

where K_0 is the heat transfer coefficient which takes into account conduction, radiation and free convection and is not a function of U, and $K_1 U^n$ represents forced convection by the boundary layer flow. The exponent n depends on the hot wire structure and is approximately 0.5 for conventional hot-wire anemometers.

Assuming linear change of wire resistance with temperature, we have

$$R = R_0[1 + \alpha_R(T - T_0)] \qquad (2.3)$$

where R_0 and α_R are the resistance and the temperature coefficient of resistivity (TCR) at the reference temperature T_0. Therefore,

$$T - T_a = \frac{R - R_a}{\alpha_R R_0} \qquad (2.4)$$

and Eq. (2.1) becomes

$$\frac{V^2}{R} = K_{eff}(U)\frac{R - R_a}{\alpha_R R_0} \qquad (2.5)$$

In CC mode, the current is kept constant. Therefore,

$$\frac{V}{R} = \frac{V_0}{(1 + a_{R0})R_a} \qquad (2.6)$$

where V_0 and a_{R0} are the output voltage and over-heat ratio at $U = 0$, respectively. The following expression for K_0 can be derived from Eq. (2.5) at $U = 0$,

$$K_0 = \frac{\alpha_R R_0 {V_0}^2}{a_{R0}(1+a_{R0}){R_a}^2} \tag{2.7}$$

This equation means that, for a given K_0 and a_{R0}, the voltage is larger for higher resistance wires. Combining Eqs. (2.5)-(2.7), it is easy to show that

$$V = \frac{1+AU^n}{1+(1+a_{R0})AU^n}V_0 \tag{2.8}$$

or

$$V - V_0 = -\frac{a_{R0}AU^n}{1+(1+a_{R0})AU^n}V_0 \tag{2.9}$$

where $A = \frac{K_1}{K_0}$. Eq. (2.9) shows that the output voltage of a hot wire with positive TCR decreases with increasing flow velocity. The higher the over-heat ratio, the faster the decrease.

In CT mode, R is kept constant and Eq. (2.5) can be written as

$$V^2 = (1 + AU^n){V_0}^2 \tag{2.10}$$

Usually, the circuit in Figure 2.13 is used to realize the CT operation and the voltage across the Wheatstone bridge V_{out}, rather than the voltage across the hot wire V, is measured. Then,

$$V_{out} = \beta V = \beta(1+AU^n)^{\frac{1}{2}}V_0 \tag{2.11}$$

where $\beta = 1 + \frac{R_2}{R_3}$ is the bridge gain.

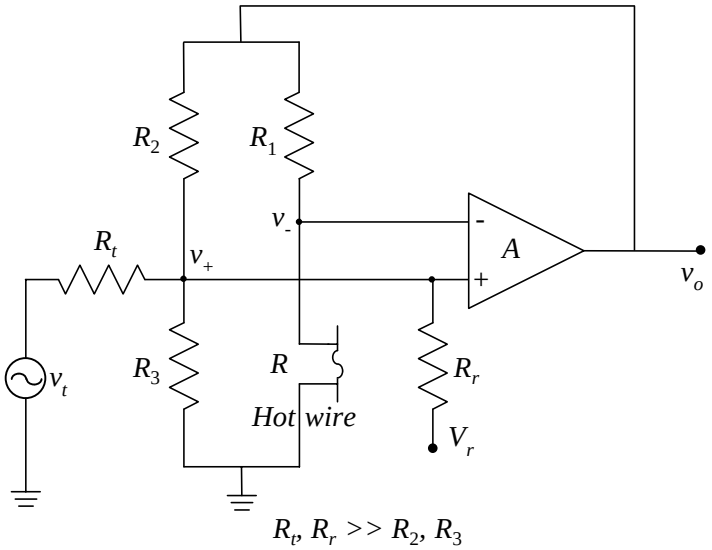

Figure 2.13 Simplified constant temperature bias circuit.

Eqs. (2.8) and (2.11) have been used to fit the experimental data in Figs. 2.9-2.11. The ratio of K_1 to K_0, i.e., the constant A in Eqs. (2.8) and (2.11) is found to be 0.10 for the micromachined hot wire and 0.15 for the conventional hot wires. This means that the conventional hot wire has higher percentage of total heat being convected to the flow than the micromachined one. It is simply because the conventional hot wire has much higher aspect ratio and hence less conduction loss to the support needles. On the other hand, the fitted value of the exponent n to velocity U for our hot wire and for the conventional hot wire in CC mode are 0.77 and 0.50 respectively. Thus, in comparison with the conventional hot wire, our hot wire has a more linear response and less degradation in sensitivity in the high velocity regime than the conventional anemometer. Previously [17], we suspected that the unusual n value for our hot wire might be caused by the non-circular cross section of our hot wire [18]. However, n and A for the micromachined hot wire in CT mode has been found to be 0.50 and 0.143, respectively. Then the question is that which fitted value truly represents the exponent n to velocity U in King's law. In order to answer this question, we need to re-examine the fitting equations and the fitting process. We considered A to be not a function of the flow velocity. This assumption stands for hot wires with larger aspect ratios, where K_0 and K_1 are independent of wire

temperature, or, for hot wires in CT mode, where the wire temperature is kept constant. However, for hot wires with small aspect ratios in CC mode, significant conduction heat loss to the supports exists, which in turn causes non-uniform temperature distribution along the wire. K_0 and K_1 may thus depend on the wire temperature, which changes with flow velocity in CC mode. This effect may have been reflected through the different fitting values of n in CC and CT modes.

2.4 Dynamic Characteristics

2.4.1 Time Constant Measurement

In addition to steady-state response, dynamic response of an anemometer is also important especially for large Reynolds number flow measurements. In fact, the greatest advantage of the micromachined hot wires should be their improved bandwidth due to their extremely small sizes or low thermal masses.

The time constant can be determined by superimposing a small signal (square wave or sine wave) on a constant bias current. Figure 2.14 shows the CC bias circuit that we used to measure our hot wires. The square wave is used if the hot wire has only one thermal time constant. This is often true for hot wires with aspect ratios larger than 200 [4]. For example, Figure 2.15 shows the square-wave response of a hot wire with aspect ratio of 200. The slow increase or decrease following the abrupt jump in the output is the thermal delay. τ is simply the time duration for the output change due to the thermal effect to reach 63% of its total, as shown in Figure 2.15.

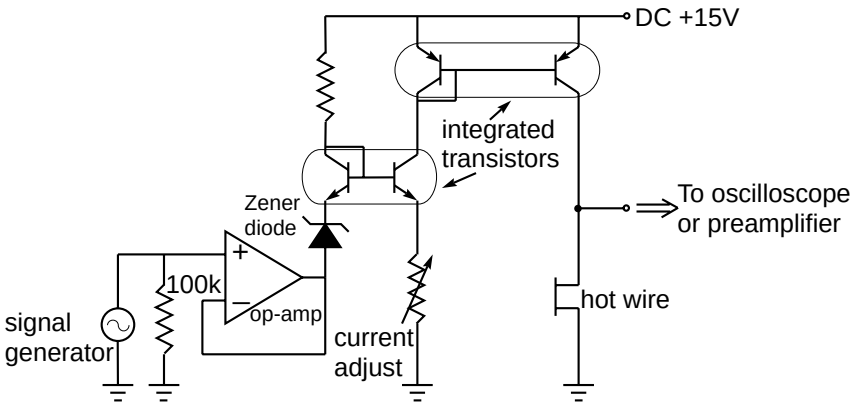

Figure 2.14 The constant current anemometer circuit for time constant measurement and wind-tunnel testing.

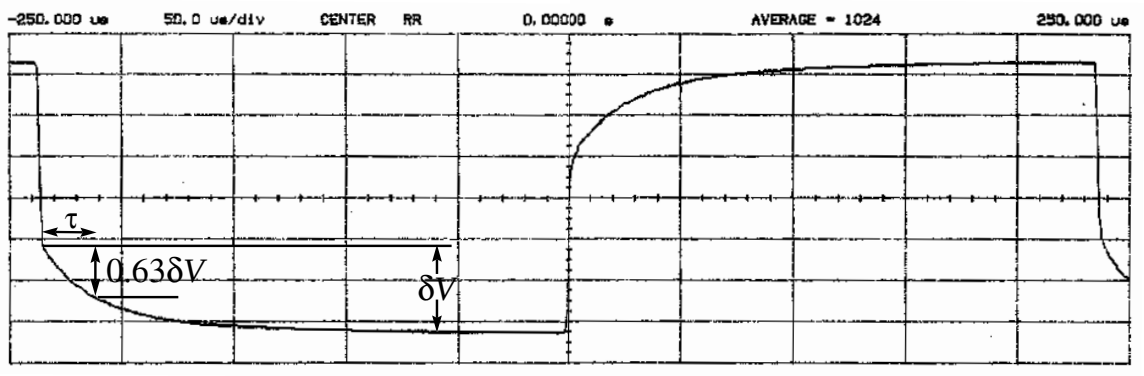

Figure 2.15 Square wave response of a 200 μm long hot wire in CC mode.

On the other hand, if the aspect ratio of a wire is less than 200, its thermal response may have two time constants. One (τ_2) is associated with the sensing wire and the other (τ_1) with the wire support shanks. In this case, the square-wave method may not be accurate, and using sine wave signals to do the measurements in the frequency domain is suggested. Figure 2.16 shows the measured total resistance of a 10 μm long wire as a function of frequency. Since the two time constants are different by more than an order of magnitude, this resistance can be accurately modeled by,

$$r = R + \frac{r_1}{1 + s\tau_1} + \frac{r_2}{1 + s\tau_2} \tag{2.12}$$

where R is the dc resistance, r_1 and r_2 are the amplitudes of the resistance change caused by ac heating effects. Fitting Eq. (2.12) into the experimental data in Figure 2.16 then gives the two thermal time constants. For our hot wires, the ratio of r_2 to r_1 increases with the wire length l. The time constant associated with the support shanks, τ_1, always ranges between 100 μs and 300 μs because of the fixed geometry design.

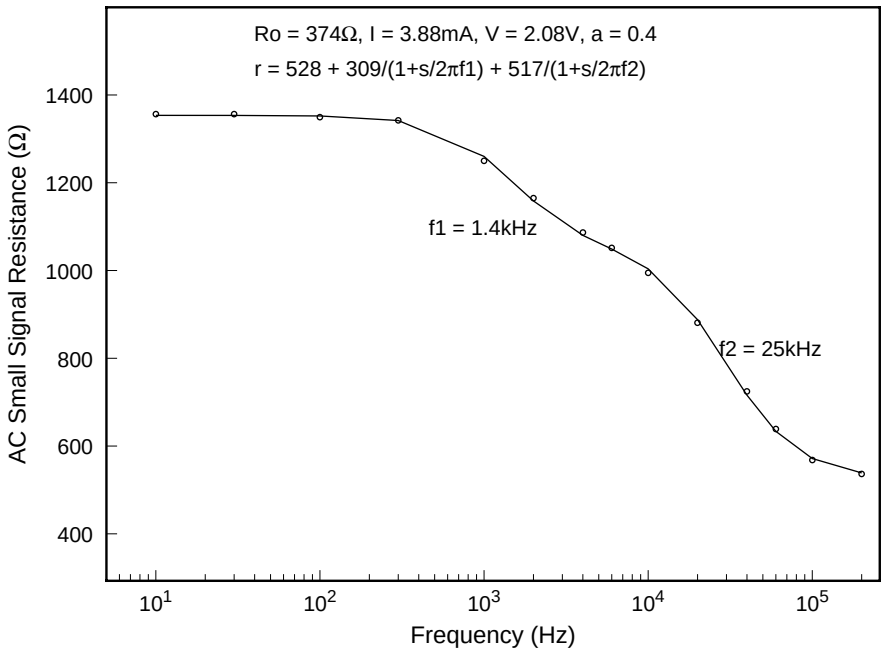

Figure 2.16 AC resistance change of a 10 μm long hot wire in the frequency domain.

2.4.2 Transient Analysis

In principle, the heat transfer is a three-dimensional problem. However, because the dimension of the wire in x direction is much larger than those in y and z directions, we can reasonably assume that temperature is not a function of y and z and the problem is simplified to a one-dimensional heat transfer.

For a wire with length l, width w and thickness d at some time t and position x from one end (see Figure 2.21), the sum of the heat absorbed by a unit length wire and the heat flowing into it through thermal conduction and convection in unit time must be equal to the ohmic heat [19], i.e.,

$$\rho w d c_p \frac{\partial T}{\partial t} - \kappa_{poly} w d \frac{\partial^2 T}{\partial x^2} + 2h(w+d)(T - T_a) = J^2 \rho_0 w d[1 + \alpha_R (T - T_0)] \quad (2.13)$$

where ρ = 2.32 g/cm^3, c_p = 0.7 J/(g·^{o}C), ρ_0 and κ_{poly} are the density, specific heat, resistivity, and thermal conductivity of polysilicon, respectively, J is the current density, and h is the convective heat transfer coefficient of the wire. The above differential equation can be solved with the boundary conditions $T(0,t) = T(l,t) = T_a$ and initial condition $T(x,0) = T_a$, assuming that the two support shanks are perfect heat sinks. The solution is a multiple-mode response. The first mode determines the time constant,

$$\tau_2 = \tau_{21}\tau_{22} / (\tau_{21} + \tau_{22}) \quad (2.14)$$

with

$$\tau_{21} = \frac{\rho c_p}{-\alpha_R J^2 \rho_0 + \frac{2h(w+d)}{wd}} \quad (2.15)$$

and

$$\tau_{22} = \left(\frac{l}{\pi}\right)^2 \frac{\rho c_p}{\kappa_{poly}} \quad (2.16)$$

It can be seen from the above expressions that the time constant is due to two components: convection time constant τ_{21}, which dominates for long wires, and conduction time constant τ_{22}, which dominates for short wires.

The measured τ_2 for our wires with lengths from 20 μm to 160 μm is shown in Figure 2.17 with the theoretical fitting from Eq. (2.14). h = 0.65 W/(cm^2·^{o}C) and κ_{poly} = 0.26W/(cm^2·^{o}C) (0.34W/(cm^2·^{o}C) reported by Tai et al. [20]) are the fitting parameters. It is clear that when l is small, the conduction time constant τ_{22} dominates and that τ_2 increases parabolically with l. If l is large, the convection time constant τ_{21} dominates and τ_2 becomes a constant. As expected, the shortest wire (10 μm long) gives the smallest τ_2 of 4 μs. This corresponds to a bandwidth of 40 kHz, which is a significant improvement over conventional hot wires (typical bandwidth of 700 Hz).

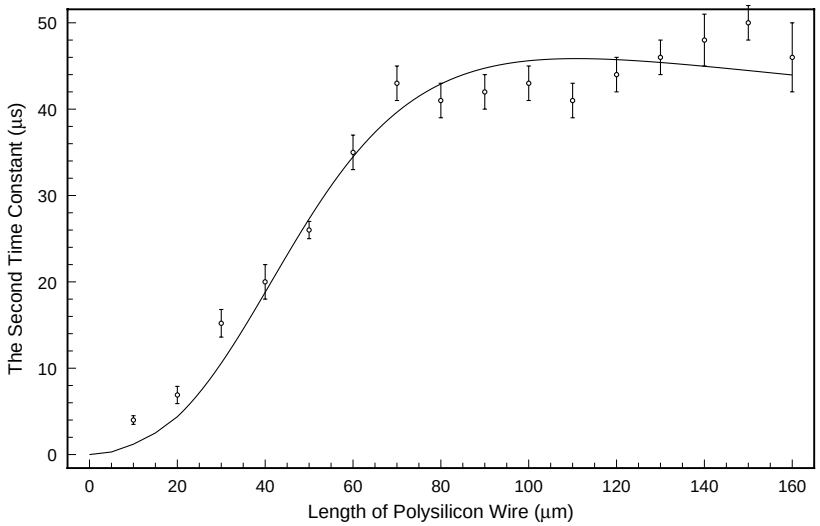

Figure 2.17 Time constant in CC mode of the micromachined hot wires with different wire lengths.

2.4.3 Constant Temperature Operation

Since the constant temperature operation of hot wires involves negative feedback, it significantly improves the frequency response over the CC mode. Figure 2.13 shows the circuit for our CT frequency response measurement. It is basically a Wheatstone bridge with a feedback operational amplifier. The ratio between R_2 and R_3 determines the dc gain, while R_1 is used to adjust the over-heat ratio or operating temperature of the hot wire. R_r and V_r are introduced here to adjust the stability of the circuit, i.e. the quality factor Q in this second-order system. The characteristic equations for the hot wire, the operational amplifier and the bridge are as follows,

$$\tau \frac{d\Delta R(t)}{dt} + \Delta R(t) = ai(t) + bu(t) \tag{2.17}$$

$$M \frac{dv_o(t)}{dt} + v_o(t) = A_0 v_i(t) \tag{2.18}$$

$$v_i(t) = -\frac{R_2 R_3 V_r}{(R_2 + R_3) R_r \overline{V_o}} v_o(t) - \frac{R_1 \overline{V_o}}{(R_1 + \overline{R})^2} \Delta R(t) - \frac{R_1 \overline{R}}{(R_1 + \overline{R}) R_t} v_t(t) \tag{2.19}$$

$$i(t) = \frac{v_o(t)}{R_1 + \overline{R}} - \frac{\overline{V_o}}{(R_1 + \overline{R})^2} \Delta R(t) + \frac{R_1}{(R_1 + \overline{R}) R_t} v_t(t) \tag{2.20}$$

where $\Delta R(t) = R(t) - \overline{R}$, $a = 2a_R \overline{R}(R_1 + \overline{R}) / \overline{V_o}$, $i(t)$ is the current through the hot wire, $u(t)$ is the flow velocity fluctuation, M and A_0 are the time constant and dc open loop gain of the operational amplifier. The output voltage $v_o(s)$ in frequency domain can be derived from these characteristic equations,

$$v_o(s) = \frac{G_v(1 + \frac{s}{\omega_1}) v_t(s) + S_u u(s)}{1 + \frac{s}{Q\omega_2} + (\frac{s}{\omega_2})^2} \tag{2.21}$$

where

$$\omega_1 = \frac{1}{(1 + 2a_R)\tau} \tag{2.22}$$

is the frequency at the system zero,

$$\omega_2 = \sqrt{\frac{2a_R A_0}{M\tau} \frac{R_2 R_3}{(R_2 + R_3)^2}} \tag{2.23}$$

is the natural frequency of the system,

$$Q = \frac{(R_2 + R_3) R_r}{R_2 R_3} \frac{\overline{V_o}}{V_r} \frac{M\omega_2}{A_0} \tag{2.24}$$

is the quality factor and can be adjusted by varying V_d,

$$G_v = (1 + \frac{1}{2a_R}) \frac{R_1 + \overline{R}}{R_t} \tag{2.25}$$

is the dc gain to the electrical testing signal v_t, and

$$S_u = \frac{b\overline{V_o}}{2a_R\overline{R}} \tag{2.26}$$

is the sensitivity to flow velocity signal. The system is normally biased into the critical damping state by adjusting Q to 0.5 to maximize the usable bandwidth.

According to Eq. (2.21), if the response to the electrical signal v_t is measured, the response to the velocity signal u can be predicted. Therefore, the electrical signal v_t is often used to calibrate the dynamic response of CT anemometers as sine or square wave velocity signals are difficult to obtain experimentally. However, when doing velocity measurements, the electrical signal must be disconnected. It is worth noting that the gain-bandwidth product of the operational amplifier can limit the bandwidth of the overall circuit. To maximize the bandwidth, a high speed operational amplifier should be used.

In the case that a hot wire has two time constants, the CT anemometer will behave as a third-order system. This will make frequency response measurement and analysis much more difficult. Fortunately, our anemometers always have r_2/τ_2 much larger than r_1/τ_1 (at least by an order of magnitude) so that Eqs. (2.21-2.23) can still be used with τ replaced by τ_2.

As an example, LM6365, a very high speed operational amplifier with gain-bandwidth of 700 MHz is used with a 10 μm long hot wire to constitute an CT anemometer system. The resistance ratio of R_2 to R_3 is set to one. The over-heat ratio is adjusted to 0.3. Figure 2.18 shows the measured frequency response to v_t together with its theoretical fitting curve and the calculated response to velocity signal from Eq. (2.21). System bandwidth of 1.4 MHz is identified. This is further verified by the square-wave response shown in Figure 2.19 where the bandwidth is approximately $1/(1.3t_1)$=1.4 MHz, with t_1 = 0.5 ~ 0.6 μs as the peak width of the response curve [4]. Furthermore, Eq. (2.23) can be used to calculate the bandwidth. The result is 1.6 MHz, which is in good agreement with the measured value.

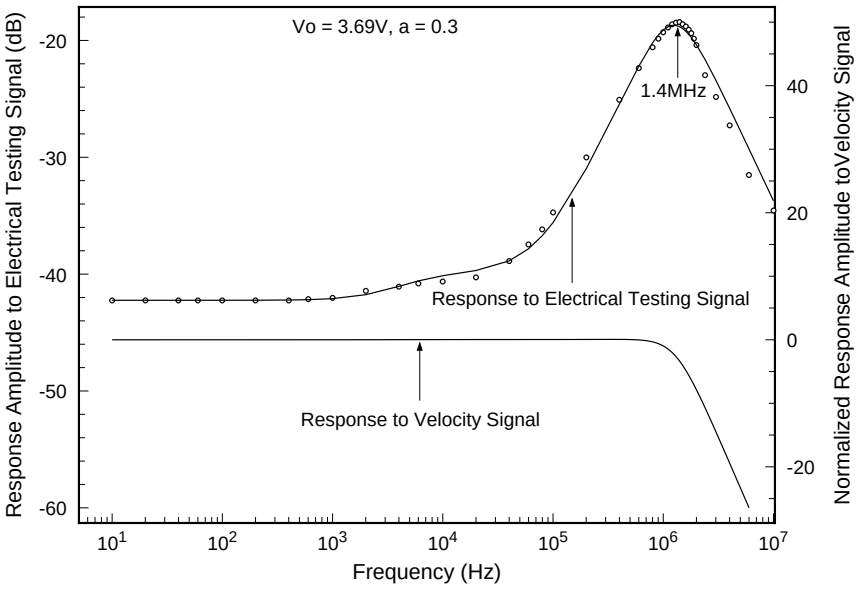

Figure 2.18 Frequency response of a 10 μm long hot wire in CT mode.

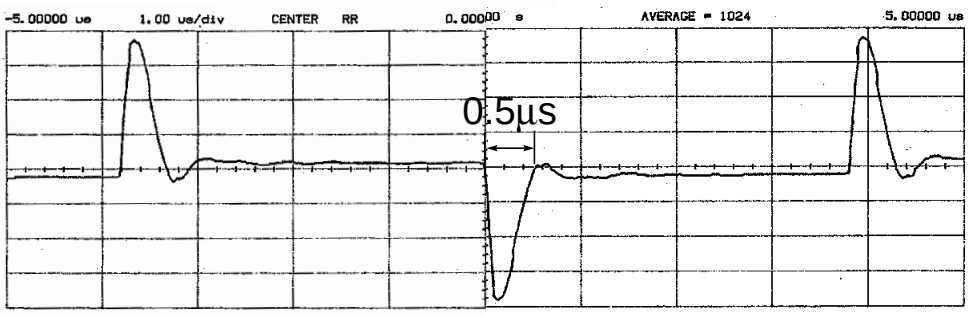

Figure 2.19 Square wave response of the 10 μm long hot wire in CT mode.

Finally, Figure 2.20 shows the bandwidth of hot wires with different lengths. The bandwidths for the hot wires with large aspect ratios are around 500 kHz. During the measurement, we noticed that the circuit stability is very sensitive to the stray capacitance of long cables connecting the hot wires to the circuit, due to the high resistance of the wires. A small capacitor may be added in parallel with R_1 to suppress the oscillation. However, in some cases, the bandwidth is degraded.

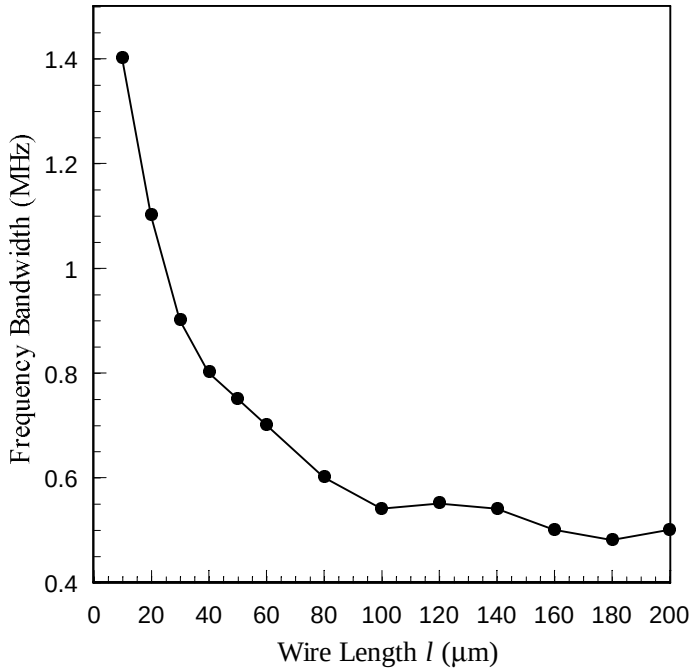

Figure 2.20 Frequency bandwidths of the micromachined hot wires with different lengths in CT mode.

2.5 Directional Dependency

Directional dependency is essential if an anemometer is used to determine velocity vectors. For hot-wire anemometers, the output characteristics depend on yaw angle and pitch angle, but not on roll angle. As defined in Figure 2.21, the yaw angle θ is the angle between the velocity vector U and its transverse component normal to the wire , and the pitch angle ϕ is between U and the hot wire probe body axis y.

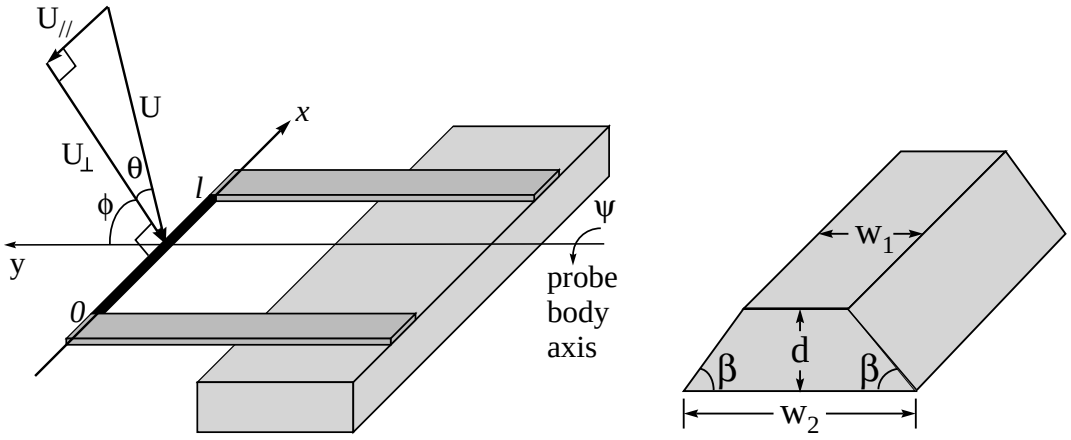

Figure 2.21 (a) Definition of yaw angle θ, pitch angles ϕ and roll angle ψ. (b) Cross section of micromachined hot wires.

For large aspect-ratio hot wires, the transverse velocity component $U_t = U\cos\theta$ is mainly responsible for wire cooling by convection. A cosine response to the yaw angle θ is then expected. This dependency is observed for an 160 μm long hot wire in CT mode, as shown in Figure 2.22. The sharp voltage drop for the yaw angle higher than 90^o is because the wire is already in the wake of the probe body. On the other hand, for small aspect-ratio hot wires such as a hot point sensor, there should be no directional dependency. Therefore we do not expect strong yaw angular dependency of the output for a small aspect-ratio hot wire. This is also confirmed in Figure 2.23 for a 20 μm long hot wire. Interestingly, at low velocity, the output voltage increases with θ. This is because the longitudinal velocity component parallel to the wire, U_l, contributes more to the wire cooling through the convection assisted heat conduction along the wire than U_t.

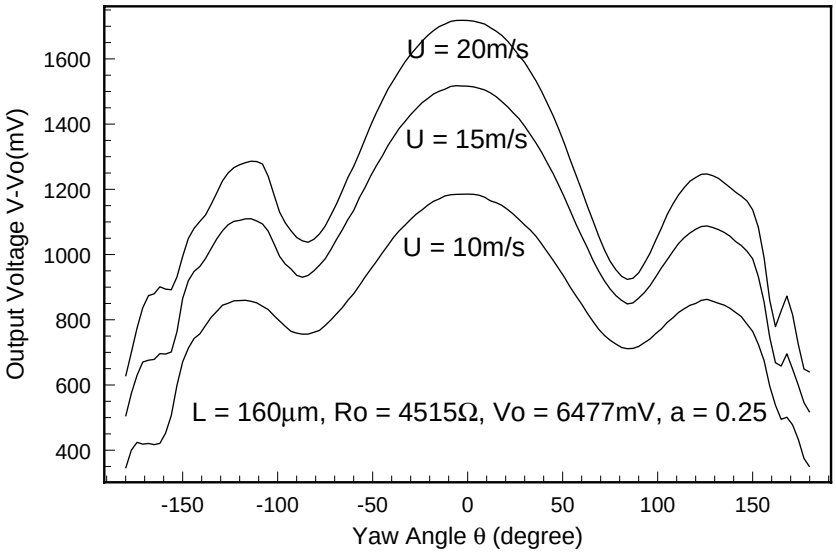

Figure 2.22 Yaw angular dependency of a 160 μm long hot wire in CT mode.

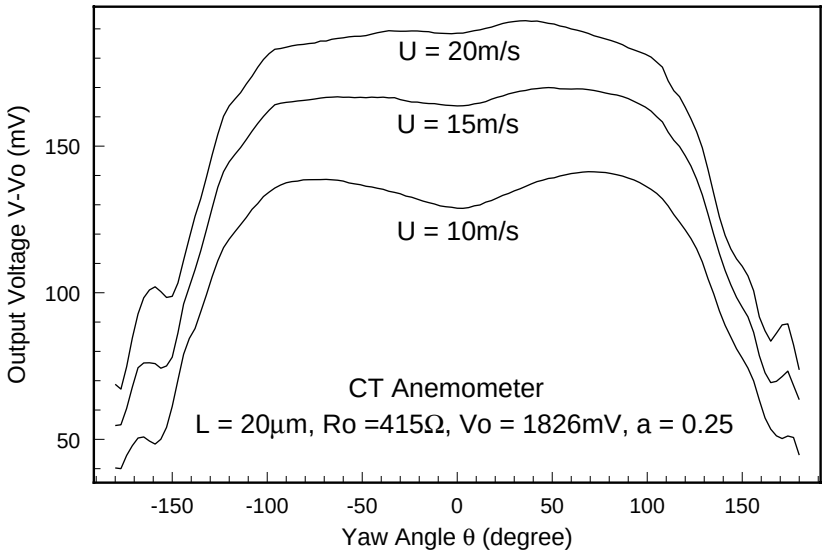

Figure 2.23 Yaw angular dependency of a 20 μm long hot wire in CT mode.

The pitch angular dependency of a hot wire can be attributed to three effects [21]. The first one is the hydrodynamic effect of the fluid passing through the opening bounded by the wire, support shanks, and the probe body when the pitch angle is increased. The second one is the additional cooling of the support shanks because they are oriented

broadside to the flow during pitching. This effect is especially significant for shorter wires since more heat loss is through the support shanks. The third one is the varying effective cooling surface area during pitching. The first two effects tend to increase the cooling, while the third one depends on the wire geometry. For conventional hot wires, which are cylinders with large aspect ratios, only the first effect exists and causes 10 to 20 percent change in output during pitching. However, for micromachined hot wires all three effects are significant due to the special structural design and the trapezoidal wire cross section (Figure 2.21(a)). Therefore we expect strong pitch angular dependency for these hot wires, especially when *l* is small.

Figure 2.24 and Figure 2.25 are the measured pitch angular dependencies of the same hot wires used in Figure 2.22 and Figure 2.23. The 20 μm long hot wire has much stronger pitch angle dependence than the 160 μm long one. This strong pitch angular dependency is useful for such a short wire because the yaw angular dependence is small. We noticed that the pitch characteristics are not symmetrical. One of the maxima occurs at $\phi = -90^o$ (when air flow blows toward the bottom of the wire), while the other one occurs at $\phi = 60^o \sim 70^o$. We believe this is due to the trapezoidal wire cross section.

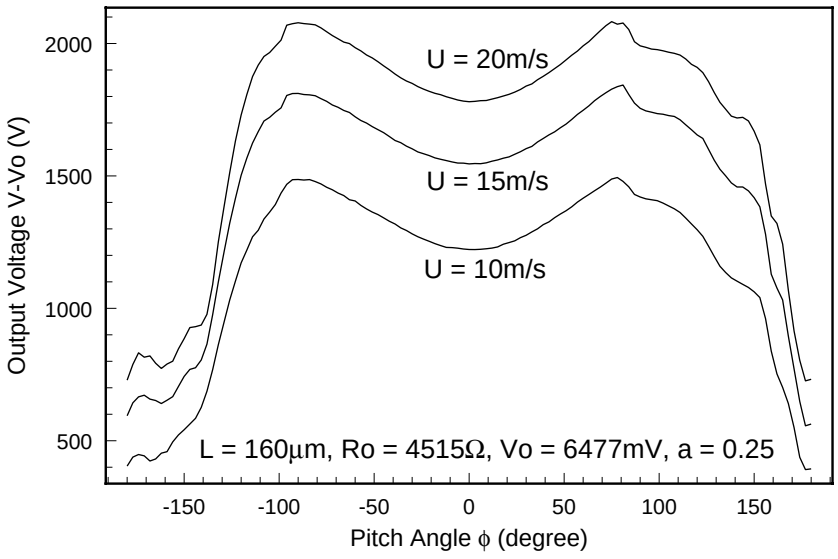

Figure 2.24 Pitch angular dependency of the 160 μm long hot wire (also used in Figure 2.22) in CT mode.

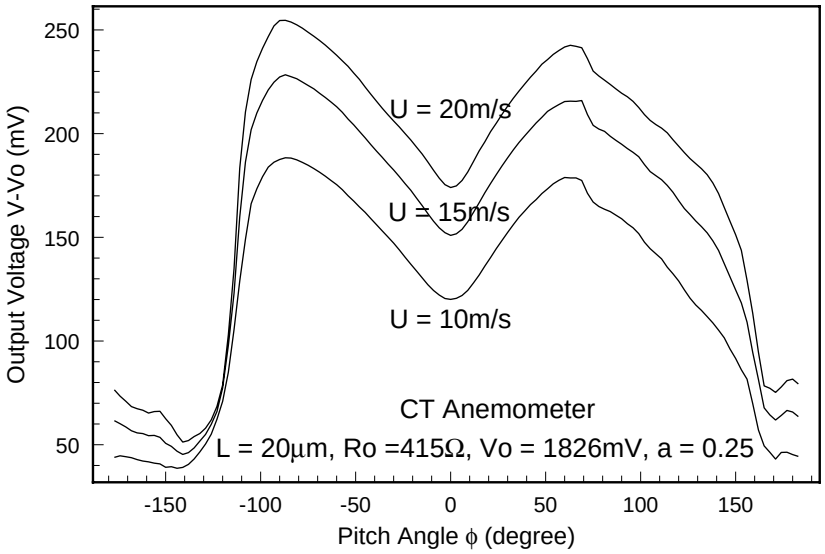

Figure 2.25 Pitch angular dependency of a 20 µm long hot wire (also used in Figure 2.23) in CT mode.

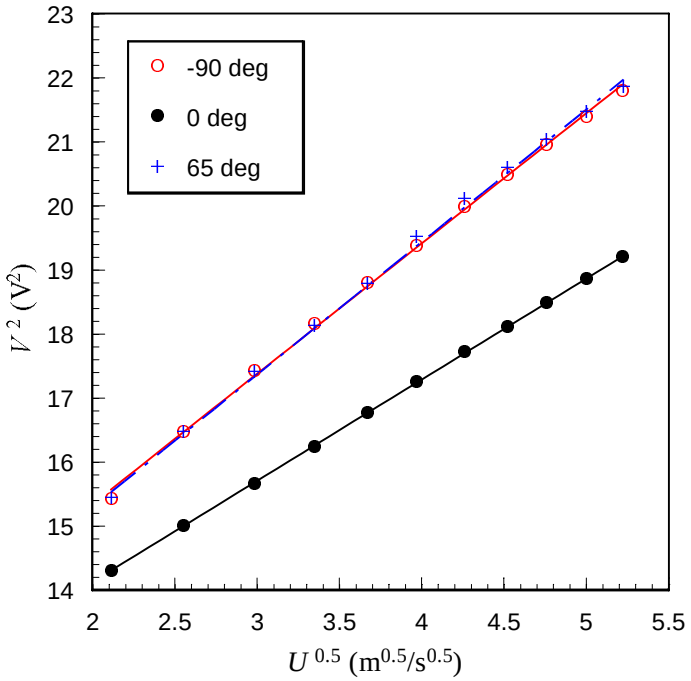

Figure 2.26 Steady-state characteristics of an 80 µm long hot wire (also used in Figs. 2.9 and 2.10) in CT mode at different pitch angles.

Finally, Figure 2.26 shows the output characteristics of the same 80 µm long hot wire

used in steady-state characterization but at three different pitch angles in CT mode. It is obvious that the V^2 vs. $U^{0.5}$ curve deviate from the linear fits at ϕ = -90^o and 65^o. As a matter of fact, the exponent *n* found from the best fitting is about 0.44 at ϕ = -90^o and 65^o. We speculate that this is also because of the trapezoidal wire cross section [18].

2.6 Discussion

2.6.1 Comparison with Conventional Hot Wires

Table 2.1 Comparison between conventional and micromachined hot wires.

Parameters	Conventional Hot Wire	Micromachined Hot Wire
fabrication	hand assembly	micromachining (mass producible)
material	Pt, W, Pt-Ir	polysilicon
TCR (%/^{o}C)	0.08 - 0.45	0.15
resistivity (Ω·cm)	5.5-31x10^{-6}	10^{-3}
density (g/cm^3)	20	2.3
thermal conductivity (W/cm·^{o}C)	0.18-2.0	0.34
specific heat (J/g·^{o}C)	0.13	0.7
length	1 mm	10-160 μm
diameter (μm)	5	1 μm (width) 0.5 μm (thickness)
power (mW)	4-8	2-4
current (mA)	10-15	1-2
sensitivity (CC) at 27 m/s (mV)	80	50-400
sensitivity (CT) at 27 m/s (mV)	300	100-2000
time constant (CC) (μs)	500	5-50
bandwidth (CT) (MHz)	0.15	0.5-1.4
directional sensitivity (yaw)	good	good (long wires) bad (short wires)
directional sensitivity (pitch)	small	large

Table 2.1 gives the overall comparison between a typical conventional hot wire and our micromachined hot wires. The performances are based on the measurement results at over-heat ratio of 0.25.

2.6.2 Small Aspect-Ratio Wires

Conventional hot wires with short length or small aspect ratios are normally not used in flow velocity measurement because they are difficult to make, their resistance and sensitivities are too low, and serious conduction losses to the supports cause dynamic effects that are difficult to measure experimentally [4]. However, for micromachined hot wires, the first two problems no longer exist. The sensitivity is low for short wires compared to the long wires in its own kind, but is more than enough to be detected. The last problem is still questionable, even though the calculated frequency response to velocity signal is shown to be flat all the way to its cutoff frequency. More analysis and tests need to be done. If this problem is not serious, the short micromachined hot wires would be useful in some special areas where fast response and high spatial resolution are desired.

2.6.3 Center-Lightly Doped Hot Wires

It is well known that lightly doped polysilicon has very high resistivity and large negative TCR (up to -1%/^{o}C). Therefore, a uniformly and lightly doped polysilicon hot wire could have an unprecedented high sensitivity. However, its resistance would be so high that it would require an extremely high voltage to operate. To avoid this problem, we have designed a center-lightly doped polysilicon hot wire which is geometrically the same as Figure 2.2, but the 2 μm center part of the wire is lightly doped. The overall dc resistance of the wire at the operating point is less than 10 kΩ. It has been confirmed that this type of hot wire indeed has a higher sensitivity than the uniformly and heavily doped hot wires. In addition, they have a smaller time constant [22]. However, these hot wires have serious stability problems due to the resistance drift caused by the dopant diffusion

from the heavily doped sides to the lightly doped middle.

2.6.4 Mechanical Rigidity

The support shanks of our hot wires are only 0.5 μm thick but are about 20 μm wide. They can not stand in high speed flows that are not in parallel with them. However, the geometry and structure is by no means the optimum for the support shanks of micromachined hot wires, and a lot of improvements can be made. For example, we can simply increase the thickness of the polysilicon to a few microns for the support shanks while keeping the thickness of the polysilicon wire at one half micron.

2.6.5 Bending of Support Shanks

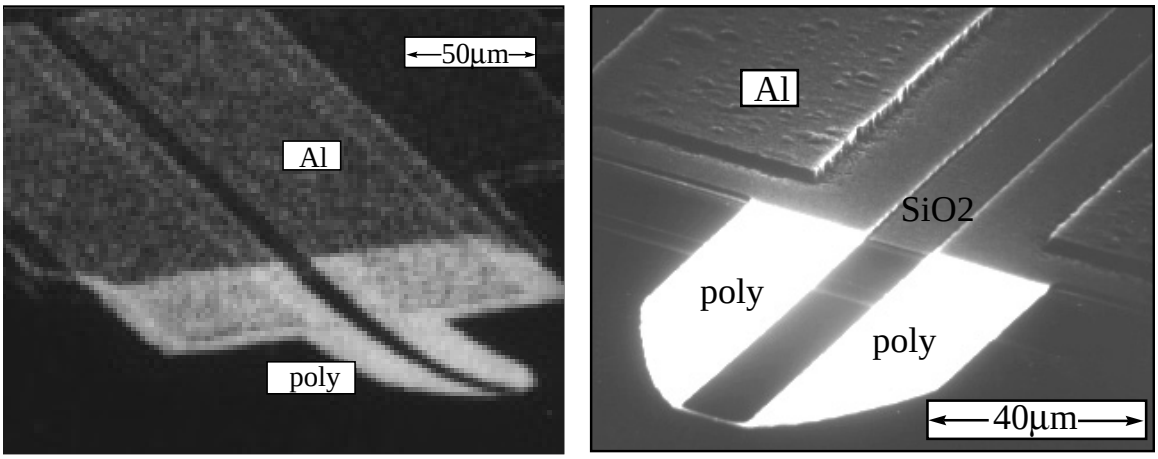

(a) (b)

Figure 2.27 SEM pictures of hot wires made from (a) polysilicon deposited at 620^{o}C; (b) crystallized amorphous silicon deposited at 560^{o}C.

As previously mentioned in the design section, we found that the stress distribution along the depth of the polysilicon deposited at 620^{o}C and annealed at 1100^{o}C is not uniform. Sometimes, the tips of all the anemometer probes in a wafer made from this type of polysilicon bend up about 50 μm, as shown in Figure 2.27(a). However, this

phenomenon is never observed in anemometers made from the polysilicon deposited at 560^{o}C and annealed at 1100^{o}C, as shown in Figure 2.27(b). The reason might be that the structure of as-deposited and as-implanted amorphous silicon films are uniform along the depth. During annealing, the grain growth is uniform, so the stress distribution is uniform too.

2.6.6 Temporal Drift

It has been observed that the resistance of hot wires increases slowly during the operation. Figure 2.28 shows the temporal drift of a 80 μm long heavily doped probe. Several factors contribute to the drift. First, the polysilicon is not protected and could be oxidized during high temperature operation. This can be avoided by a conformal anti-oxidation layer coating over the free standing polysilicon structures. This would only increase the time constant a little. Second, since dopants in polysilicon have high diffusion coefficients, the temperature non-uniformity and the electric field across the wire at the operating temperature of a few hundred degrees may cause the slow diffusion of dopants. Amemiya et al. [23] found that the resistivity of heavily doped polysilicon decreases under high current density. This contradicts our observation. Further studies need to be done on the mechanism of this drift.

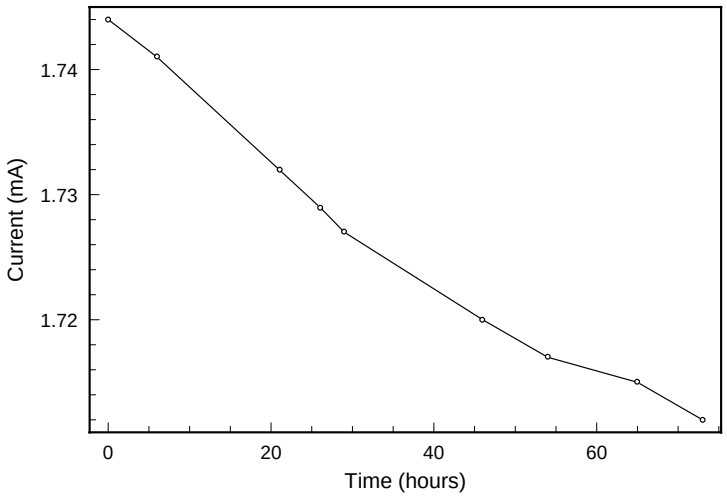

Figure 2.28 The temporal drift of a 80 μm long hot wire at V = 2.5 V and a_R = 0.35.

2.7 Summary

A new type of micromachined hot-wire anemometer has been developed. Extensive characterization of their steady-state characteristics, frequency responses and directional dependencies has been carried out. These hot wires, if properly designed, can be practical. They can significantly out-perform conventional hot wires in some aspects such as spatial resolution, sensitivity and frequency response.

Bibliography

[1] L. V. King, "On the Convection of Heat from Small Cylinders in a Stream of Fluid: Determination of the Convection Constants of Small Platinum Wires, with Application to Hot-Wire Anemometry," *Proc. R. Soc. London*, Vol. 90, pp. 563-570, 1914.

[2] R. F. Blackwelder, "Hot-Wire and Hot-Film Anemometers," *Methods of Experimental Physics: Fluid Dynamics*, Vol.18, Part A, Academic Press, pp. 259-314, 1981.

[3] A. E. Perry, *Hot-Wire Anemometry*, Clarendon Press, 1982.

[4] L. M. Fingerson and P. Freymuth, "Thermal Anemometers," *Fluid Mechanics Measurements*, J. Goodstein, ed., Hemisphere Publishing Corp., pp. 99-154, 1983.

[5] H. H. Bruun, *Hot-Wire Anemometry: Principles and Signal Analysis*, Oxford University Press, 1995.

[6] W. R. Runyan and K. E. Bean, Semiconductor Integrated Circuit Processing Technology, Addison-Wesley, 1990.

[7] K. E. Petersen, "Silicon as a Mechanical Material," *Proc. IEEE*, Vol. 70, pp. 420-457, 1982.

[8] G. Kaminsky, "Micromachining of Silicon Mechanical Structures," *J. Vac. Sci. Technol. B*, Vol. 3, pp. 1015-1024, 1985.

[9] L. Lofdahl, G. Stemme, and B. Johansson, "Silicon Based Flow Sensors Used for Mean Velocity and Turbulent Measurements," *Experiments in Fluids*, Vol. 12, pp. 270-276, 1992.

[10] H. Rahnamai and J. N. Zemel, "Pyroelectric Anemometers: Preparation and Velocity Measurements," *Sensors and Actuators*, Vol. 2, pp. 3-16, 1981.

[11] Y. C. Tai and R. S. Muller, "Lightly Doped Polysilicon Bridge as a Flow Meter," *Sensors and Actuators*, Vol. 15, pp. 63-75, 1988.

[12] B. W. van Oudheusden and J. H. Huijsing, "Integrated Silicon Flow Direction Sensor," *Sensors and Actuators*, Vol.16, pp. 109-119, 1989.

[13] H. Seidel, "The Mechanism of Anisotropic Silicon Etching and its Relevance for Micromachining," *Digest IEEE Int. Conf. On Solid-State Sensors and Actuators* (*Tansducers'87*), pp. 120-125, 1987.

[14] R. T. Howe, "Surface Micromachining for Microsensors and Microactuators," *J. Vac. Sci. Technol. B*, Vol. 6, pp. 1809-1813, 1988.

[15] L. S. Fan, Y. C. Tai, and R. S. Muller, "Integrated Movable Micromechanical Structures for Sensors and Actuators," *IEEE Trans. Electron Devices*, Vol. 35, pp. 724-730, 1988.

[16] G. Harbeke, L. Krausbauer, E. F. Steigmeier, A. E. Widmer, H. F. Kappert, and G. Neugebauer, "Growth and Physical Properties of LPCVD Polycrystalline Silicon Films," *J. Electrochem. Soc*., Vol.131(3), pp. 675-682, 1984.

[17] F. Jiang, Y. C. Tai, C. M. Ho, K. Rainer, and M. Garstenauer, "Theoretical and Experimental Studies of Micromachined Hot-Wire Anemometer," *Digest IEEE Int. Electron Devices Meeting (IEDM)*, San Francisco, pp. 139-142, 1994.

[18] M. Jakob, *Heat Transfer*, Vol. 1, John & Wiley, New York, pp. 559-564, 1949.

[19] C. H. Mastrangelo, *Thermal Applications of Microbridges*, Ph. D. Thesis, University of California, Berkeley, 1990.

[20] Y. C. Tai, C. H. Mastrangelo, and R. S. Muller, "Thermal Conductivity of LPCVD Polycrystalline Silicon," *J. Appl. Physics*, Vol. 63, pp. 1442-1447, 1988.

[21] C. G. Lomas, *Fundamentals of Hot Wire Anemometry*, Cambridge University, 1986.

[22] F. Jiang, Y. C. Tai, C. M. Ho, and W. J. Li, "A Micromachined Polysilicon Hot-Wire Anemometer," *Digest Solid-State Sensors & Actuator Workshop*, Hilton Head, SC, pp. 264-267, 1994.

[23] Y. Amemiya, T. Ono, and K. Kato, "Electrical Trimming of Heavily Doped Polycrystalline Silicon Resistors," *IEEE Trans. Electron Devices*, Vol. ED-26, No. 11, pp. 1738-1742, 1979.

Chapter 3

Micromachined Shear Stress Sensors

3.1 Introduction

A fluid flowing past a solid boundary exerts normal and tangential stresses on it. Normal stresses or pressures are readily measured by connecting a small hole on the surface to a pressure sensor or manometer through a tube. The measurement of the tangential or shear stresses at a surface is much more difficult. However, since the information about the variation of the wall shear stress on a surface is often quite useful in analyzing a flow field, especially turbulent flow, numerous methods of measuring the local wall shear stress [1,2] have been developed so far, including the Stanton tube [3], the Preston tube [4], direct measurement using floating elements [5,6], thermal method using heated elements [7,8,9], the sub-layer fence and the electrochemical technique [10]. Among them, the most often used is the thermal method that relates the local wall shear stress and the rate of heat transfer from small thermal elements mounted flush with the surface because it has many advantages over other techniques. For example, it has negligible interference with the flow; the size of the sensor can be as small as a millimeter; the possibility of measuring fluctuations in the wall shear stress as well as the time average makes them particularly attractive for time-varying flows such as turbulent flows [11].

The typical flush-mounted hot film sensors used to measure wall shear stress are thin metal film resistors, mostly platinum and nickel, deposited on flat substrates. Since only the heat lost to the fluid by convection responds to the change of shear stress, it is desirable to thermally isolate the thin film resistor from the substrate. This minimizes the conductive heat loss and improves the sensitivity and frequency response. In the past, the

approach was to use low thermal conductivity materials as the substrates. These include glass, quartz [11,12], and plastic and polyimide films [13,14], with the polyimide film being the best. Reasonably good sensitivity can be obtained when such sensors are used in a fluid with high thermal conductivity such as water. However, they are not as satisfactory for the measurement in low thermal conductivity fluids such as air. The major problems are the low sensitivity, low frequency response and more importantly, their not-yet-well-understood performance at high frequency unsteady turbulence [15,16]. This is all because of the significant and complicated heat conduction loss to the substrates. Theoretically, improvement of sensor performance can be achieved by further reducing the thickness of the substrates. In reality, this alone will not be feasible because extremely thin substrates are difficult to produce using traditional fabrication technology and is not desirable by sensor users. Also, limited by the fabrication technology, the size of traditional hot-film sensors is typically in the millimeter range [5]. This may be tolerable in measuring the mean value of shear stress, but is certainly not acceptable in shear stress imaging with reasonable spatial resolution (i.e. tenths of mm).

There has been some effort to develop micro hot-film sensors using the more advanced Si microfabrication technology [17,18]. The performances of these devices, however, are not as good as the traditional hot-film sensors. In this chapter, we will present a new type of hot-film shear stress sensor with much improved structures and better performance made possible by silicon surface micromachining technology.

3.2 Design And Fabrication

Our new hot-film shear stress sensor has the cross-sectional structure shown in Figure 3.1. It is quite different from a traditional hot-film sensor. As a matter of fact, the structure is much more delicate and complicated. However, it is readily fabricated by using today's surface micromachining technology.

The sensing element, i.e. the thin film polysilicon resistor, is embedded in a silicon nitride diaphragm which sits on a vacuum cavity so that the conduction loss from the

diaphragm to the silicon substrate is minimal even though the cavity is shallow. Since the silicon nitride diaphragm can be very thin and its thermal conductivity is comparable to that of quartz, the thermal isolation of our sensor is much better than any of the traditional hot-film sensors.

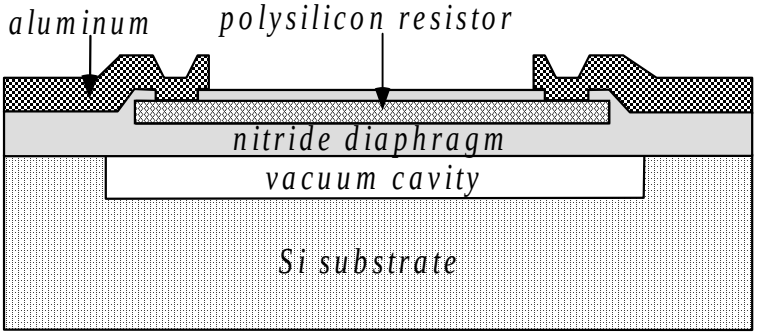

Figure 3.1 Cross-section of the micromachined shear stress sensor.

The design parameters of our sensors include the depth of the vacuum cavity and the dimensions of the diaphragm and polysilicon resistor. The requirement for the aspect ratio of the polysilicon resistor is similar to that of a hot wire sensor, i.e., the resistor has to be long enough to minimize the conduction loss through the ends. On the other hand, it is desirable to have a short polysilicon resistor as it determines the horizontal dimension of the whole sensor. We have decided that a length of 150 μm is a good trade-off. The effect of the width on the sensor performance is not clear at this moment. Therefore, we have designed several sensors with different widths, from 3 μm to 15 μm. The nitride diaphragm has to be slightly larger than the length of the polysilicon resistor to fully accommodate it so we choose 200×200 μm^2. The thickness of the diaphragm is determined to be about 1 μm such that it does not break during fabrication or operation. It can be calculated that the center of a nitride diaphragm with the above dimension will bend approximately 0.8 μm under one atmospheric pressure. Therefore, the depth of the edge of the vacuum cavity should be more than 1 μm to keep the diaphragm from touching the bottom of the cavity.

The fabrication process of the shear stress sensors starts with the deposition of 0.5 μm LPCVD low stress silicon nitride on 4" Si wafers. In the cavity areas, the nitride is removed by plasma etching with a little over-etch to give 0.9 μm trench. Then the wafers are put in oxidation furnace to grow 1.8 μm thick oxide (LOCOS process) in the trench at 1050^{o}C. A short time etch in BHF is performed to planarize the wafers and to remove the oxidized nitride. 0.4 μm of phosphosilicate glass (PSG) is deposited, patterned and annealed to form the sacrificial layer etching channel. Next, 1.2 μm of LPCVD low stress nitride is deposited as the diaphragm material. Etching holes are opened to expose the end of the PSG etching channel, and this is followed by a 49% HF etching to completely remove the PSG and thermal oxide underneath the diaphragm. The cavity is then sealed by LPCVD LTO and nitride deposition at a vacuum of 200 mTorr. The sealing materials on the diaphragm are removed by plasma and BHF etching to minimize the diaphragm thickness. A 0.5 μm polysilicon layer is deposited, doped, annealed and patterned to form the resistors on the diaphragms. Another 0.2 μm of low stress nitride is deposited to passivate the polysilicon resistors. Contact holes are opened through the passivation layer and 1 μm aluminum is evaporated, patterned and sintered to finish the whole process. The fabrication process flow with cross-sections after each step is shown in Figure 3.2 and the SEM picture of a fabricated shear stress sensor is shown in Figure 3.3. The depth of the vacuum cavity on the edges is about 2 μm, which is the sum of the thickness of PSG and thermal oxide remained after planarization. The horizontal dimension of such a sensor is less than 300×300 μm^2, more than four time smaller than the traditional hot-film sensors. The surface roughness is less than 3 μm.

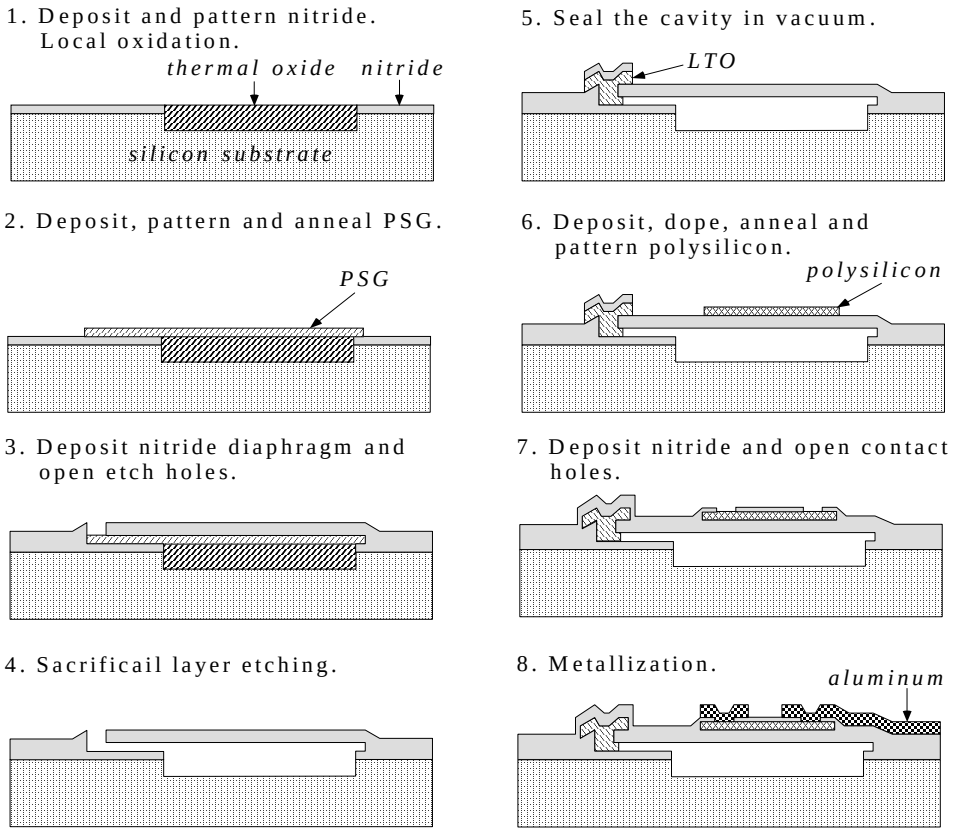

Figure 3.2 Fabrication process flow of the micromachined shear stress sensor.

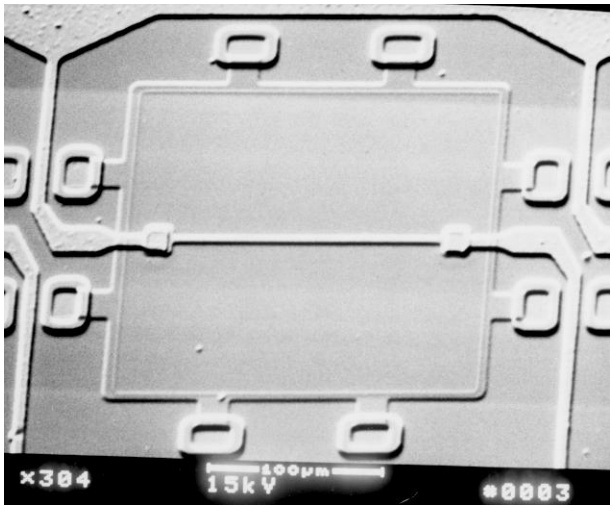

Figure 3.3 SEM picture of a micromachined shear stress sensor. The polysilicon resistor is 150 μm long and 3 μm wide. The nitride diaphragm is 200×200 μm^2. The sensor size is less than 300×300×550 (thickness) μm^3. Note that the entire sensor was in vacuum of the SEM sample chamber so the diaphragm in the picture is flat.

3.3 Heat Transfer Analysis

For the sensor structure shown in Figure 3.4, the heat transfer analysis is rather complicated because strictly speaking, it is a three-dimensional problem. However, it can be simplified to a one-dimensional problem by neglecting the heat conduction in *x* and *z* direction on the diaphragm area (region I) and in *y* and *z* direction on the sensing wire (region II).

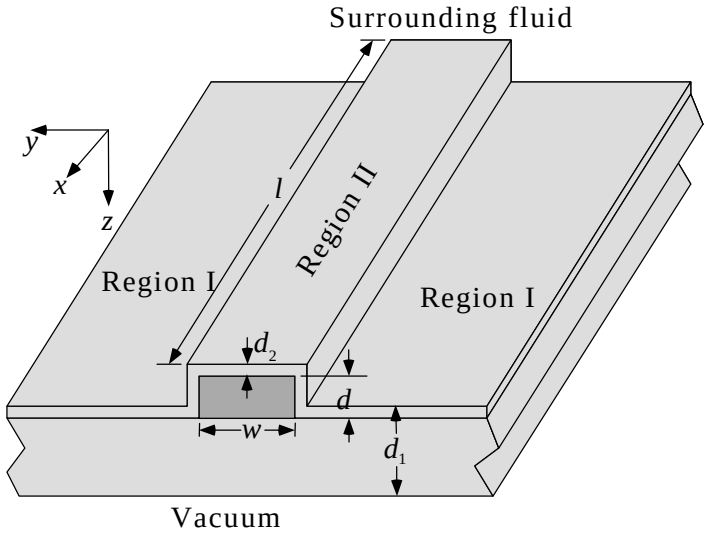

Figure 3.4 Geometry of the diaphragm and the sensing wire.

In an infinitesimal element *dy* in region I ($|y| \geq \frac{w}{2}$), the heat balance equation is

$$(\rho dc_p)_1 ldy \frac{\partial T_1}{\partial t} = \kappa_1 \frac{\partial^2 T_1}{\partial y^2} dyd_1 l - hldy(T_1 - T_a) \tag{3.1}$$

where T_1 is the temperature of the element, T_a is the ambient temperature, *w* and *l* are the width and length of the sensing wire, d_1, κ_1, ρ_1 and c_{p1} are the thickness, thermal conductivity, density and specific heat of the diaphragm, and *h* is the convective heat-transfer coefficient per unit area from the element to the fluid above the diaphragm. Rearranging the above equation yields

$$\frac{1}{\alpha_1}\frac{\partial T_1}{\partial t} = \frac{\partial^2 T_1}{\partial y^2} - \frac{h}{\kappa_1 d_1}(T_1 - T_a) \tag{3.2}$$

where $\alpha_1 = \dfrac{\kappa_1 d_1}{(\rho d c_p)_1}$ is the diffusivity of the diaphragm material. Introducing small perturbations on ambient temperature and heat transfer coefficient, i.e., $T_a = \bar{T}_a + \tilde{T}_a$ and $h = \bar{h} + \tilde{h}$, then

$$T_1 = T_{1s}(y) + T_{1t}(y, t) \tag{3.3}$$

where $T_{1s}(y)$ is the steady-state temperature which satisfies

$$\frac{\partial^2 T_{1s}}{\partial y^2} - \delta^2 (T_{1s} - \bar{T}_a) = 0 \tag{3.4}$$

and $T_{1t}(y, t)$ is the transient temperature change which satisfies

$$\frac{1}{\alpha_1}\frac{\partial T_{1t}}{\partial t} = \frac{\partial^2 T_{1t}}{\partial y^2} - \delta_0{}^2 (T_{1t} - \tilde{T}_a) - \frac{T_{1s} - \bar{T}_a}{\kappa_1 d_1}\tilde{h} \tag{3.5}$$

with $\delta_0 = \sqrt{\dfrac{\bar{h}}{\kappa_1 d_1}}$.

It is easy to show that the solution for Eq. (3.4) with the boundary condition $T_{1s}(\frac{L}{2}) = \bar{T}_a$ is

$$T_{1s} - \bar{T}_a = C_1[e^{-\delta_0 y} - e^{-\delta_0 (L-y)}] \qquad (y \geq \frac{w}{2}) \tag{3.6}$$

where C_1 is the constant of integration. Insert Eq. (3.6) into Eq. (3.5) and perform the Laplace transform,

$$\frac{\partial^2 T_{1t}(y, s)}{\partial y^2} - \left(\delta_0{}^2 + \frac{s}{\alpha_1}\right) T_{1t}(y, s) + \delta_0{}^2 \tilde{T}_a - \frac{C_1\left[e^{-\delta_0 y} - e^{\delta_0 (y-L)}\right]}{\kappa_1 d_1}\tilde{h} = 0 \tag{3.7}$$

The solution for this equation at $y \geq \frac{w}{2}$ with the boundary condition $T_{1t}(\frac{L}{2}) = \frac{\tilde{\tilde{T}}_a}{1+sM_s}$ is

$$T_{1t}(y,s) = \left\{\frac{\delta_0{}^2}{\delta^2}\left[1 - e^{\delta(y-\frac{L}{2})}\right] + \frac{1}{1+sM_s}e^{\delta(y-\frac{L}{2})}\right\}\tilde{T}_a - \frac{\alpha_1}{s\kappa_1 d_1}\tilde{h}C_1\left[e^{-\delta_0 y} - e^{\delta_0(y-L)}\right] + C_2(s)\left[e^{-\delta y} - e^{\delta(y-L)}\right] \quad (3.8)$$

where M_s is the thermal time constant of the substrate and $\delta = \sqrt{\delta_0{}^2 + \frac{s}{\alpha_1}}$.

In region II, the heat balance equation for an infinitesimal dx is

$$(\rho dc_p)_e w dx \frac{\partial T}{\partial t} = \frac{I^2\rho_0}{wd}dx[1+\alpha_R(T-T_0)] + 2(\kappa d)_e dx \left.\frac{\partial T}{\partial y}\right|_{y=\frac{w}{2}} + (\kappa d)_e w dx \frac{\partial^2 T}{\partial x^2} - h(w+2d+2d_2)dx(T-T_a) \quad (3.9)$$

where T_0 is the reference temperature, ρ_0 and α_R are the resistivity and its temperature coefficient of the sensing wire at T_0, $(\rho dc_p)_e = (\rho dc_p)_1 + \rho dc_p$ and $(\kappa d)_e = (\kappa d)_1 + \kappa d$. Rearrange the above equation to get

$$\frac{1}{\alpha_e}\frac{\partial T}{\partial t} = \frac{I^2\rho_0}{(\kappa d)_e w^2 d}[1+\alpha_R(T-T_0)] + \frac{2}{w}\left.\frac{\partial T}{\partial y}\right|_{y=\frac{w}{2}} + \frac{\partial^2 T}{\partial x^2} - \frac{h(w+2d+2d_2)}{(\kappa d)_e w}(T-T_a) \quad (3.10)$$

where $\alpha_e = \frac{(\kappa d)_e}{(\rho dc_p)_e}$ is the effective diffusivity of region II.

In steady state, the above equation becomes

$$\frac{\partial^2 T_s}{\partial x^2} + \frac{\bar{I}^2\rho_0}{(\kappa d)_e w^2 d}[1+\alpha_R(T_s-T_0)] + \frac{2}{w}\left.\frac{\partial T_s}{\partial y}\right|_{y=\frac{w}{2}} - \frac{h(w+2d+2d_2)}{(\kappa d)_e w}(T_s - \bar{T}_a) = 0 \quad (3.11)$$

At $y = \frac{w}{2}$, we have the following boundary conditions

$$T_s = T_{1s}(\frac{w}{2}) \tag{3.12}$$

and

$$(\kappa d)_e \left.\frac{\partial T_s}{\partial y}\right|_{y=\frac{w}{2}} = \kappa_1 d_1 \left.\frac{\partial T_{1s}}{\partial y}\right|_{y=\frac{w}{2}} = -\kappa_1 d_1 \delta_0 C_1 \left[e^{-\delta_0 \frac{w}{2}} + e^{\delta_0 (\frac{w}{2} - L)} \right] \tag{3.13}$$

From Eqs. (3.6) and (3.12), we have

$$C_1 = \frac{T_s - \overline{T}_a}{e^{-\delta_0 \frac{w}{2}} - e^{\delta_0 (\frac{w}{2} - L)}} \tag{3.14}$$

Plug it into Eq. (3.13)

$$\left.\frac{\partial T_s}{\partial y}\right|_{y=\frac{w}{2}} = -\frac{\kappa_1 d_1}{(\kappa d)_e} \frac{\delta_0 (T_s - \overline{T}_a)}{\tanh(\delta_0 L')} \tag{3.15}$$

with $L' = \frac{L - w}{2}$. By substituting the above expression into Eq. (3.11), we can rewrite it as

$$\frac{\partial^2 T_s}{\partial x^2} - \lambda_0{}^2 (T_s - \overline{T}_a - \varepsilon) = 0 \tag{3.16}$$

with

$$\lambda_0{}^2 = \frac{1}{(\kappa d)_e w} \left[\overline{h}(w + 2d + 2d_2) + \frac{2\sqrt{\overline{h}\kappa_1 d_1}}{\tanh(\delta_0 L')} - \frac{\alpha_R \overline{I}^2 R_0}{l} \right] \tag{3.17}$$

$$\varepsilon = \frac{\overline{I}^2 \overline{R}_a}{\lambda_0{}^2 (\kappa d)_e w l} \tag{3.18}$$

and

$$\bar{R}_a = \rho_0 \frac{l}{wd}[1 + \alpha_R(\bar{T}_a - T_0)] = R_0[1 + \alpha_R(\bar{T}_a - T_0)] \tag{3.19}$$

This second-order differential equation can be solved by considering the symmetry of the temperature distribution $T_s(x)$ with respect to $x = 0$ and the boundary condition $T_s(\pm\frac{l}{2}) = \bar{T}_a$. The solution is

$$T_s - \bar{T}_a = \varepsilon - \varepsilon \frac{\cosh(\lambda_0 x)}{\cosh(\lambda_0 l/2)} \tag{3.20}$$

The average temperature increase of the sensing element above the ambient is

$$\bar{T}_s - \bar{T}_a = \varepsilon\left[1 - \frac{2}{\lambda_0 l}\tanh\left(\frac{\lambda_0 l}{2}\right)\right] = \frac{\bar{I}^2 \bar{R}_a}{{\lambda_0}^2 (\kappa d)_e wl}\left[1 - \frac{2}{\lambda_0 l}\tanh\left(\frac{\lambda_0 l}{2}\right)\right] \tag{3.21}$$

Once again, introduce small perturbations on electrical current, ambient temperature and heat transfer coefficient in region II, i.e., $I = \bar{I} + \tilde{i}$, $T_a = \bar{T}_a + \tilde{T}_a$ and $h = \bar{h} + \tilde{h}$, which results in $T = T_s + T_t(t)$. Eq. (3.10) then becomes

$$\begin{aligned} \frac{1}{\alpha_e}\frac{\partial T_t}{\partial t} &= \frac{\bar{I}^2 R_0 \alpha_R T_t + 2\bar{I}\tilde{i} R_0[1 + \alpha_R(T_s - T_0)]}{(\kappa d)_e wl} + \frac{2}{w}\left.\frac{\partial T_t}{\partial y}\right|_{y=\frac{w}{2}} \\ &+ \frac{\partial^2 T_t}{\partial x^2} - \frac{w + 2d + 2d_2}{(\kappa d)_e w}\bar{h}(T_t - \tilde{T}_a) - \frac{w + 2d + 2d_2}{(\kappa d)_e w}(T_s - \bar{T}_a)\tilde{h} \end{aligned} \tag{3.22}$$

The first boundary condition for T_t is

$$T_t = T_{1t}(\frac{w}{2}) \tag{3.23}$$

$$T_t = \left[\frac{{\delta_0}^2}{\delta^2}(1 - e^{-\delta L'}) + \frac{e^{-\delta L'}}{1 + sM_s}\right]\tilde{T}_a - \frac{\alpha_1}{s\kappa_1 d_1}\tilde{h}(T_s - \bar{T}_a) + C_2(s)\left[e^{-\delta\frac{w}{2}} - e^{\delta(\frac{w}{2} - L)}\right] \tag{3.24}$$

$$C_2(s) = \frac{-\left[\frac{\delta_0{}^2}{\delta^2}(1-e^{-\delta L'}) + \frac{e^{-\delta L'}}{1+sM_s}\right]\tilde{T}_a + T_t + \frac{\alpha_1}{s\kappa_1 d_1}\tilde{h}(T_s - \bar{T}_a)}{e^{-\delta\frac{w}{2}} - e^{\delta(\frac{w}{2}-L)}} \tag{3.25}$$

The second boundary condition is

$$\left.\frac{\partial T_t}{\partial y}\right|_{y=\frac{w}{2}} = \frac{\kappa_1 d_1}{(\kappa d)_e}\left.\frac{\partial T_{1t}}{\partial y}\right|_{y=\frac{w}{2}} = \frac{\kappa_1 d_1}{(\kappa d)_e}\left[\frac{1}{1+sM_s}\frac{\delta}{\sinh(\delta L')} + \frac{\delta_0{}^2}{\delta}\tanh\left(\frac{\delta L'}{2}\right)\right]\tilde{T}_a$$
$$-\left[\frac{\delta}{\tanh(\delta L')} - \frac{\delta_0}{\tanh(\delta_0 L')}\right]\frac{\alpha_1\tilde{h}}{s(\kappa d)_e}(T_s - \bar{T}_a) - \frac{\kappa_1 d_1}{(\kappa d)_e}\frac{\delta T_t}{\tanh(\delta L')} \tag{3.26}$$

Insert the above expression into Eq. (3.22) and perform the Lapalace transform

$$\frac{\partial^2 T_t}{\partial x^2} - \lambda^2 T_t + \frac{\upsilon + \sigma}{(\kappa d)_e w} - \frac{\sigma}{(\kappa d)_e w}\frac{\cosh(\lambda_0 x)}{\cosh(\lambda_0 l/2)} = 0 \tag{3.27}$$

with

$$\lambda^2 = \frac{1}{(\kappa d)_e w}\left[\bar{h}(w + 2d + 2d_2) + \frac{2\kappa_1 d_1\delta}{\tanh(\delta L')} - \frac{\alpha_R \bar{I}^2 R_0}{l}\right] + \frac{s}{\alpha_e}$$
$$\approx \lambda_0{}^2\left[1 + b\left(\sqrt{1+\frac{if}{f_1}} - 1\right) + \frac{if}{f_2}\right] \tag{3.28}$$

where $b = \frac{2\sqrt{\bar{h}\kappa_1 d_1}}{\lambda_0{}^2(\kappa d)_e w}$, $f_1 = \frac{\bar{h}\alpha_1}{2\pi\kappa_1 d_1}$ and $f_2 = \frac{\lambda_0{}^2\alpha_e}{2\pi}$. The approximation is valid if $\delta L' > 2$.

$$\upsilon = \left[\bar{h}(w + 2d + 2d_2) + \frac{1}{1+sM_s}\frac{2\kappa_1 d_1\delta}{\sinh(\delta L')} + \frac{2\bar{h}}{\delta}\tanh\left(\frac{\delta L'}{2}\right)\right]\tilde{T}_a + \frac{2\bar{I}\tilde{i}\bar{R}_a}{l} \tag{3.29}$$

$$\sigma = \varepsilon\left\{\frac{2\bar{I}\tilde{i}R_0\alpha_R}{l} - (w + 2d + 2d_2)\tilde{h} - \left[\frac{\delta}{\tanh(\delta L')} - \frac{\delta_0}{\tanh(\delta_0 L')}\right]\frac{2\alpha_1\tilde{h}}{s}\right\} \tag{3.30}$$

The above differential equation can be solved with the help of the boundary condition

$T_t(\pm\frac{l}{2}) = \frac{\tilde{T}_a}{1+sM_s}$ and symmetry $T_t(-x) = T_t(x)$. The solution is

$$T_t = \frac{1}{(\kappa d)_e w}\left\{\begin{array}{l} \dfrac{\upsilon+\sigma}{\lambda^2} - \dfrac{\sigma}{\lambda^2 - {\lambda_0}^2}\dfrac{\cosh(\lambda_0 x)}{\cosh(\lambda_0 l/2)} \\ + \left[\dfrac{\sigma}{\lambda^2 - {\lambda_0}^2} - \dfrac{\upsilon+\sigma}{\lambda^2} + \dfrac{(\kappa d)_e w}{1+sM_s}\tilde{T}_a\right]\dfrac{\cosh(\lambda x)}{\cosh(\lambda l/2)} \end{array}\right\} \tag{3.31}$$

The average temperature fluctuation on the sensing element is

$$\begin{aligned} \bar{T}_t &= \frac{1}{1+sM_s}\frac{2}{\lambda l}\tanh\left(\frac{\lambda l}{2}\right)\tilde{T}_a \\ &+ \frac{1}{(\kappa d)_e w}\left\{\frac{\upsilon+\sigma}{\lambda^2}\left[1-\frac{2}{\lambda l}\tanh\left(\frac{\lambda l}{2}\right)\right] - \frac{\sigma}{\lambda^2-{\lambda_0}^2}\left[\frac{2}{\lambda_0 l}\tanh\left(\frac{\lambda_0 l}{2}\right) - \frac{2}{\lambda l}\tanh\left(\frac{\lambda l}{2}\right)\right]\right\} \end{aligned} \tag{3.32}$$

The resulting sensor resistance change is

$$\Delta R(s) = \alpha_R \bar{T}_t R_0 = r_b(s)\frac{\tilde{i}}{\bar{I}} + G_h(s)\frac{\tilde{h}}{\bar{I}} + G_T(s)\frac{\tilde{T}_a}{\bar{I}} \tag{3.33}$$

and the sensor voltage change is

$$v(s) = \bar{I}\Delta R(s) + \tilde{i}\bar{R} = [r_b(s) + \bar{R}]\tilde{i} + G_h(s)\tilde{h} + G_T(s)\tilde{T}_a \tag{3.34}$$

where

$$r_b(s) = \frac{2\alpha_R \bar{I}^2 {R_0}^2}{{\lambda_0}^2(\kappa d)_e wl}\left\{\begin{array}{l} \dfrac{1+\alpha_R(\varepsilon+\bar{T}_a - T_0)}{(\lambda/\lambda_0)^2}\left[1-\dfrac{2}{\lambda l}\tanh\left(\dfrac{\lambda l}{2}\right)\right] \\ - \dfrac{\alpha_R \varepsilon}{(\lambda/\lambda_0)^2 - 1}\dfrac{2}{\lambda_0 l}\left[\tanh\left(\dfrac{\lambda_0 l}{2}\right) - \dfrac{\lambda_0}{\lambda}\tanh\left(\dfrac{\lambda l}{2}\right)\right] \end{array}\right\} \tag{3.35}$$

is the difference between the ac and dc resistance of the sensor,

$$\begin{aligned} G_h(s) = -\frac{\alpha_R \varepsilon \bar{I} R_0}{{\lambda_0}^2(\kappa d)_e}&\left\{\frac{{\lambda_0}^2}{\lambda^2}\left[1-\frac{2}{\lambda l}\tanh\left(\frac{\lambda l}{2}\right)\right] - \frac{1}{(\lambda/\lambda_0)^2-1}\frac{2}{\lambda_0 l}\left[\tanh\left(\frac{\lambda_0 l}{2}\right) - \frac{\lambda_0}{\lambda}\tanh\left(\frac{\lambda l}{2}\right)\right]\right\} \\ &\left\{1 + \frac{2d+2d_2}{w} + \left[\frac{\delta}{\tanh(\delta L')} - \frac{\delta_0}{\tanh(\delta_0 L')}\right]\frac{2\alpha_1}{sw}\right\} \end{aligned} \tag{3.36}$$

is the ac voltage sensitivity to heat transfer coefficient, and

$$G_T(s) = \frac{\alpha_R \bar{I} R_0}{1 + sM_s} \frac{2}{\lambda l} \tanh\left(\frac{\lambda l}{2}\right) + \frac{\alpha_R \bar{I} R_0}{\lambda^2 (\kappa d)_e w} \left[1 - \frac{2}{\lambda l} \tanh\left(\frac{\lambda l}{2}\right)\right] \left[\bar{h}(w + 2d + 2d_2) + \frac{1}{1 + sM_s} \frac{2\kappa_1 d_1 \delta}{\sinh(\delta L')} + \frac{2\bar{h}}{\delta} \tanh\left(\frac{\delta L'}{2}\right)\right] \tag{3.37}$$

is the ac voltage sensitivity to ambient temperature fluctuation. The first term in Eq. (3.34) represents the voltage drop on a impedance, while the second and third terms represent controlled ac voltage sources. Figure 3.5 shows the equivalent circuit of the sensor.

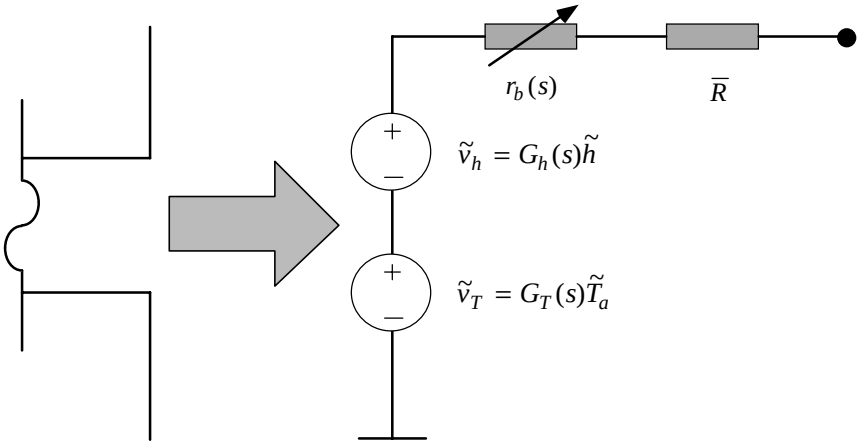

Figure 3.5 (a) Symbol of the shear stress sensor. (b) Equivalent ac circuit model.

3.4 Calibration and Analysis

3.4.1 *I-V* Measurement

The steady-state voltage drop on the sensor is

$$\bar{V} = \bar{I} R_0 [1 + \alpha_R (\bar{T}_s - T_0)] = \bar{I} \bar{R}_a \left\{1 + \frac{\alpha_R \bar{I}^2 R_0}{{\lambda_0}^2 (\kappa d)_e wl} \left[1 - \frac{2}{\lambda_0 l} \tanh\left(\frac{\lambda_0 l}{2}\right)\right]\right\} \tag{3.38}$$

The over-heat ratio of the sensor can be expressed as

$$a_R = \frac{\alpha_R \bar{I}^2 R_0}{\lambda_0{}^2 (\kappa d)_e wl}\left[1 - \frac{2}{\lambda_0 l}\tanh\left(\frac{\lambda_0 l}{2}\right)\right] \tag{3.39}$$

For the micromachined shear stress sensors, polycrystalline silicon is used as the sensing wire material and low stress silicon nitride as the diaphragm material. The resistance - temperature relationship of the sensors are calibrated. The results (Figure 3.6) show a 2.5% non-linearity over a temperature range of 200°C. The above derivations are still valid if α_R is replaced by the average resistance coefficient of temperature (~ 0.11%/°C) extrapolated from the fit to the data in Figure 3.6.

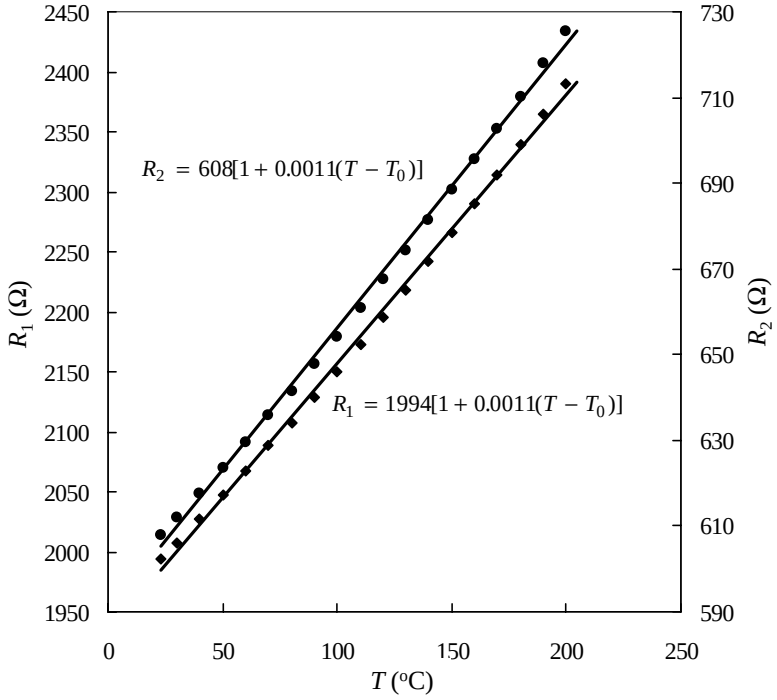

Figure 3.6 The measured resistance-temperature relationships of two boron-doped polysilicon resistors with doping concentration of 2×10^{20} cm^{-3}.

The other physical properties of polysilicon and silicon nitride can be found from various literature. They are: $\rho_0 = 1\times10^{-3}$ Ω·cm, $\kappa = 0.3$ W/cm·°C, $c_p = 0.7$ J/g·°C, $\rho = 2.32$ g/cm^3, $\kappa_1 = 0.032$ W/cm·°C, $c_{p1} = 0.7$ J/g·°C, $\rho_1 = 3.0$ g/cm^3, and $\alpha_1 = 0.015$ cm^2/s. The

dimensions of the sensor structure are: d = 0.55 μm, l = 150 μm, L = 210 μm, d_1 = 1.4 μm, d_2 = 0.2 μm. Then we have $(\kappa d)_e = 2.1\times10^{-5}$ W/°C, α_e = 0.0547 cm^2/s. After fitting Eq. (3.38) and Eq. (3.39) to the *I*-*V* data measured in still air at $T_a = T_0 = 22\,^{o}$C for sensors with different widths (Figure 3.7 and Figure 3.8), we found that the average value of $\bar{h}$ is 0.262 W/cm^2·°C. Note that the convective heat transfer coefficient is non-zero even in still air because there exists the natural or free convection. By using this value of $\bar{h}$, all the parameters in the above equations are calculated and listed in Tables 3.1 and 3.2 for $T - T_a = 100\,^{o}$C.

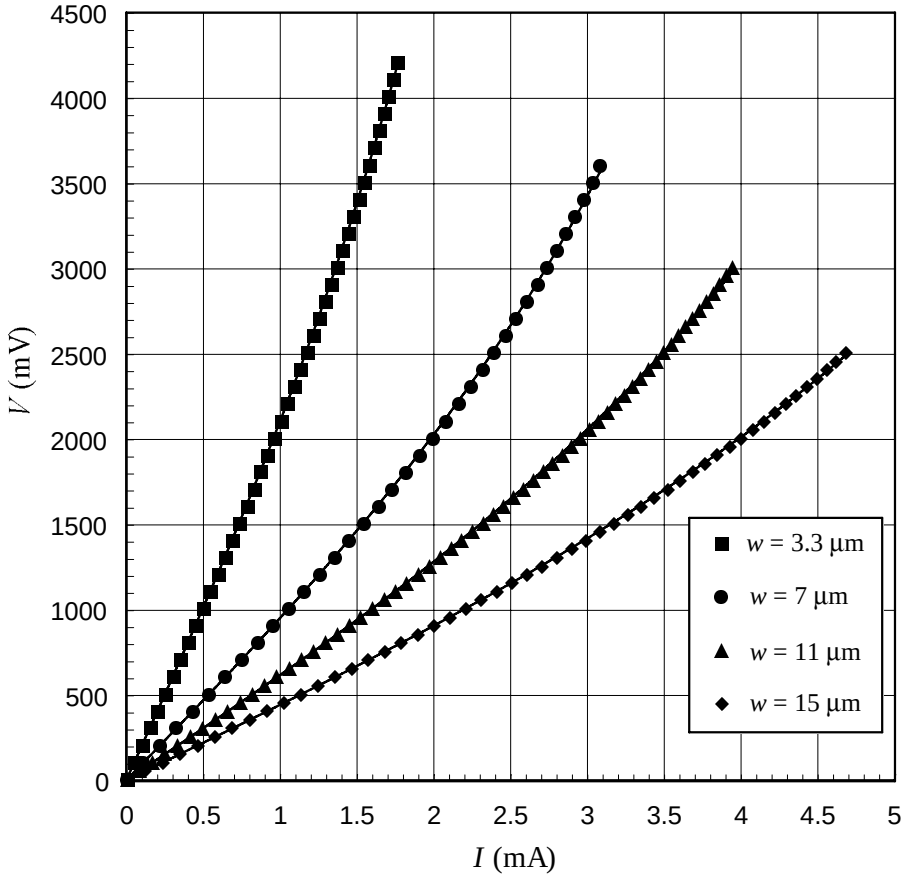

Figure 3.7 Measured *V*-*I* curves (symbols) of the sensors with different widths together with the fitted curves (solid lines) of Eq. (3.38).

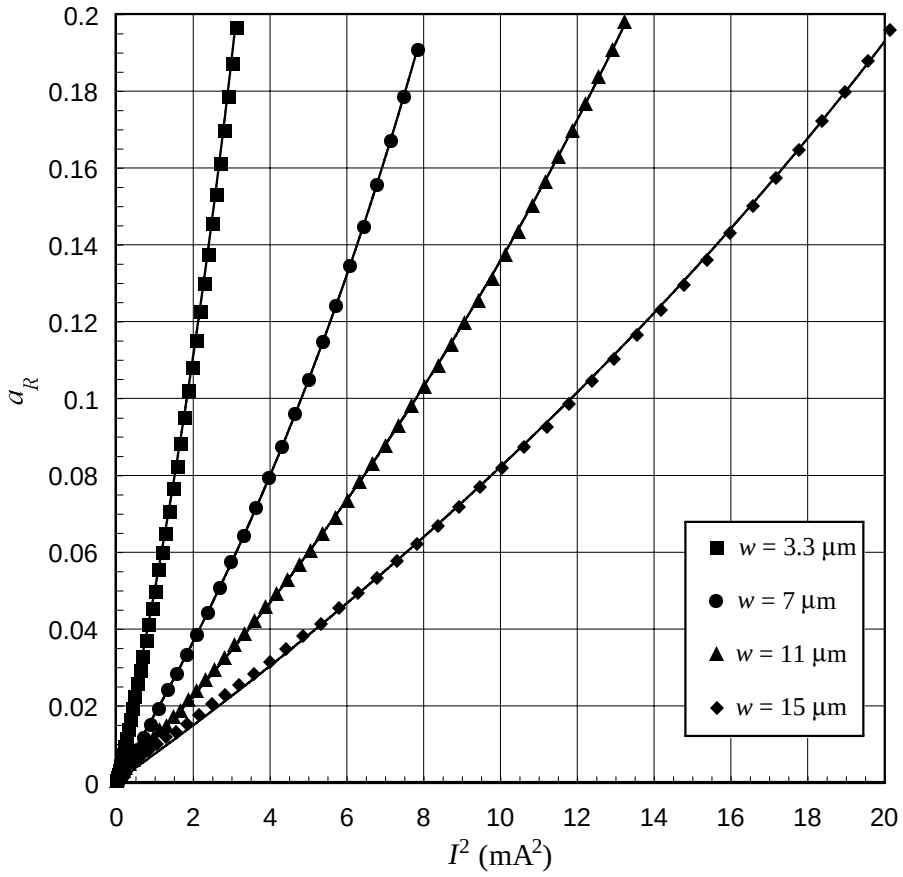

Figure 3.8 The over-heat ratio of the sensors calculated from the measured *I-V* data are plotted against the square of the heating current. The solid lines are the fitted curves of Eq. (3.39).The fitting parameter $\bar{h}$ is found to be 0.262.

Table 3.1 Parameters calculated from measured *I-V* curves.

w (μm)	R_a (Ω)	V (mV)	I (mA)	λ (cm^{-1})	$\alpha_R\varepsilon$	$\lambda l/2$	$\delta L'$
3.3	1994	2976	1.357	516.2	0.1348	3.872	2.491
7	930	2249	2.198	351.5	0.1601	2.636	2.455
11	608	1872	2.799	288.1	0.1820	2.161	2.406
15	438	1665	3.455	252.2	0.2020	1.892	2.358

The temperature distribution on the diaphragm of the sensors can be calculated by using Eqs. (3.6), (3.14) and (3.21). Figure 3.9 shows the contour plot of the 3.3 μm wide

sensor at an over-heat ratio of 0.1. However, it needs to be verified by experimental measurement such as infrared thermal imaging.

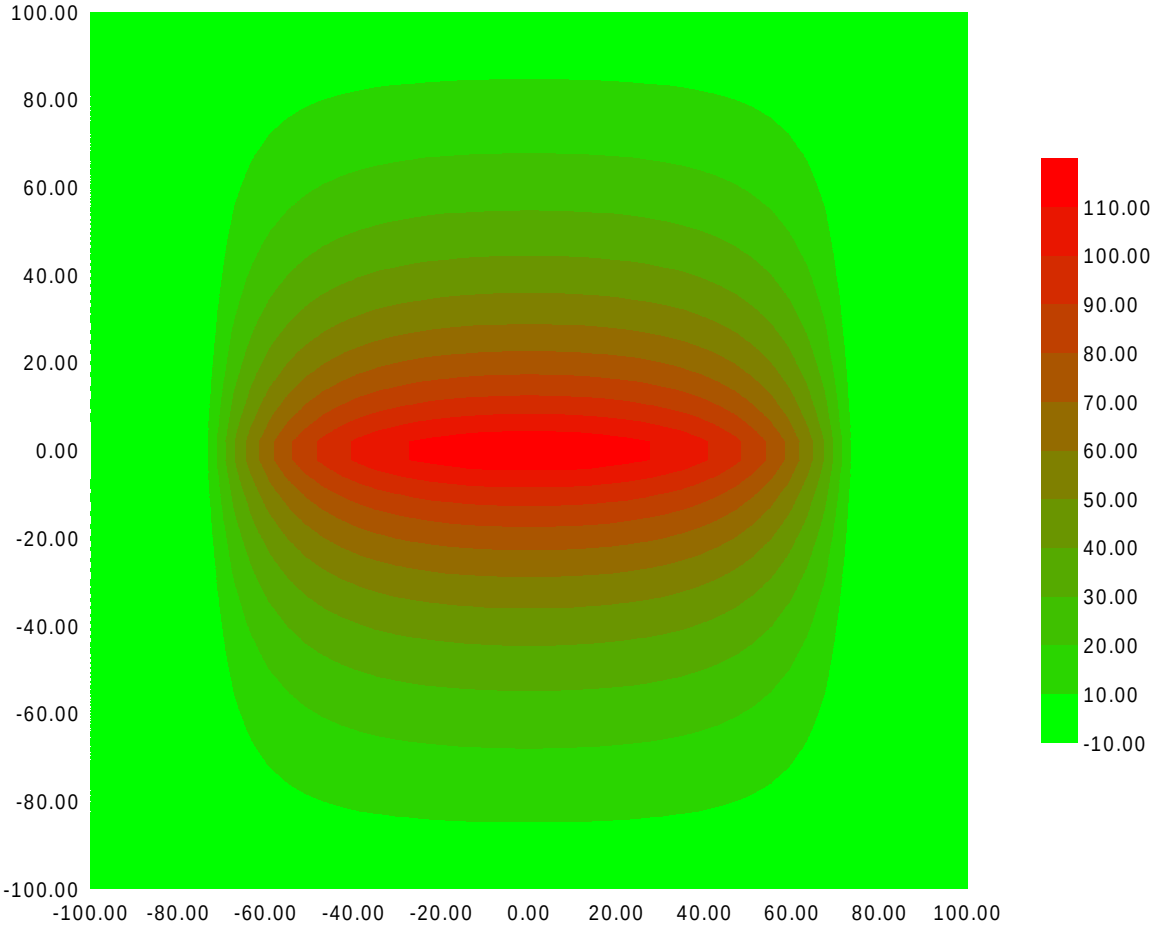

Figure 3.9 Calculated temperature distribution (relative to room temperature) on the diaphragm of the 3.3 μm wide sensor at an over-heat ratio of 0.1.

3.4.2 Temperature Sensitivity

In constant current (CC) mode, when $\overline{h}$ is kept constant, the only parameter in Eq. (3.38) that changes with ambient temperature $\overline{T}_a$ is $\overline{R}_a$. Therefore, the output voltage is a linear function of the ambient temperature and its sensitivity to ambient temperature change is

$$\left.\frac{\partial \overline{V}}{\partial \overline{T}_a}\right|_{CC} = \alpha_R \bar{I} R_0 (1 + a_{R0}) = \alpha_R \overline{V}_0 \tag{3.40}$$

where

$$a_{R0} = \frac{\overline{R} - R_0}{R_0} = \alpha_R (\overline{T}_a - T_0) \tag{3.41}$$

is the sensor resistance over-heat ratio at room temperature T_0. The measured sensitivities labeled in Figure 3.10 are in good agreement with those calculated from Eq. (3.40).

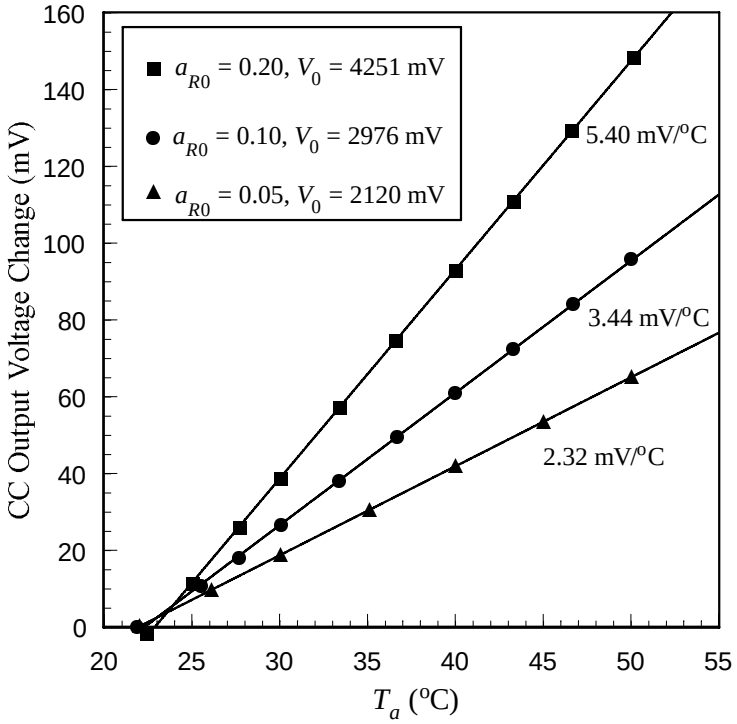

Figure 3.10 Output voltage sensitivity of the sensor to ambient temperature in CC mode.

The conventional constant temperature (CT) anemometer circuit shown in Figure 2.13 with temperature insensitive bridge resistors keeps the sensor resistance and hence the sensor temperature constant. In CT mode, both $\bar{I}$ and $\overline{R}_a$ change with $\overline{T}_a$. The theoretical $\overline{V} - \overline{T}_a$ curves calculated from Eq. (3.38) (Figure 3.11) exhibit severe non-linearity when the ambient temperature becomes close to the sensor temperature. For

small fluctuation of ambient temperature around room temperature, the temperature sensitivity can be expressed as

$$\left.\frac{\partial \overline{V}}{\partial \overline{T}_a}\right|_{CT} \approx -\left(1+\frac{1}{a_R}\right)\frac{\alpha_R V_0}{2} \tag{3.42}$$

which means that the temperature sensitivity is higher when the sensor is operated at smaller over-heat ratio. The sensitivities extracted from the experimental results shown in Figure 3.11 are close to those calculated from the above equation (-14.0 mV/^{o}C, -17.9 mV/^{o}C and -24.7 mV/^{o}C for a_R = 0.2, 0.1 and 0.05 respectively). However, the results for small over-heat ratios deviate significantly from the theoretical curves. As a matter of fact, the measured $\overline{V} - \overline{T}_a$ relationships are more linear than expected.

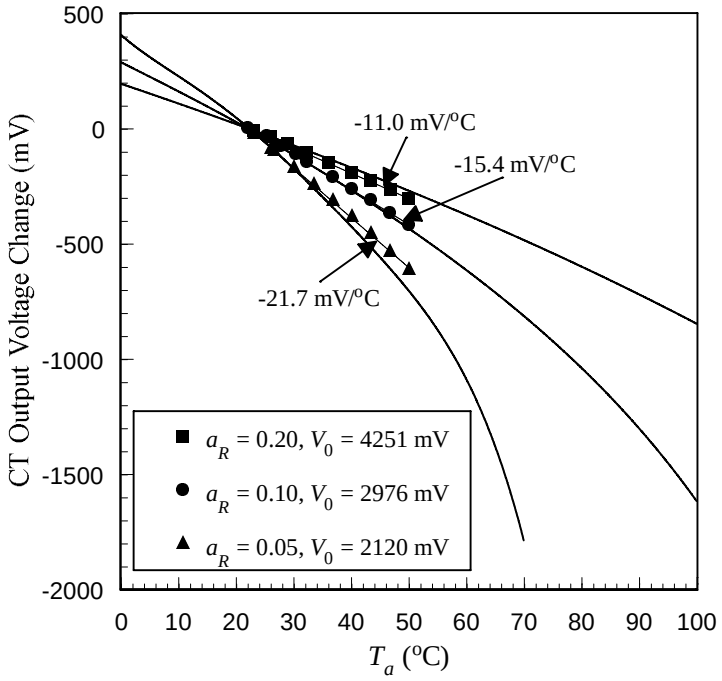

Figure 3.11 Ambient temperature sensitivity of the sensor output voltage in CT mode. The sensor temperatures corresponding to the over-heat ratios of 0.05, 0.10 and 0.20 are 73^{o}C, 123 ^{o}C and 223 ^{o}C respectively.

In an ideal CT mode, the sensor temperature is preset to a value by the three temperature-insensitive bridge resistors. Obviously, the sensor will not function when the ambient temperature becomes equal to the preset sensor temperature. Therefore, in most

applications, the sensor is operated at a temperature significantly higher than the room temperature to avoid the situation. This has the additional advantage of reducing and linearizing (for easy compensation) the output drift with ambient temperature. However, in some applications, such as in underwater measurement, high operating temperature is undesirable. This problem can be solved by integrating the bridge resistor R_3 (or all of the resistors) with the sensor on the same chip. Because the bridge resistors are in direct contact with the substrate, they will not be heated up by electrical current. However, their resistance will change with ambient temperature since the resistors and the sensor are made of the same material and they all have the same temperature coefficient of resistance. As a result, we have

$$\overline{T}_s - \overline{T}_a = [1 + \alpha_R(\overline{T}_a - T_0)]\frac{a_{R0}}{\alpha_R} = \frac{\overline{R}_a}{R_0}\frac{a_{R0}}{\alpha_R} \tag{3.43}$$

i.e., the temperature difference between the sensor and the ambient is proportional to $\overline{R}_a$. According to Eq. (3.21), $\bar{I}$ is not a function of $\overline{T}_a$ and the temperature sensitivity then is

$$\frac{\partial \overline{V}}{\partial \overline{T}_a} = \alpha_R \bar{I} R_0 \frac{\partial \overline{T}_s}{\partial \overline{T}_a} = \alpha_R \overline{V}_0 \tag{3.44}$$

which is the same as that in CC mode. Note that the sensor temperature does not change with the heat transfer coefficient. Therefore, the sensitivity to heat transfer is the same as that in CT mode.

In conclusion, this type of simple compensation results in a new mode having the advantages of both CC mode (low temperature sensitivity) and CT mode (high sensitivity to heat transfer coefficient, as will be demonstrated in the next section) at any operation temperature.

3.4.3 Sensitivity to Shear Stress

The output sensitivity to heat transfer in CC mode

$$\left.\frac{\partial \bar{V}}{\partial \bar{h}}\right|_{CC} = -\frac{\alpha_R \bar{I}^3 R_0 \bar{R}_a}{{\lambda_0}^4 (\kappa d)_e{}^2 wl}\left[1-\frac{3}{\lambda_0 l}\tanh\left(\frac{\lambda_0 l}{2}\right)+\frac{1}{2\cosh^2(\lambda_0 l/2)}\right] \left[1+\frac{2d+2d_2}{w}+\frac{1/(\delta_0 w)}{\tanh(\delta_0 L')}-\frac{L'/w}{\sinh^2(\delta_0 L')}\right] \tag{3.45}$$

and the sensitivity to heat transfer in CT mode

$$\left.\frac{\partial \bar{V}}{\partial \bar{h}}\right|_{CT} = \frac{\dfrac{\bar{V}}{2\lambda^2(\kappa d)_e}\left[1+\dfrac{2d+2d_2}{w}+\dfrac{1/(\delta w)}{\tanh(\delta L')}-\dfrac{L'/w}{\sinh^2(\delta L')}\right]}{\left[1-\dfrac{2}{\lambda l}\tanh(\dfrac{\lambda l}{2})\right]\Big/\left[1-\dfrac{3}{\lambda l}\tanh(\dfrac{\lambda l}{2})+\dfrac{1}{2\cosh^2(\dfrac{\lambda l}{2})}\right]+\dfrac{\alpha_R \bar{I}^2 R_0}{\lambda^2 (\kappa d)_e wl}} \tag{3.46}$$

are still functions of the heat transfer coefficient, as shown in Figure 3.12. However, in a sufficiently small range, the output voltage changes are proportional to the change of heat transfer coefficient in small range (Figure 3.13).

The relationship between the heat transfer coefficient h and the wall shear stress τ_w when the sensor is flush-mounted on the wall has been experimentally determined or theoretically derived by a number of researchers [8,9,11,19]. The most general expression is the one reported by Brown, who included the effect of pressure gradient, that is,

$$Nu^3 = A\tau_w + \frac{B}{Nu}\frac{dp}{dx}L \tag{3.47}$$

where A and B are constants, *Nu* is the *Nusselt* number, which is defined as $h_c l/\nu$ with l being the characteristic length, L the effective length of the sensor in the streamwise direction, and $h_c = \Delta h$ the heat transfer coefficient caused by forced convection. If the pressure drop across the sensor is small, which is usually the case for our micro sensors in subsonic flow, the second term in the above equation can be neglected. Then we have

$$h_c = \Delta h \propto {\tau_w}^{1/3} \tag{3.48}$$

The measured output voltage changes in CC and CT modes with wall shear stress are plotted in Figure 3.14 and Figure 3.15 respectively. The solid lines in the figures are

polynomial fittings. By comparing these measured data with the calculated data (Figure 3.12), we found that the maximum variation of the heat transfer coefficient in our calibration is less than 0.016 W/cm^{2}.^{o}C or about 6%, well in the linear region of the $\Delta\overline{V} - \Delta\overline{h}$ curves in Figure 3.13. Theoretically, if we plot the voltage change against $\tau_w^{1/3}$, we should be able to get straight lines, except in the very low shear stress region, where measurement errors and non-idealities occur. However, in reality, when the shear stress range is less than 1 Pa, it is difficult to determine the exponent to the shear stress because the accuracy of fitting is not very sensitive to it.

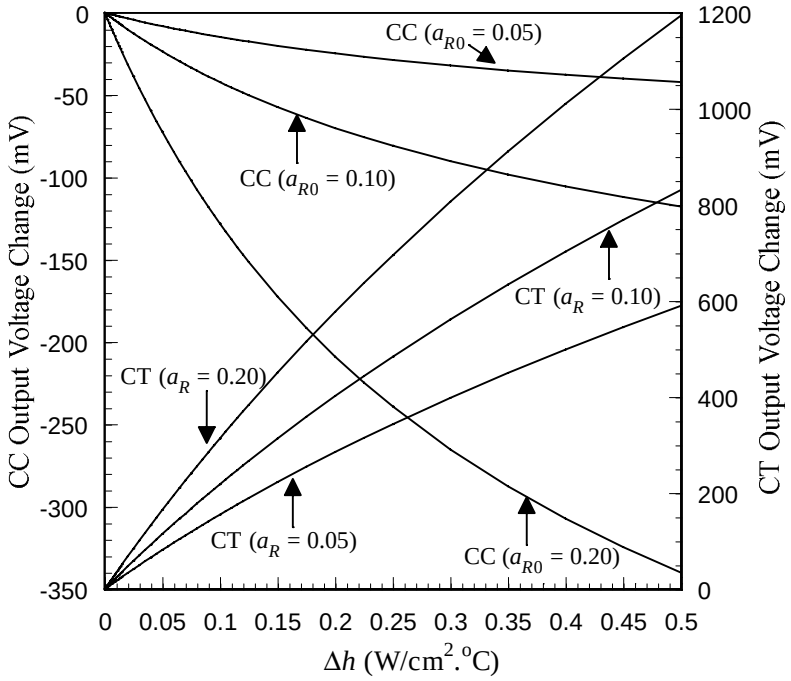

Figure 3.12 Output voltage changes as a function of heat transfer coefficient at different over-heat ratios for the 3.3 μm wide sensor.

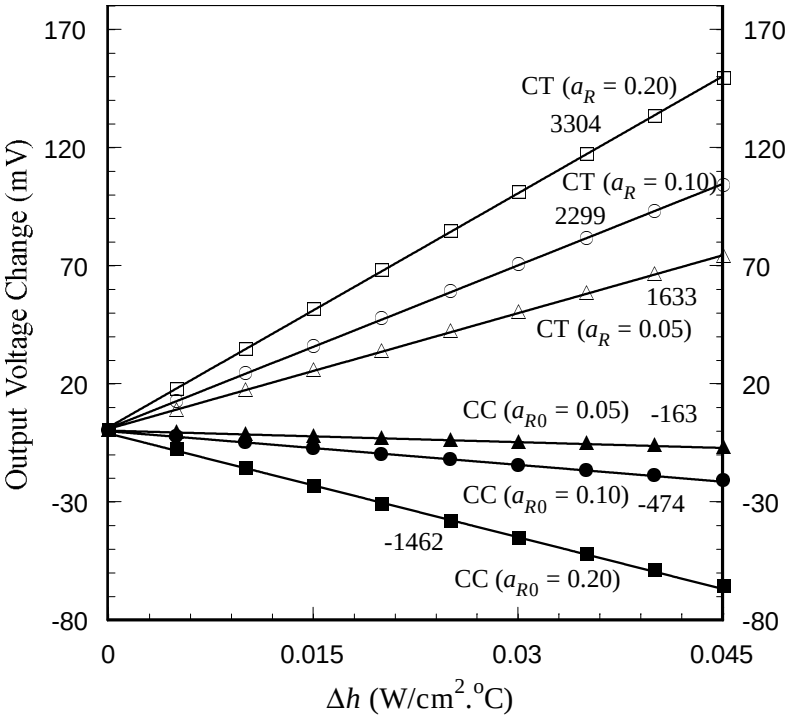

Figure 3.13 Zoom-in of the calculated $\overline{V}$ – $\Delta\overline{h}$ curves in the linear region.

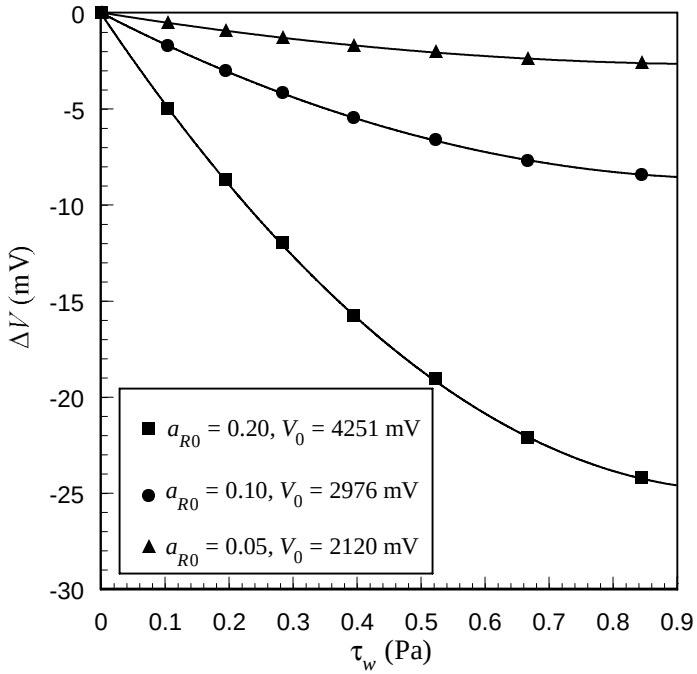

Figure 3.14 Output voltage changes in CC mode at different over-heat ratios. The normalized output ($\Delta V/V_0$) increases dramatically with over-heat ratio.

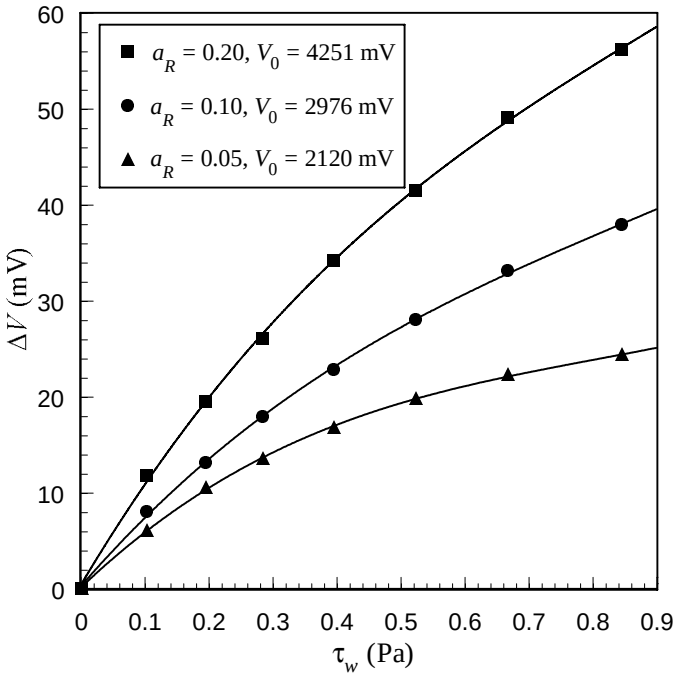

Figure 3.15 Output voltage changes in CT mode at different over-heat ratios. The normalized output is almost insensitive to the over-heat ratio.

Both the theoretical calculations and experimental data have shown that the normalized output in CC mode increases dramatically for larger over-heat ratio, which implies high over-heat ratio for CC operation in order to get enough sensitivity. For CT operation, the normalized output is almost insensitive to the over-heat ratio in CT mode. However, reasonably high over-heat ratio is still preferred to avoid excessive temperature sensitivity.

The drift of the sensitivity to heat transfer with ambient temperature can be estimated from Eqs. (3.45) and (3.46). In CC mode, this drift is linearly proportional to the ambient temperature change with the coefficient of proportionality being $\alpha_R \approx 0.1\%/^{o}C$. In CT mode, the sensitivity - ambient temperature relationship has been numerically calculated and is plotted in Figure 3.16. The drift rates around room temperature are labeled next to each curve. In all cases, the drift rate is no more than $1\%/^{o}C$ and can be neglected when the sensors are used in laboratory measurement where ambient temperature change is

only a few degrees. For applications where ambient temperatures varies significantly, temperature compensation to the output voltage is necessary. This may be complicated at small over-heat ratio in CT mode due to the high non-linearity. If the integrated bridge temperature compensation scheme described in the previous section can be used, the drift of sensitivity with ambient temperature in CT mode becomes that in CC mode and can be further reduced by linear compensation.

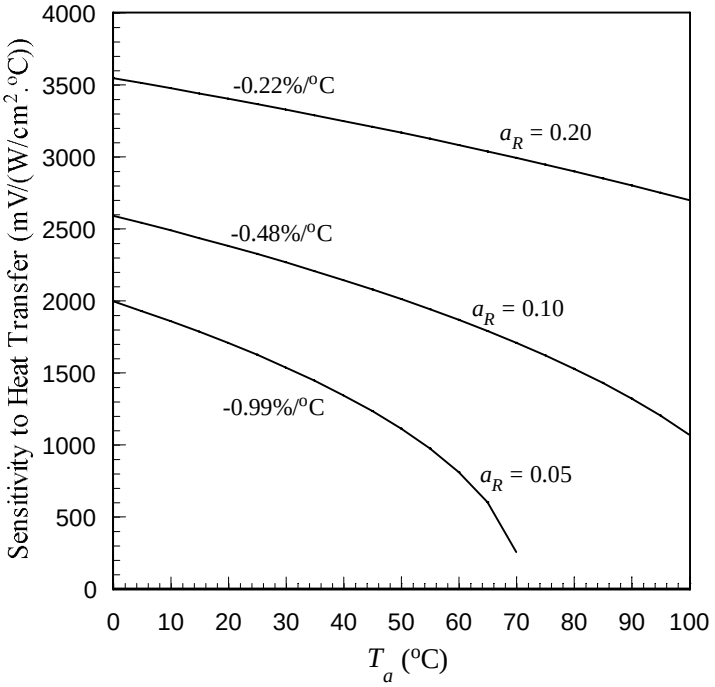

Figure 3.16 The drift of the sensitivity to heat transfer coefficient with ambient temperature in CT mode.

Finally, Figure 3.17 shows that wind-tunnel calibration results of the sensors with different widths. This time, we have plotted the normalized voltage changes against $\tau_w^{1/3}$. Again, the normalized sensitivity is almost independent of the sensor width.

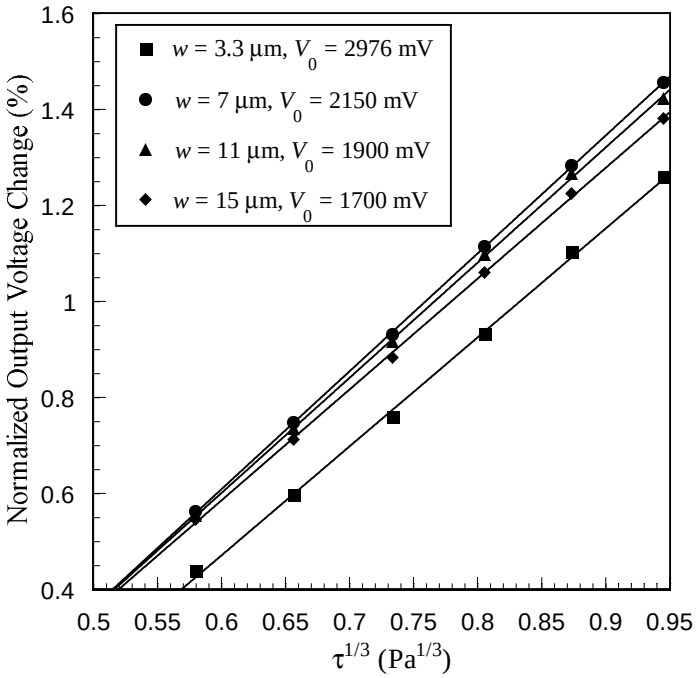

Figure 3.17 Wind-tunnel calibration results of the sensors with different width at the over-heat ratio of 0.1.

3.4.4 Frequency Responses in CC Mode

The frequency response of r_b(s) is the only one among the three ac components in the equivalent circuit of the sensor that can be experimentally measured since standard perturbation on heat transfer or wall shear stress and ambient temperature are not readily available. The simple circuit shown in Figure 3.18 has been used to do the measurement. The function generator supplies both the dc bias and the ac sine wave signal to the Wheatstone bridge through a wide-band voltage follower. The values of R_1, R_2 and R_3 are chosen such that $R_1 R_3 = R_2 R_0 (1 + a_R)$, where a_R is the desired over-heat ratio of the sensor. The dc output of the bridge can be nulled by adjusting the dc bias. At that point, we know that the sensor has been biased at the right over-heat ratio. The amplitude of the sine wave is set to about 3% of the dc bias to satisfy the small signal condition. The frequency of the sine wave is swept from 2 Hz to 100 kHz while the magnitude and phase of the amplified output are recorded. The magnitude and phase of $r_b(i\omega)$ can thus be calculated from these measurement results by

$$\left|r_b(i\omega)\right| = \frac{\left(1+\frac{R_3}{R_2}\right)R_1}{\left\{\left[\frac{R_2}{R_2+R_3}\left|\frac{Gv_i(i\omega)}{v_o(i\omega)}\right|\right]^2 - \frac{2R_2\cos\theta}{R_2+R_3}\left|\frac{Gv_i(i\omega)}{v_o(i\omega)}\right| + 1\right\}^{\frac{1}{2}}} \tag{3.49}$$

$$\phi = -\tan^{-1}\frac{\sin\theta}{\cos\theta - \frac{R_2+R_3}{R_2}\left|\frac{v_o(i\omega)}{Gv_i(i\omega)}\right|} \tag{3.50}$$

where v_i is the input signal from the function generator, v_o is the amplified output signal, G is the gain of the amplifier after the Wheatstone bridge and θ is the phase of the output signal.

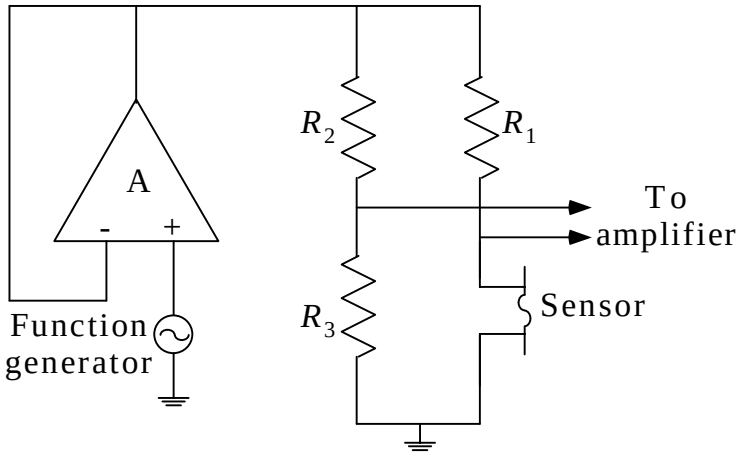

Figure 3.18 Circuit used in measuring the frequency response of the sensors in CC mode.

The Bode plots of the magnitude and phase responses for the sensors with different widths are shown in Figure 3.19 and Figure 3.20 respectively. The solid lines are the fitted curves of Eq. (3.35) using the parameters in Tables 3.1 and 3.2. Note that the fitting parameters f_1 and f_2 are in reasonably good agreement with their calculated values.

Table 3.2 Calculated and fitted parameters for the study of dynamic responses.

w (μm)	b	f_1 (Hz)		f_2 (Hz)	
	Calculated	Calculated	Fitted	Calculated	Fitted
3.3	1.173	140	133	2322	3400
7	1.193	140	135	1076	1150
11	1.130	140	130	723	690
15	1.081	140	126	554	480

Unlike the conventional hot-wire anemometers and flush-mountable hot-film sensors, which have constant high frequency roll-off of 20 dB/dec. [20,21] and 10 dB/dec. [22] respectively, the micromachined shear stress sensors do not exhibit a constant roll-off at high frequency. Their frequency responses are the result of the coupling of two critical frequencies, f_1 and f_2. f_1 represents the thermal response of the diaphragm and is virtually independent of the sensor width; f_2 represents the thermal response of the sensing element and decreases with increasing sensor width. As a matter of fact, this model can be used to qualitatively explain the behavior of hot-wire and hot-film sensors. For a free-standing hot wire (i.e., no substrate), f_1 is infinity and according to Eqs. (3.35) and (3.28), the maximum attenuation rate of the magnitude-frequency response is inversely proportional to the frequency with f_2 being the corner frequency. For a hot-film sensor (thin metal sensing element directly sitting on thick and flat substrate, such as quartz), f_1 is typically a few Hz, while f_2 is usually in the kilo-Hertz range. Therefore the maximum attenuation rate of the magnitude-frequency response is inversely proportional to the square root of frequency in the region between 10 Hz to 1 kHz.

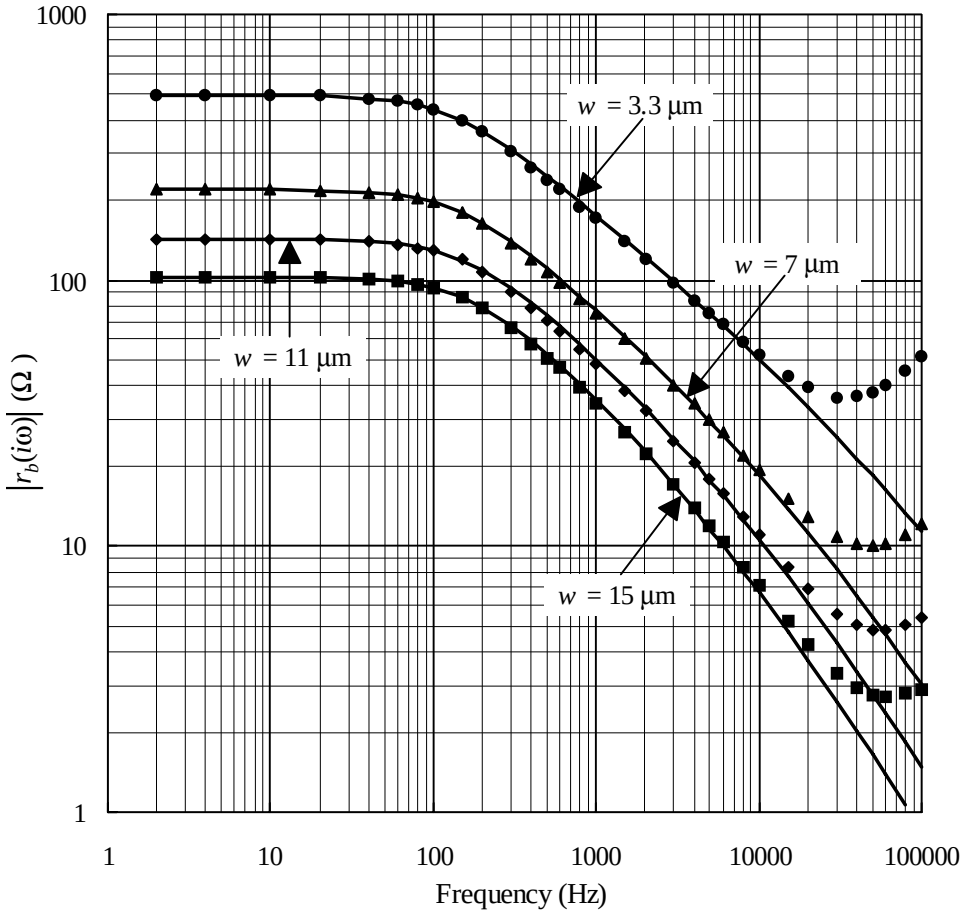

Figure 3.19 Magnitude responses of $r_b(i\omega)$ for sensors with different widths.

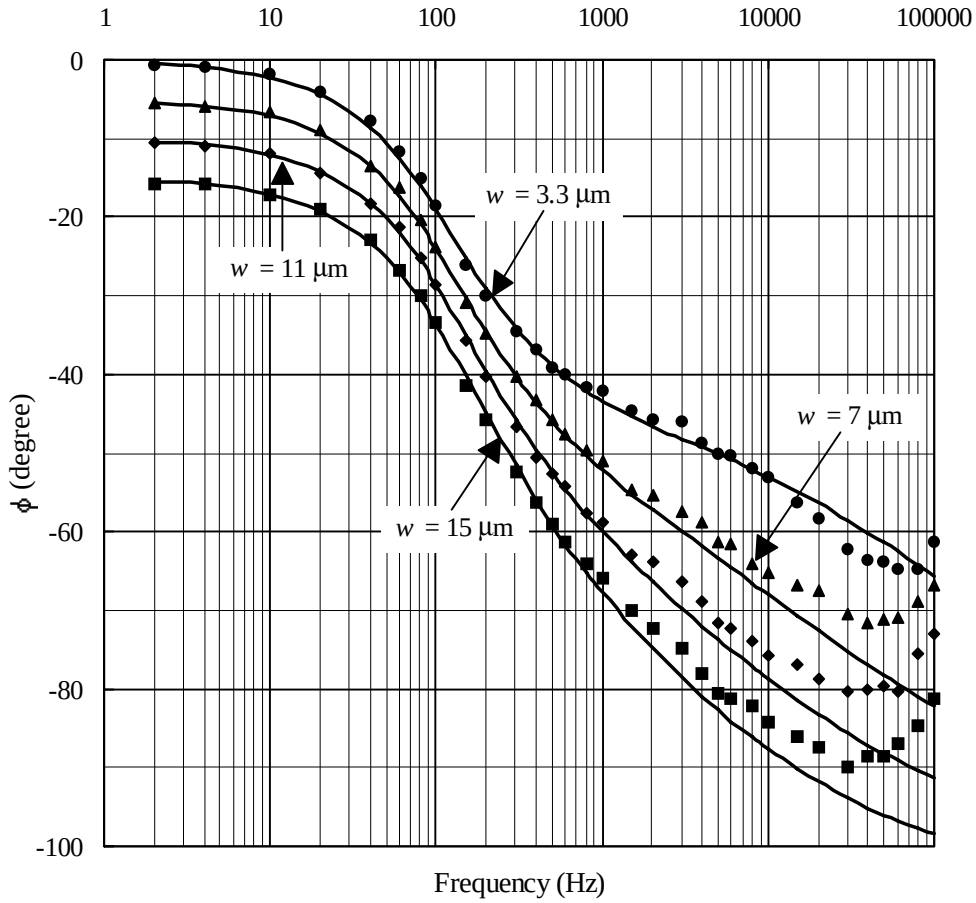

Figure 3.20 Phase responses of $r_b(i\omega)$ for sensors with different widths. Note that the curves for 7 μm, 11 μm and 15 μm have been shifted down by 5, 10 and 15 degrees respectively to avoid overlapping with other curves.

As can be seen from the figures, the experimental data points start to deviate from the theoretical curves at frequency of 10 kHz. It is even more surprising that, above certain frequency (40 kHz, 60 kHz, 80 kHz and 80 kHz for w = 3.3 μm, 7 μm, 11 μm and 15 μm respectively), the magnitude of r_b increases with frequency. This abnormal effect is obviously caused by the parasitic components from the sensing element in the measurement circuit.

Finally, the voltage sensitivity $G_h(i\omega)$ and $G_T(i\omega)$ are plotted against the excitation frequencies. They both have a corner frequency at about 130 Hz. It is interesting that these two sensitivities attenuate at frequencies above f_1 with a constant rate of 20 dB/dec.,

even for all the sensors under study. This can be qualitatively explained by the simple heat transfer model of the sensor structure. Since the size of the sensing element is small, most of its generated heat is lost to the diaphragm, which in turn loses heat to the ambient. These two heat transfer steps each has an attenuation rate proportional to the square root of frequency. The overall attenuation is then proportional to the frequency.

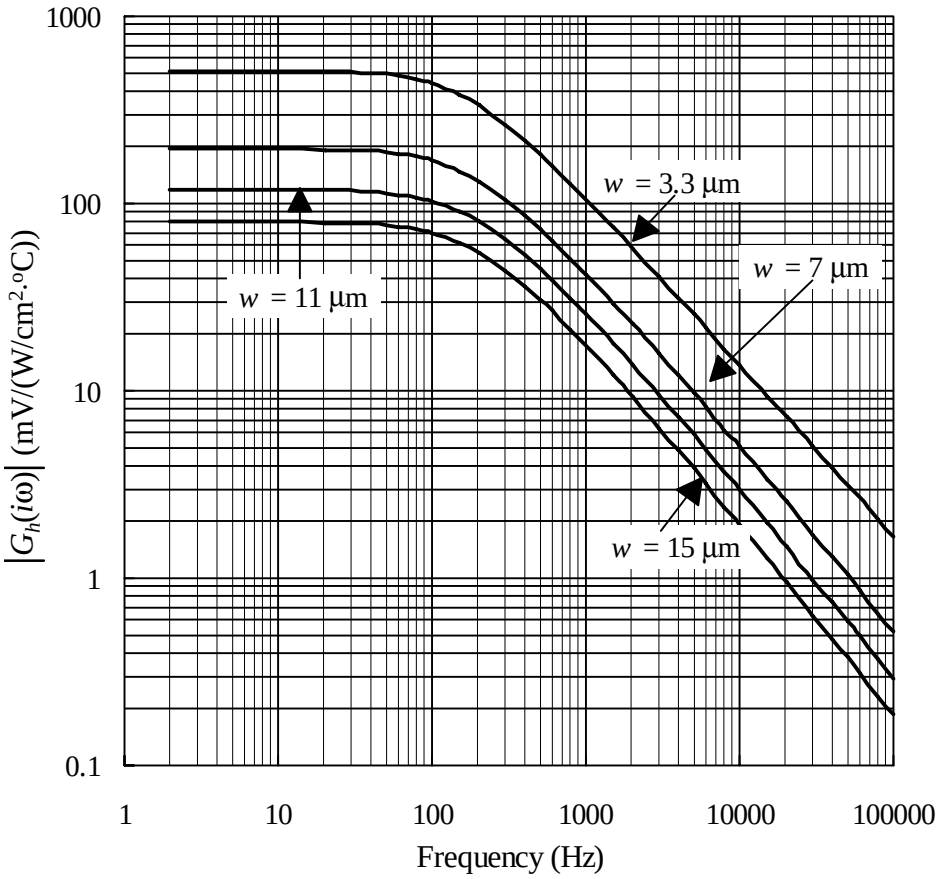

Figure 3.21 Magnitude responses of $G_h(i\omega)$.

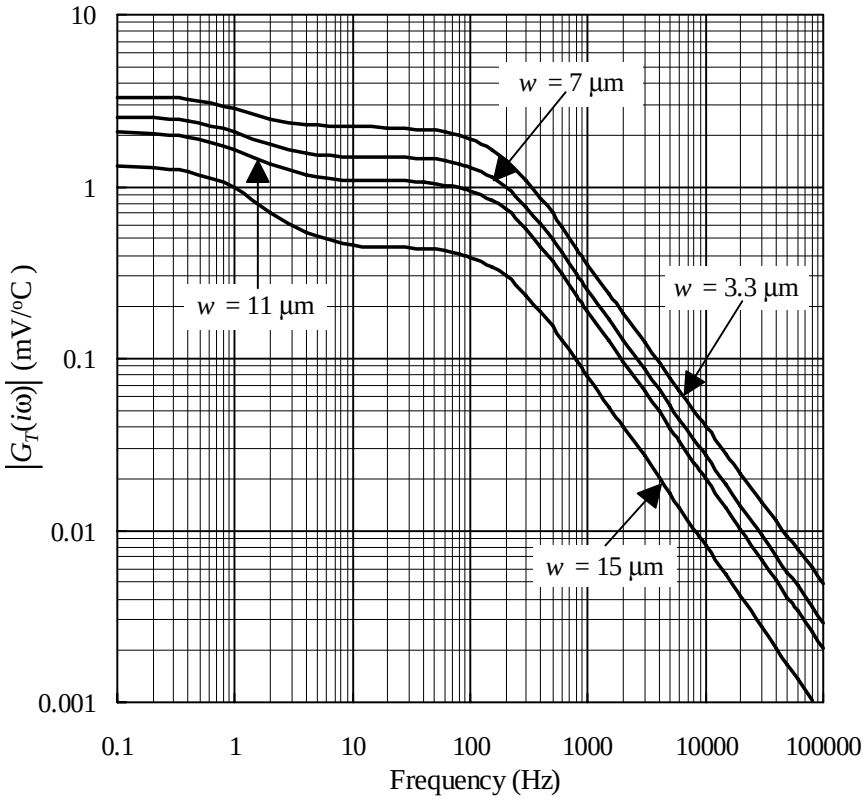

Figure 3.22 Magnitude responses of $G_T(i\omega)$.

In addition to the corner frequency at 130 Hz, $G_T(i\omega)$ has another much lower corner frequency at 1 Hz (assumed), as a result of the slow response of the silicon substrate to ambient temperature change. The ac temperature sensitivity on the second platform in the Bode plot is only 50% - 70% of that at steady state. This difference, if not corrected, could cause significant error in the measurement of temperature fluctuation.

3.4.5 Frequency Responses in CT Mode

Figure 2.13 is the schematic of the constant temperature bias circuit. It is easy to derive from the equivalent circuit of the sensor (Figure 3.5) and the basic circuit theory that the voltage at the non-inverting input terminal of the operational amplifier is

$$v_+ = R_2' \| R_3' \left(\frac{v_o}{R_2} + \frac{v_t}{R_t} \right) \tag{3.51}$$

where $R_2' = R_2 \| R_t = \frac{R_2 R_t}{R_2 + R_t}$ and $R_3' = R_3 \| R_r = \frac{R_3 R_r}{R_3 + R_r}$, and the voltage at the inverting input terminal of the operational amplifier is

$$v_- = \frac{[\overline{R} + r_b(s)]v_o + R_1[G_h(s)\tilde{h} + G_T(s)\tilde{T}_a]}{R_1 + \overline{R} + r_b(s)} \tag{3.52}$$

Considering the great complexity of the expression for $r_b(s)$ (Eq. (3.35)), we will continue to use the symbol $r_b(s)$ and its polar expression $r_b(s) = |r_b|e^{i\phi}$ throughout the remaining derivation just for simplicity. The equation for an operational amplifier with two poles is

$$v_o = \frac{A_0 v_i}{(1 + \frac{s}{p_1})(1 + \frac{s}{p_2})} = \frac{A_0(v_+ - v_-)}{1 + sM' + s^2 M''} \tag{3.53}$$

where p_1 and p_2 are the first and second pole frequencies, $M' = \frac{1}{p_1} + \frac{1}{p_2}$ and $M'' = \frac{1}{p_1 p_2}$. Inserting Eqs. (3.51) and (3.52) into the above equation yields

$$\frac{1 + sM' + s^2 M''}{A_0} v_o = R_2' \| R_3' \left(\frac{v_o}{R_2} + \frac{v_t}{R_t} \right) - \frac{[\overline{R} + r_b(s)]v_o + R_1[G_h(s)\tilde{h} + G_T(s)\tilde{T}_a]}{R_1 + \overline{R} + r_b(s)} \tag{3.54}$$

$$\begin{aligned} v_o &= \frac{\frac{R_2' \| R_3'}{R_t} v_t - \frac{R_1[G_h(s)\tilde{h} + G_T(s)\tilde{T}_a]}{R_1 + \overline{R} + r_b(s)}}{\frac{1 + sM' + s^2 M''}{A_0} - \frac{R_2' \| R_3'}{R_2} + \frac{\overline{R} + r_b(s)}{R_1 + \overline{R} + r_b(s)}} \\ &= \frac{\frac{R_2' \| R_3'}{R_t}\left[\frac{R_1 + \overline{R}}{r_b(s)} + 1\right] v_t - \frac{R_1}{r_b(s)}[G_h(s)\tilde{h} + G_T(s)\tilde{T}_a]}{\left(\frac{1 + sM' + s^2 M''}{A_0} - \frac{R_2' \| R_3'}{R_2}\right)\left[\frac{R_1 + \overline{R}}{r_b(s)} + 1\right] + \frac{\overline{R}}{r_b(s)} + 1} \end{aligned} \tag{3.55}$$

Since the bridge is balanced in steady state, it is easy to show that

$$\frac{\overline{R}}{R_1} = \left[1 - \frac{R_2^{'} \| R_3^{'}}{R_2}\left(1 + \frac{R_2}{R_r}\frac{V_r}{V_o}\right)\right]^{-1} - 1 \tag{3.56}$$

For convenience, the resistors in the CT circuit are chosen such that $R_2 = R_3 << R_t = R_r$. Then,

$$\frac{\overline{R}}{R_1} = 1 + \frac{2R_2}{R_r}\left(\frac{V_r}{V_o} - 1\right) \tag{3.57}$$

$$\begin{aligned} v_o &= \frac{\frac{R_2}{2R_t}\left(\frac{2R_1}{|r_b|}e^{-i\phi} + 1\right)v_t - \frac{R_1}{r_b(s)}[G_h(s)\tilde{h} + G_T(s)\tilde{T}_a]}{\frac{sM^{'} + s^2M^{''}}{A_0}\left(\frac{2R_1}{|r_b|}e^{-i\phi} + 1\right) + \frac{R_2}{R_r}\left(1 + \frac{R_1}{|r_b|}\frac{V_r}{V_o}e^{-i\phi}\right) + \frac{1}{2}} \\ &= \frac{\frac{R_2}{R_t}\left[\left(1 + \frac{2R_1}{|r_b|}\cos\phi\right) - i\left(\frac{2R_1}{|r_b|}\sin\phi\right)\right]v_t - \frac{2R_1}{r_b(s)}[G_h(s)\tilde{h} + G_T(s)\tilde{T}_a]}{p(\omega) + iq(\omega)} \end{aligned} \tag{3.58}$$

where

$$p(\omega) = 1 + \frac{4\omega M^{'}}{A_0}\frac{R_1}{|r_b|}\sin\phi - \frac{2\omega^2 M^{''}}{A_0}\left(1 + \frac{2R_1}{|r_b|}\cos\phi\right) + \frac{R_2}{R_r}\left(1 + \frac{2R_1}{|r_b|}\frac{V_r}{V_o}\cos\phi\right) \tag{3.59}$$

and

$$q(\omega) = \frac{2\omega M^{'}}{A_0}\left(1 + \frac{2R_1}{|r_b|}\cos\phi\right) + \frac{4\omega^2 M^{''}}{A_0}\frac{R_1}{|r_b|}\sin\phi - \frac{2R_1}{|r_b|}\frac{R_2}{R_r}\frac{V_r}{V_o}\sin\phi \tag{3.60}$$

The magnitude of the gain is

$$\left|\frac{v_o}{v_t}\right| = \frac{R_2}{R_t}\frac{\left[\left(1 + \frac{2R_1}{|r_b|}\cos\phi\right)^2 + \left(\frac{2R_1}{|r_b|}\sin\phi\right)^2\right]^{\frac{1}{2}}}{\left[p(\omega)^2 + q(\omega)^2\right]^{\frac{1}{2}}} \tag{3.61}$$

The phase angle of the gain is

$$\varphi = -\tan^{-1}\frac{\sin\phi}{\cos\phi + \dfrac{|r_b|}{2R_1}} - \tan^{-1}\frac{q(\omega)}{p(\omega)} \tag{3.62}$$

The sensitivity to heat transfer coefficient is

$$\left|\frac{v_o}{\tilde{h}}\right| = \frac{2R_1\left|\dfrac{G_h(s)}{r_b(s)}\right|}{\left[p(\omega)^2 + q(\omega)^2\right]^{\frac{1}{2}}} = \frac{2R_1\left|\dfrac{G_h(s)}{r_b(s)}\right|\left|\dfrac{v_o}{v_t}\right|\dfrac{R_t}{R_2}}{\left[\left(1+\dfrac{2R_1}{|r_b|}\cos\phi\right)^2 + \left(\dfrac{2R_1}{|r_b|}\sin\phi\right)^2\right]^{\frac{1}{2}}} \tag{3.63}$$

The sensitivity to ambient temperature fluctuation is

$$\left|\frac{v_o}{\overline{T}_a}\right| = \frac{2R_1\left|\dfrac{G_h(s)}{r_b(s)}\right|}{\left[p(\omega)^2 + q(\omega)^2\right]^{\frac{1}{2}}} = \frac{2R_1\left|\dfrac{G_T(s)}{r_b(s)}\right|\left|\dfrac{v_o}{v_t}\right|\dfrac{R_t}{R_2}}{\left[\left(1+\dfrac{2R_1}{|r_b|}\cos\phi\right)^2 + \left(\dfrac{2R_1}{|r_b|}\sin\phi\right)^2\right]^{\frac{1}{2}}} \tag{3.64}$$

If the op-amp has only one pole, i.e., $M'' = 0$,

$$p(\omega) = 1 + \frac{4\omega M'}{A_0}\frac{R_1}{|r_b|}\sin\phi + \frac{R_2}{R_r}\left(1 + \frac{2R_1}{|r_b|}\frac{V_r}{V_o}\cos\phi\right) \tag{3.65}$$

$$q(\omega) = \frac{2\omega M'}{A_0}\left(1 + \frac{2R_1}{|r_b|}\cos\phi\right) - \frac{2R_1}{|r_b|}\frac{R_2}{R_r}\frac{V_r}{V_o}\sin\phi \tag{3.66}$$

In most of our experimental studies on the sensor frequency responses in CT mode, OP-27 has been used as the feedback amplifier. It has a single pole and is unity gain stable. Its gain-bandwidth product is about 7 MHz. In the measurement of the gain, the amplitude of the sine wave testing signal v_t is adjusted to ensure that the output signal satisfies the small signal criteria, i.e., $v_o << V_o$. R_2 and R_3 are both 5 kΩ, R_t and R_r are 1 MΩ, a_r = 0.1, V_r = 4.2 V for all types of sensors when the circuit is in critical damping

state. The measured magnitude and phase responses of the gain to frequency are then shown in Figure 3.23 and Figure 3.24. The solid lines are the theoretical curves calculated from Eqs. (3.61) and (3.62) with $|r_b|$ and ϕ being the fitted data obtained in Section 3.4.3.

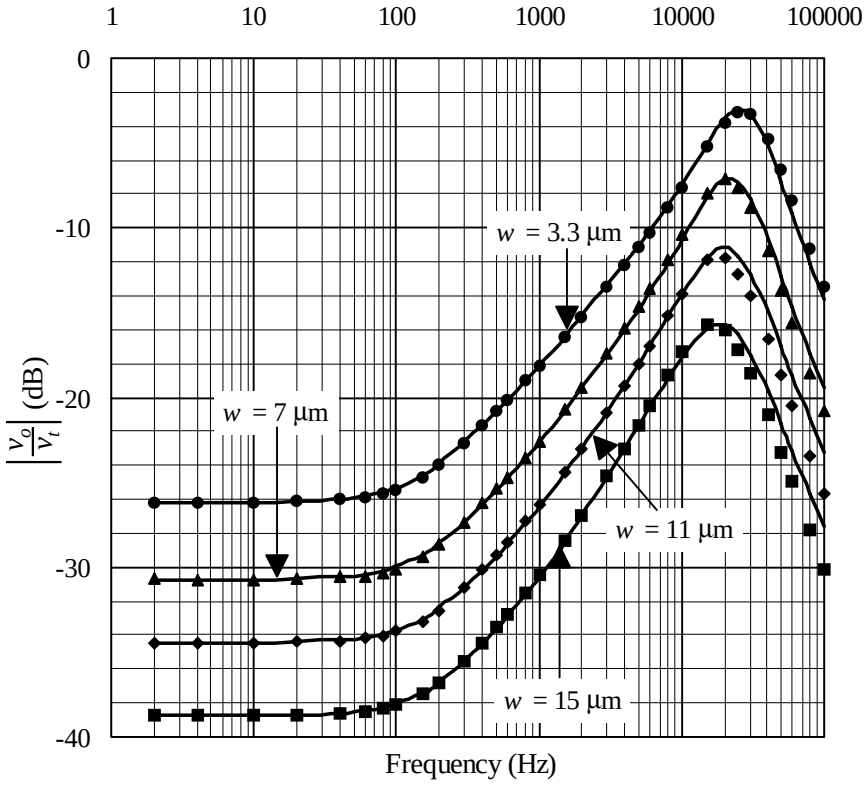

Figure 3.23 Magnitude responses of the gain of the CT circuit at a_R = 0.1.

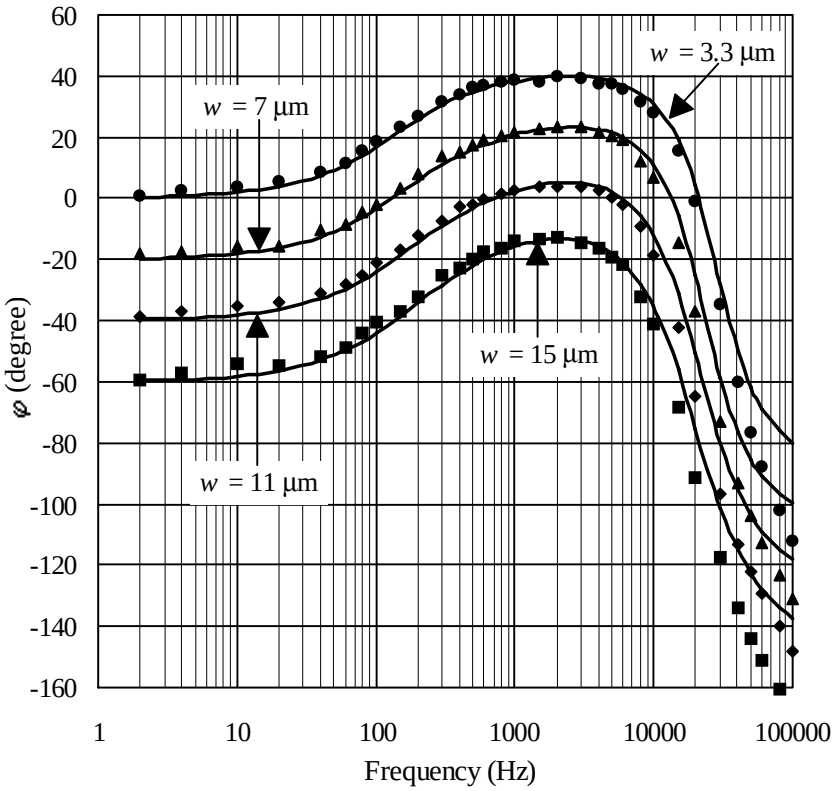

Figure 3.24 Phase responses of the gain of the CT circuit.

The magnitude of the gain is almost inversely proportional to $|r_b(i\omega)|$ before reaching the peak. The frequency at the peak is the critical frequency of the system to electronic signals. It has also been assumed to be the cut-off frequency of the system to flow signals. According to Eq. (3.63), this assumption is correct for conventional hot-wire and some hot-film sensors where $r_b(i\omega)$and $G_h(i\omega)$ have the same frequency responses. However, in the previous section, they have been found to have significantly different frequency responses for our sensors. We can therefore expect a somewhat non-flat magnitude response of our CT sensor systems to flow signals even below the critical frequency (Figure 3.25 and Figure 3.26) and certain compensation in data processing such as using FFT is necessary for some applications.

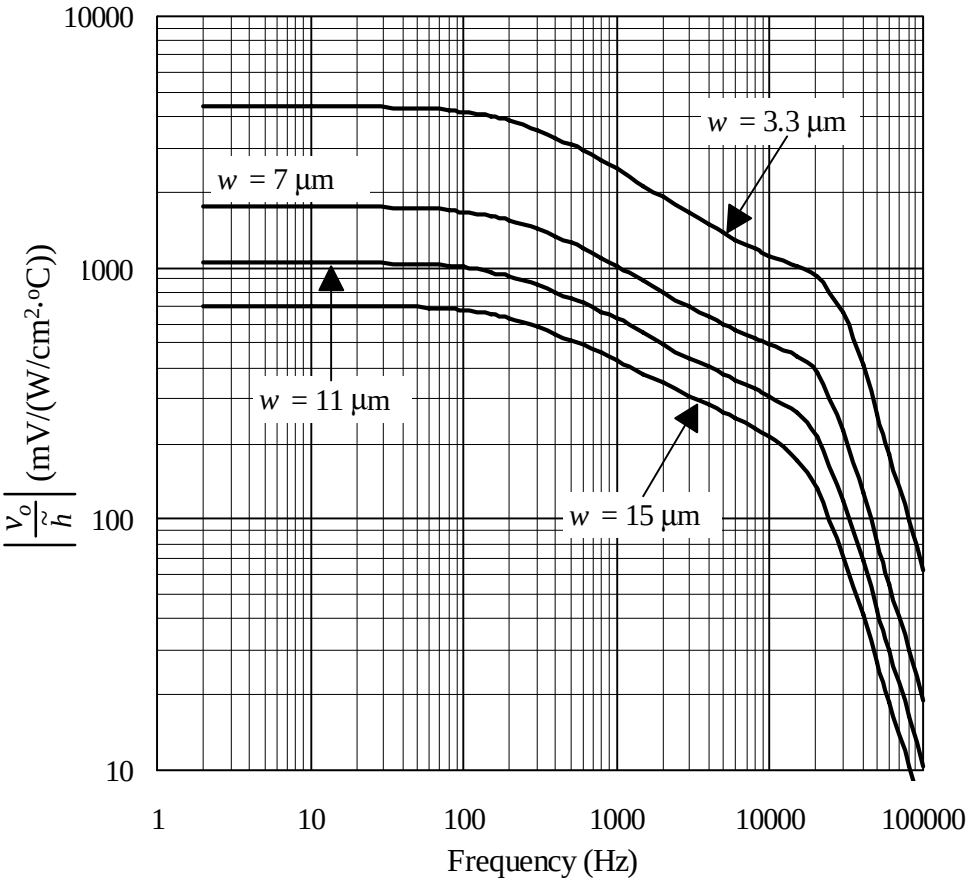

Figure 3.25 Calculated frequency response of the sensitivity to heat transfer coefficient in CT mode.

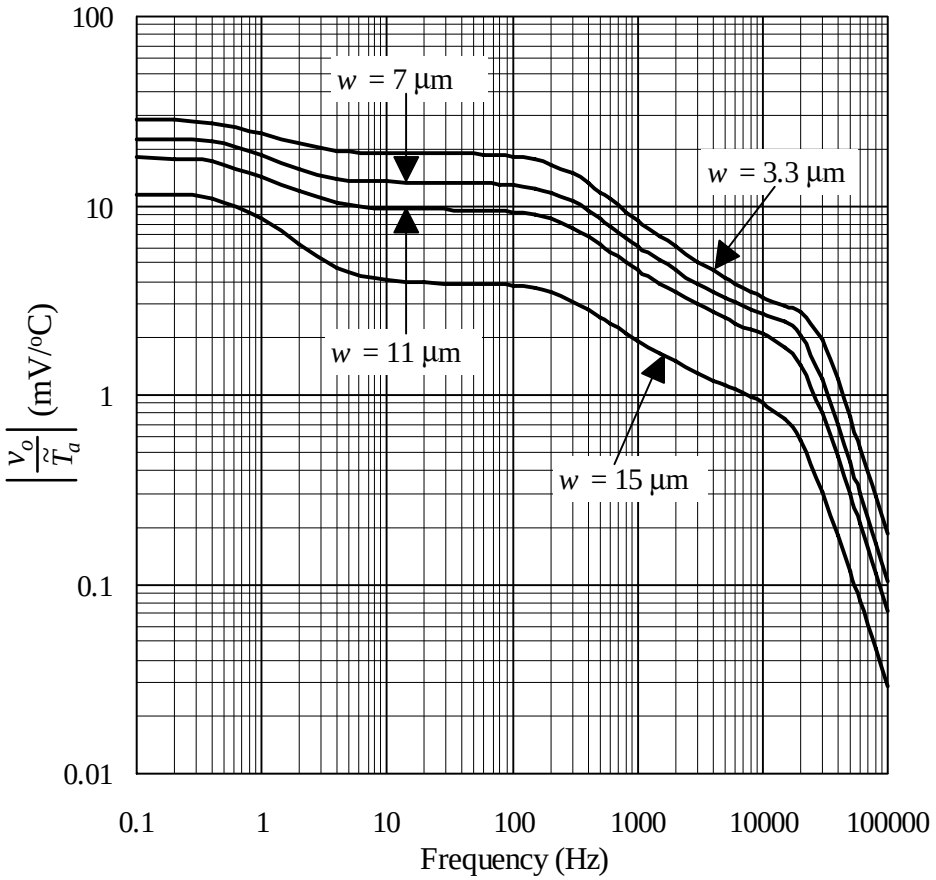

Figure 3.26 Calculated frequency response of the temperature sensitivity in CT mode.

The critical frequency of the CT circuit can be boosted by using improved circuits and op-amps with higher gain-bandwidth products. We will not discuss it here because it is beyond the scope of our research. The non-flat frequency response of the sensitivity to heat transfer below the critical frequency can be improved by optimizing the design of the sensor, including the increase on the horizontal dimensions (especially the width) of the polysilicon resistor while to equalize the frequency responses of $r_b(i\omega)$ and $G_h(i\omega)$. The underlying principle of the improvement, of course, is the reduction of the conduction heat loss from the polysilicon resistor to the nitride diaphragm through the sides and through the ends.

3.5 Comparison with Conventional Hot-Film Sensors

Table 3.3 Comparison of conventional and micromachined shear stress sensors.

Parameters	Conventional	Micromachined
Sensor dimension	mm size	250×250 μm2
Resistance	10 - 100 Ω	400 - 2.5 kΩ
Sensitivity (mV/Pa)	< 10	> 50
Frequency bandwidth (CC)	< 10 Hz	> 100 Hz
Power consumption (mW)	> 40	5

3.6 Other Structures

In addition to the vacuum-isolated shear stress sensor (type I) described above, we have also fabricated and studied other possible structures that can be used as shear stress sensors [23]. Their cross-sections and SEM pictures are shown in Figure 3.27. Type II has a similar structure to type I except that the polysilicon wire is lifted a few microns above the diaphragm, thus achieving better thermal isolation. Type III is a conventional polysilicon bridge sitting on the solid substrate [24,25]. Type IV is basically a micromachined hot wire which is very close to the wall. All these wires are a few microns (in a range from 1 μm to 5 μm) above the substrate surface so they are well in viscous sublayer, i.e., the linear velocity distribution region and the heat transfer is still a function of wall shear stress [11]. In our study, all four types of structures were fabricated on a single chip to ensure identical thermal and electrical properties of the sensing elements.

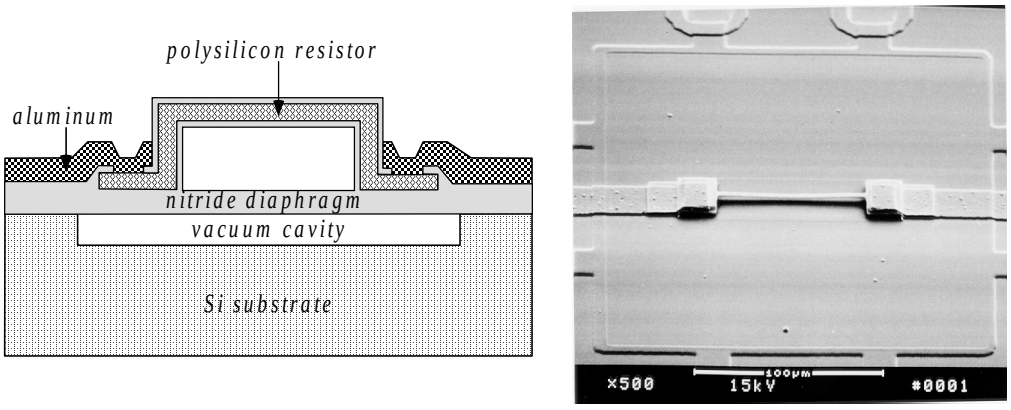

(a) Type II: bridge over diaphragm.

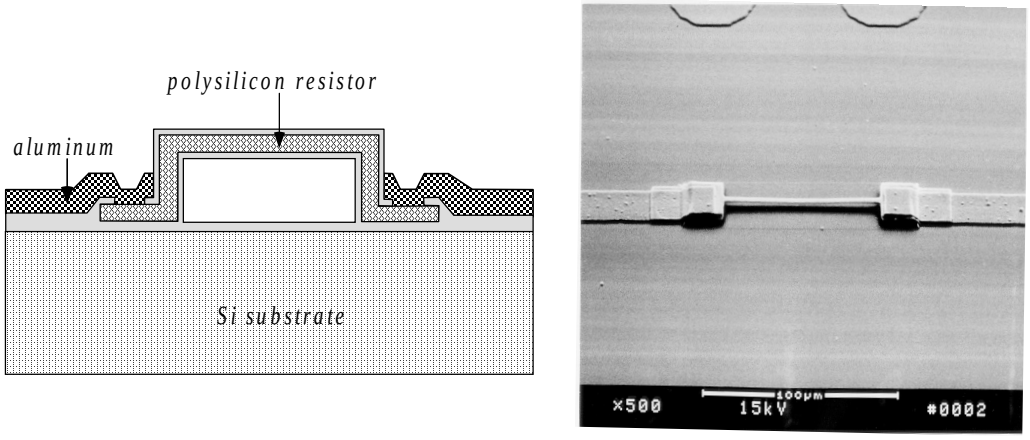

(b) Type III: bridge over substrate.

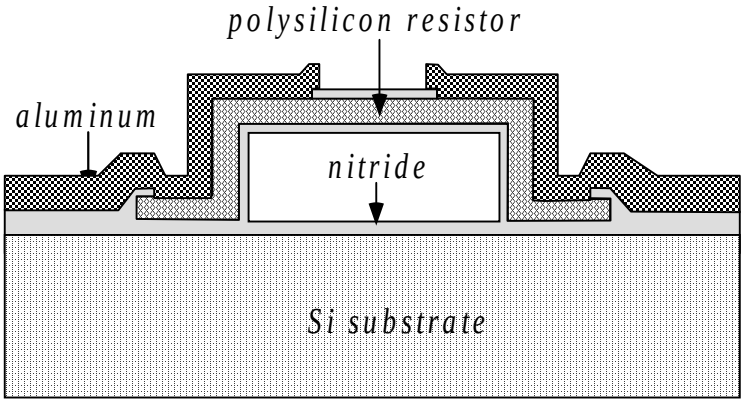

(c) Type IV: hot wire. The SEM picture is not available.

Figure 3.27 Structures and SEM pictures of other types of micromachined shear stress sensors.

3.6.1 Frequency Responses

The frequency responses of the sensors operating in constant current (CC) mode are compared in Figure 3.28. Note that for type I, the frequency response is determined mainly by the diaphragm properties such as thickness and thermal conductivity. For type III, since the ends of the wire are directly connected to the substrate which behaves as a perfect heat sink, the frequency response is solely determined by the polysilicon wire. For type II and IV, the diaphragm and the support shanks to which the polysilicon wires are connected can heat up through thermal conduction; therefore, each type has two corner frequencies, one corresponding to the diaphragm or the support shanks and the other (3 - 4 kHz) to the polysilicon wire. The effect of the second corner frequency can be greatly reduced if we increase the wire length or put aluminum over the support shanks.

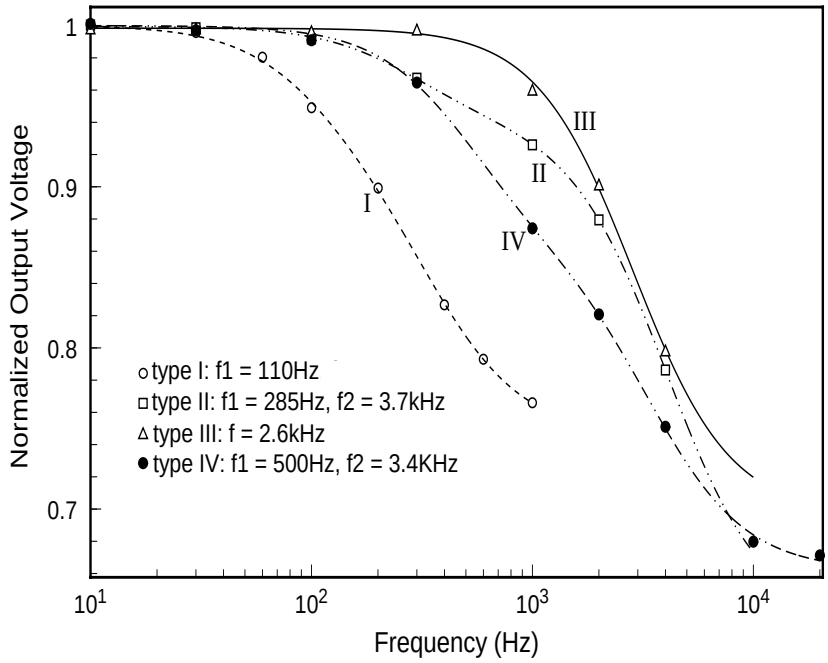

Figure 3.28 Frequency responses of four types of sensors in CC mode.

3.6.2 Thermal Resistance

To study the heat transfer characteristics, we have measured the electrical power needed to heat up the wire to a certain temperature in atmosphere and in vacuum (~ 30 mTorr) for all of the structures. The results are shown in Figure 3.29. The reciprocals of the slopes of these curves represent the thermal resistance R_{th}. Type I has the smallest thermal resistance because the nitride diaphragm is also significantly heated. The thermal resistances in atmosphere and in vacuum are not very different, meaning that most of the heat is conducted to the substrate though the diaphragm in atmosphere. Types II - IV have nearly the same thermal resistance. Their slight differences reflect different end losses. The thermal resistance in vacuum is many times smaller than that in atmosphere, meaning that in atmosphere, the end heat loss is a very small part of the total heat. The combination of the heat convection to air and heat conduction to the substrate through the air dominates the heat transfer process.

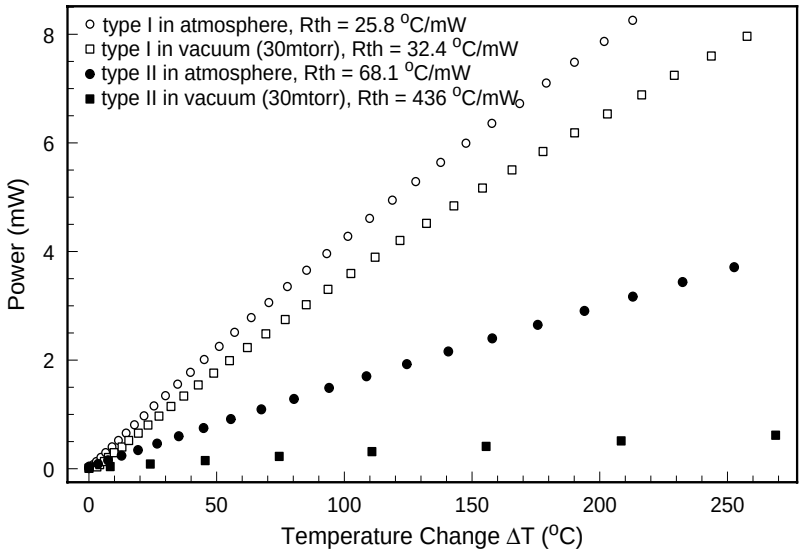

(a) Types I and II.

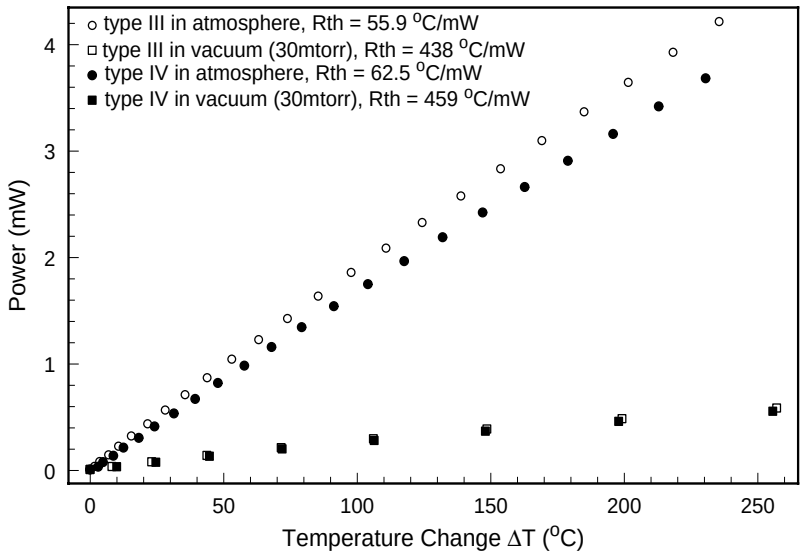

(b) Types III and IV.

Figure 3.29 Thermal resistance in atmosphere and in vacuum. The polysilicon resistors are all 120 μm long and 3 μm wide. The distance between the resistors and the substrates for types II, III and IV are 4 μm.

Another interesting test is to measure the power as a function of the height of the wire above the substrate in atmosphere for type IV sensors. This gives the information about the heat conduction loss to substrate through the air. As shown in Figure 3.30, this loss can not be neglected for *h* less than 10 μm.

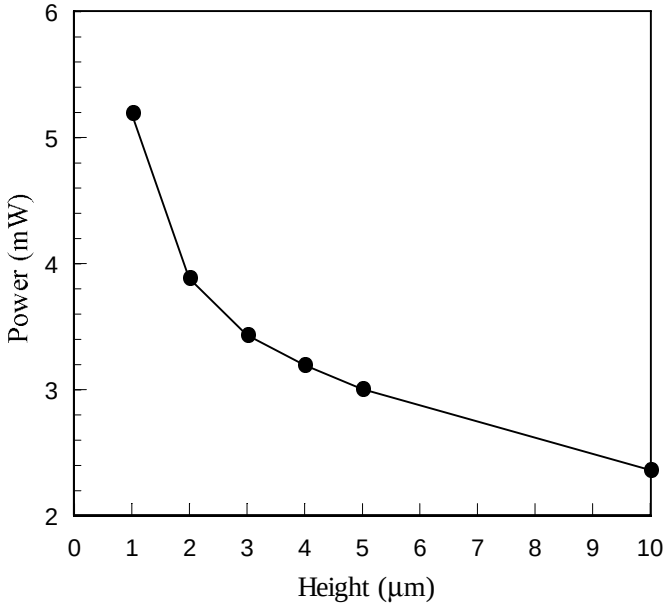

Figure 3.30 The power needed to heat up type IV sensors with different bridge height to 200^{o}C.

3.6.3 Steady-State Responses

Figure 3.31 shows the calibration results in wind-tunnel. The output changes are proportional to the one third power of shear stress, which agrees with the heat transfer theory. Types I and II are the most sensitive ones and have approximately the same relative sensitivity, despite the big difference in thermal resistance. The reason might be that when the wire is not far above the diaphragm for type II, the interaction (heat transfer) between them is almost independent of the environment change and they can be considered as a single element, just as type I sensor. Also, both type I and type II have smallest conduction loss to the substrate and are certainly more sensitive than the other two types that have significant conduction loss to the substrate through the air gaps and/or through the ends (mainly for type III). Increasing the gap height reduces the conduction loss to the substrate and improves the sensitivity for types III and IV, but then it may interfere with the flow and make the sensor more physically vulnerable.

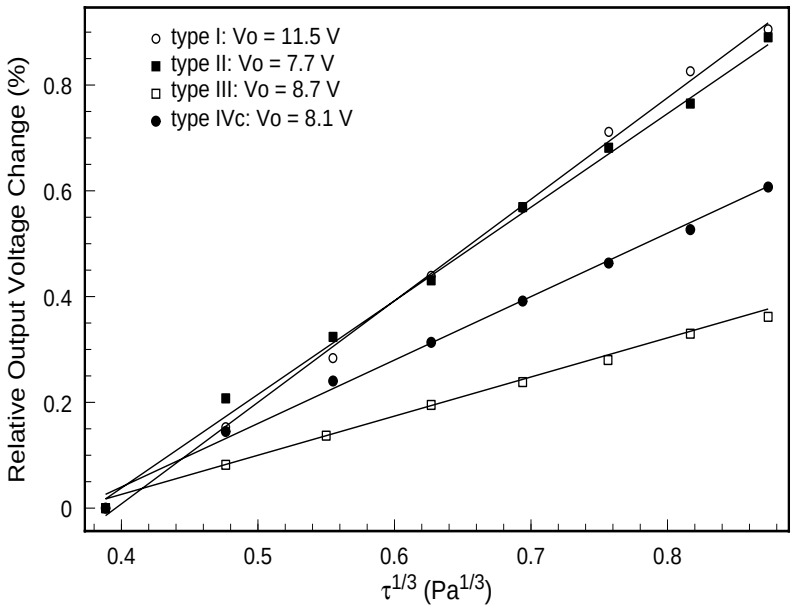

Figure 3.31 Wind tunnel calibration results for all types of micromachined shear stress sensor structures in CT mode (a_R = 0.1).

3.7 Summary

A novel MEMS thermal shear stress sensor featuring a unique vacuum cavity has been developed. The vacuum cavity dramatically improves the thermal isolation of the polysilicon sensing element from the substrate. The steady-state and transient heat transfer models of the sensor has been established and successfully used to analyze the steady-state wind-tunnel calibration results, temperature sensitivities and frequency responses. The theoretical analysis also provides the guidance for the optimization of the sensor design. Finally, other potential sensor structures are explored and their sensitivity and frequency responses are compared with the vacuum-cavity isolated sensor.

Bibliography

[1] T. J. Hanratty and J. A. Campbell, "Measurement of Wall Shear Stress," *Fluid Mechanics Measurements*, R. J. Goodstein, ed., Hemisphere Publishing, pp. 559-615, 1983.

[2] J. H. Haritonidis, "The Measurement of Wall Shear Stress," *Advances in Fluid Mechanics Measurements*, Mgad-el Hak, ed., Springer-Verlag, New York, pp. 229-261, 1989.

[3] T. E. Stanton, D. Marshall, and C. W. Bryant, "On the Condition of the Boundary of a Fluid in Turbulent Motion," *Proc. R. Soc. London A*, Vol. 97, pp. 413-434, 1920.

[4] J. H. Preston, "The Determination of Turbulent Skin Friction by Means of Pitot Tubes," *J. Roy. Aero. Scoc.*, Vol. 58, pp. 109-121, 1953.

[5] M. A. Schmidt, R. T. Howe, S. D. Senturia, and J. H. Haritonidis, "Design and Calibration of a Microfabricated Floating-Element Shear-Stress Sensor," *IEEE Tans. Electron Dev.*, Vol. ED-35, pp. 750-757, 1988.

[6] T. Pan, D. Hyman, M. Mehregany, E. Reshotko, and B. Willis, "Characterization of Microfabricated Shear Stress Sensors," *Tech. Digest 8th Int. Conf. On Solid-State Sensors and Actuators (Transducer'95)*, Stockholm, Sweden, pp.1995.

[7] A. Fage and V. M. Falkner, "On the Relation between Heat Transfer and Surface Friction for the Laminar Flow," *Aero Res. Counc. London*, R&M No.1408, 1931.

[8] H. Ludwieg, "Instrument for Measuring the Wall Shearing Stress of Turbulent Boundary Layers," NACA TM-1284, 1950.

[9] H. W. Liepmann and G. T. Skinner, "Shearing-Stress Measurements by Use of a Heated Element," NACA TN-3269, 1954.

[10] J. E. Mitchell and T. J. Hanratty, "A Study of Turbulence at a Wall Using an Electrochemical Wall-Stress Meter," *J. Fluid Mech.*, Vol. 26, pp. 199-221, 1966.

[11] B. J. Bellhouse and D. L. Schultz, “Determination of Mean and Dynamic Skin Friction, Separation and Transition in Low-Speed Flow with a Thin-Film Heated Element,” *J. Fluid Mech.*, Vol. 24, pp. 379-400, 1966.

[12] M. J. Moen and S. P. Schneider, “The Effect of Sensor Size on the Performance of Flush-Mounted Hot-Film Sensors,” *J. Fluid Eng.*, Vol. 116, pp. 273-277, 1994.

[13] W. J. McCroskey and E. J. Durbin, “Flow Angle and Shear Stress Measurements Using Heated Films and Wires,” *J. Basic Eng.*, Vol. 94, pp. 46-52, 1972.

[14] D. C. Reda, “Rise-Time Response of Nickel-Foil-on-Kapton-Substrate Hot-Film, Shear-Stress Sensors,” AIAA Paper 91-0169, 1991.

[15] B. J. Bellhouse and D. L. Schultz, “The Determination of Fluctuating Velocity in Air with a Heated Thin Film Gauges,” *J. Fluid Mech.*, Vol. 29, pp. 289-295, 1967.

[16] B. J. Bellhouse and D. L. Schultz, “The Measurement of Fluctuating Skin Friction in Air with a Heated Thin-Film Gauges,” *J. Fluid Mech.*, Vol. 32, pp. 675-680, 1968.

[17] B. W. van Oudheusden and Huising, “Integrated Flow Friction Sensor,” *Sensors & Actuators A*, Vol. 15(2), pp. 135-144, 1988.

[18] E. Kalvesten, C. Vieider, L. Lofdahl, and G. Stemme, “An Integrated Pressure-Flow Sensor for Correlation Measurements in Turbulent Gas Flows,” *Sensors & Actuators A*, Vol. 52, pp. 51-58, 1996.

[19] G. L. Brown, “Theory and Application of Heated Films for Skin Friction Measurement,” *Proc. Heat Transfer and Fluid Mechanics Institute*, Stanford University Press, pp. 361-381, 1967.

[20] P. D. Weidman and F. K. Browand, “Analysis of a Simple Circuit for Constant Temperature Anemometry,” *J. Physics E: Sci. Instrum.*, Vol. 8, pp. 553-560, 1975.

[21] I. Kidron, “Measurement of the Transfer Function of Hot-Wire and Hot-Film Turbulence Transducers,” *IEEE Tans. Instrum. & Meas.*, Vol. IM-15 (3), pp. 76-81, 1966.

[22] S. C. Ling, “Heat Transfer Characteristics of Hot-Film Sensing Element Used in Flow Measurement,” *J. Basic Engr.*, Vol. 82, pp. 629-634, 1960.

[23] F. Jiang, Y. C. Tai, J. B. Huang, and C. H. Ho, “Polysilicon Structures for Shear Stress Sensors,” *Digest IEEE TENCON’95*, Hong Kong, pp. 12-15, 1995.

[24] Y. C. Tai, R. S. Muller, “Lightly-Doped Polysilicon Bridge as Flow Meter,” *Sensors and Actuators*, Vol. 15 (1), pp. 63-75, 1988.

[25] C. H. Mastrangelo, *Thermal Applications of Microbridges*, Ph. D. Thesis, University of California at Berkeley, 1990.

Chapter 4

Shear Stress Imager

The active control of turbulent flows has long been a dream of fluid mechanicists because of its potential impact on the aerospace industry [1,2,3]. Up to now, however, little has been done mainly because of the unavailability of miniature devices whose sizes are comparable to the feature sizes in high-Reynolds-number turbulent flows. Among these previously unavailable devices are the distributed shear stress sensor arrays. They are responsible for the real-time collection of wall shear stress information, which is processed by detection circuits to identify the turbulence structure. This chapter describes the development of such a shear stress imager using the shear stress sensor developed in Chapter 3 and its shear stress profiling capability in turbulent boundary layers.

4.1 Turbulent Boundary Layer and Streamwise Vortices

The basic understanding of turbulent boundary layer and vortex structure is important for the proper design of the shear stress imager. Here we only discuss the wall-bound channel flow which will be used for shear stress imaging.

4.1.1 Channel Flow

Figure 4.1 shows the successive stages of development of the boundary layer of an incompressible viscous fluid in a channel, assuming the no-slip boundary condition, i.e., the fluid on the wall is not moving. At the entrance of the channel, uniform flow at free-stream velocity exists. As the fluid moves down the channel, shear friction between the fluid and the wall, and between adjacent fluid layers, retards the motion, causing the boundary layer to grow until it is fully developed. From this point on, the velocity profile

remains unchanged. The length required for the flow to become fully developed is known as the *entrance length* x_e. Note that the free stream velocity U_∞ is replaced by the centerline velocity U_c in calculating the Reynolds number in fully developed channel flow.

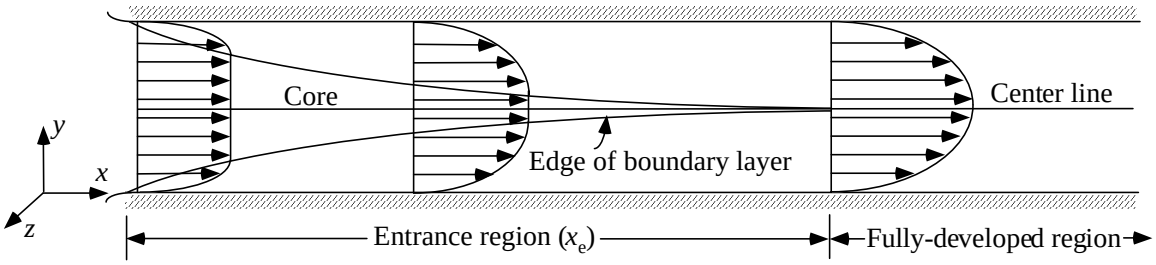

Figure 4.1 Boundary layer development in channel flow.

4.1.2 Wind Tunnel

The wind tunnel that is used in most of the turbulent boundary layer studies is in the UCLA Fluid Mechanics Laboratory. It is 4.87 m long, 60 cm wide and 2.54 cm high. Note that a wind tunnel with this high aspect ratio cross section supplies a two-dimensional channel flow. The walls of the channel are constructed of 2.5 cm thick Plexiglass and supported by a steel frame. An axial blower powered by a DC source supplies the air flow in the channel. At the highest blower speed, the centerline velocity in the channel is about 25 m/s. Hot-wire velocity measurements at 8 m/s indicate that the channel consists of a laminar entrance flow region which gradually transforms into a fully-developed turbulent flow in the downstream 2/3 portion of the channel. All calibration and testing of shear stress sensors and shear stress imaging is carried out in this region of the channel.

In the fully developed region, the mean shear stress is uniform everywhere on the wall because the velocity profiles remains unchanged. A simple force balance on a rectangular control volume of length L, width W and height H gives

$$\tau_w = \frac{H}{2L}\Delta p \tag{4.1}$$

if $W >> H$, i.e., for a 2-D channel. In the above equation, τ and Δp are the mean shear stress and mean pressure difference. Therefore, the mean shear stress in the 2-D fully developed channel flow can be determined through the measurement of the pressure gradient.

On the other hand, wall shear stress can be expressed as

$$\tau_w = \rho_f u_\tau^2 \tag{4.2}$$

where u_τ is called the *friction velocity* and ρ_f is the density of the fluid. For air at room temperature, ρ_f is 1.21 kg/m^3. According to [4], the friction velocity is related to the centerline stream velocity and Reynolds number by

$$\frac{u_\tau}{U_c} = 0.119\mathbf{Re}^{-0.089} \tag{4.3}$$

Here the half height of the wind tunnel $H/2$, i.e., the boundary thickness, is taken as the characteristic length of the Reynolds number. Therefore, the shear stress can also be calculated from the measurement of the free stream velocity from

$$\tau_w = 0.00427U_c^{1.822} \tag{4.4}$$

It is found that the wall shear stresses determined by the above two methods in our wind tunnel give almost identical results.

4.1.3 Streamwise Vortices and Sub-Layer Structures

It has been revealed that turbulent flow has dual features, deterministic and random. The deterministic part of the turbulence is responsible for most of the mass and momentum transfers for both free and wall-bounded flows [5,6,7]. For wall-bounded channel flow, the quasi-deterministic structures have been numerically and experimentally identified in the fully developed turbulent region to be a pair of counter-rotating streamwise vortices (Figure 4.2). These vortices, which appear randomly in both space and time, bring high velocity fluids down to the wall and create a streak of high

shear stress in the region between the vortices. These streaky structures can be detected through the measurement of near wall velocity [8] or wall shear stress distribution.

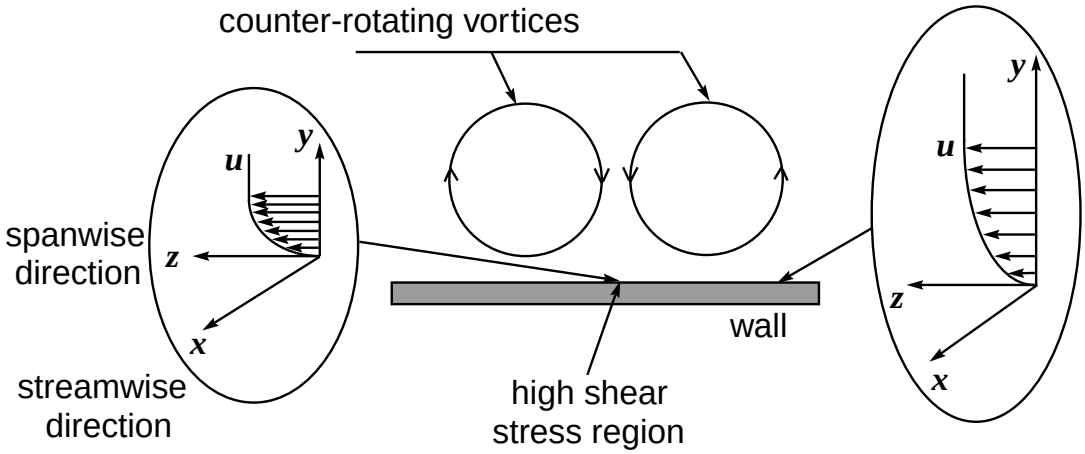

Figure 4.2 Counter-rotating vortex pair.

The statistical sizes of the streaky structures have been reported by a number of authors [9,10,11,12,13,14,15]. Most observed quantities exhibit significant variations. Nevertheless, these are helpful to the design of our shear stress imaging chip. According to Cantwell [5], the thickness of the viscous sub-layer is $7\nu/u_\tau$; the length of sub-layer structure in the streamwise direction λ_x varies from $100\nu/u_\tau$ to $2000\nu/u_\tau$ with $1000\nu/u_\tau$ as the best value; the vertical half scale of the sub-layer structure λ_y varies from $10\nu/u_\tau$ to 25 ν/u_τ with $15\nu/u_\tau$ as the best value; the spanwise scale of the sub-layer structure λ_z is generally agreed to be $100\nu/u_\tau$. Here ν/u_τ is the viscous length. It decreases as the Reynolds number increases. For the centerline air flow velocity ranging from 8 m/s to 25 m/s in our wind tunnel, the friction velocity u_τ is from 0.394 m/s to 1.111 m/s and the Reynolds number is from 6790 to 21200. The best estimation of the scales of the sub-layer streaky structures corresponding to above flow velocity range is

Streamwise scale $\lambda_x = 1000\ \nu/u_\tau$ = 1.35 cm - 3.80 cm

Spanwise scale $\lambda_z = 100\ \nu/u_\tau$ = 1.35 mm - 3.80 mm

Vertical half scale $\lambda_y = 15\ \nu/u_\tau$ = 0.20 mm - 0.57 mm

These numbers tell us that in order to capture the sub-layer structures (minimum of three sensors per structure) in our wind tunnel, the sensor dimension and spacing of the shear stress imager has to be less than half a millimeter. Traditional flush-mounted hot-film sensors obviously do not meet this dimensional requirement. This is probably one of the reasons why there has been no report on sub-layer structure detection at high Reynolds number.

4.2 Shear Stress Imager

Based on the understanding of the sub-layer streaky structures in turbulent flows, we have developed the 2.85 cm $\times$ 1.0 cm shear stress imaging chip shown in Figure 4.3 using the 3 μm wide and 150 μm long micro shear stress sensor described in Chapter 3. The chip is specifically designed for the study in turbulent flow with Reynolds number around 10^4. There are two identical rows of sensors 5 mm apart and normal to the streamwise direction. This streamwise pitch is chosen such that at least three data points can be taken from a streak in the streamwise direction. Each row has 25 sensors with 300 μm pitch, which is already the minimum for this type of sensor. It should give at least three data points from a streak in the spanwise direction and be able to catch more than one streak. Between the two major rows of sensors, there are two 5-sensor rows and one 25-sensor row for the detection of streak details in spanwise direction. The 1 cm spacing between the sensors and the bonding pads on the left and right edges of the chip is necessary to avoid the upstream bonding wires from interfering with the downstream sensors.

The fabrication process of the shear stress imager is basically the same as that of a single sensor but it needs two more masks for the final metallization step. The yield of sensors on a imaging chip is important even for laboratory testing purpose. Thanks to the well-designed process, more than 95% of the sensors on each chip can be used for measurement.

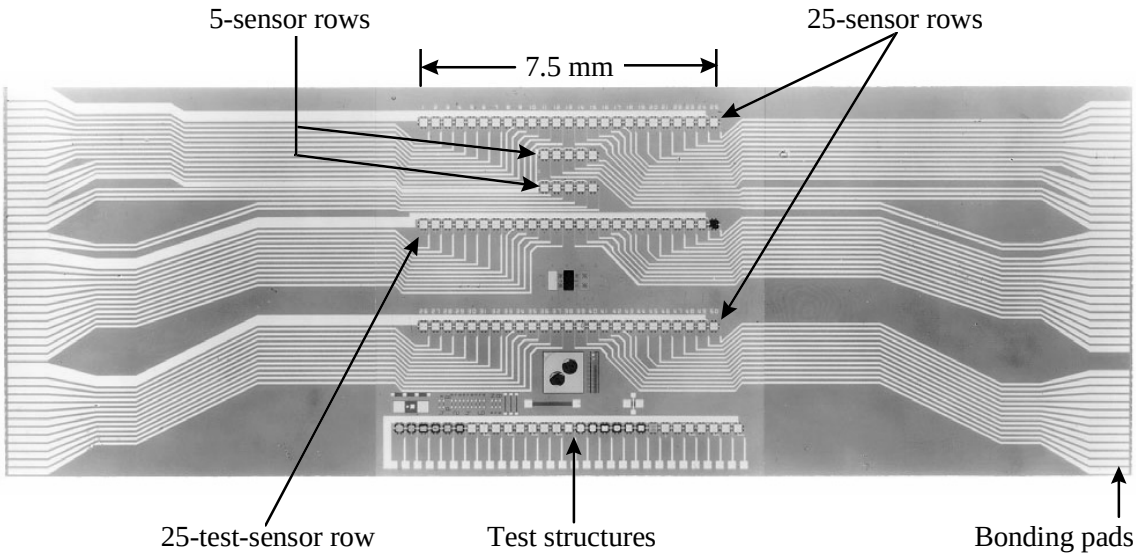

Figure 4.3 The micromachined shear stress imager (2.85×1 cm^2) with over 100 sensors.

4.3 Packaging, Biasing and Calibration

The package for the imaging chip is a fine-line PC board with a chip-size recess in the center so that the imaging chip can be flush-mounted. The chip and the PC board are electrically connected by wire bonding (Figure 4.4). The electrical leads are soldered on the backside of the PC board. The PC board is then flush-mounted on a specially-made plug which fits into the wall of the wind-tunnel (Figure 4.5), with the sensor row perpendicular to the flow direction.

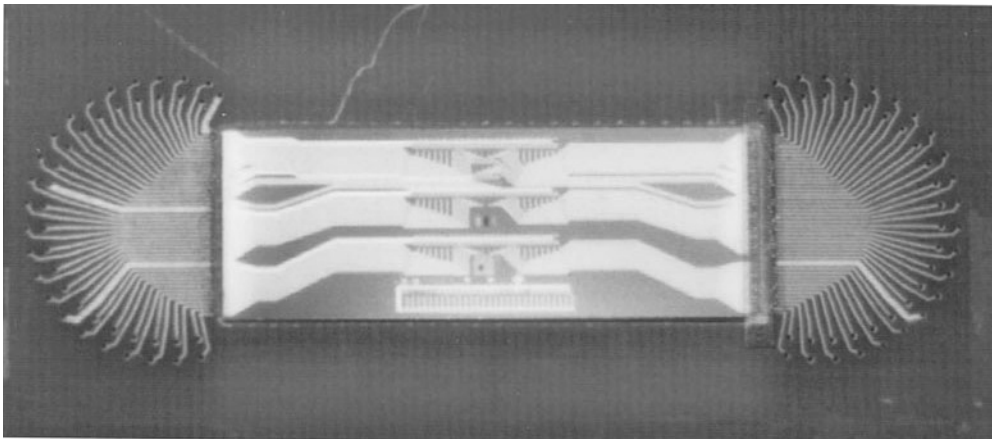

Figure 4.4 Photograph of the packaged shear stress imager.

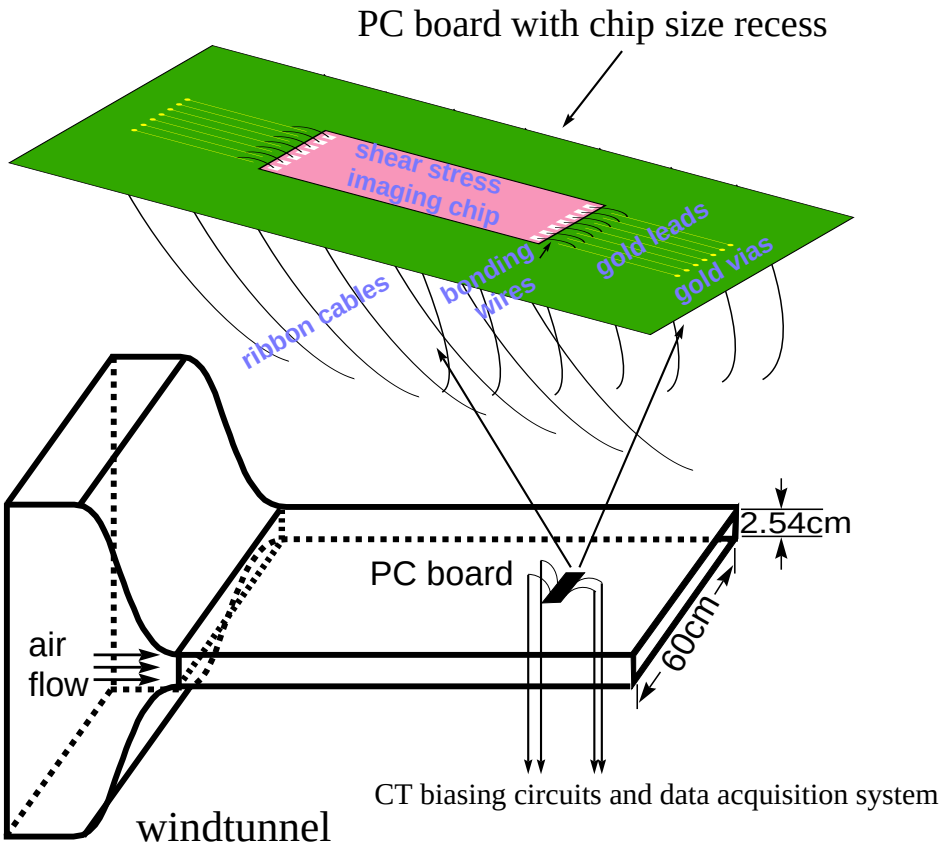

Figure 4.5 Imaging chip package and wind tunnel setup.

In our experiments, the sensors are biased in constant temperature (CT) mode. Although it is more complicated than the constant current mode, it can achieve much higher frequency bandwidth which is crucial in turbulence measurement. Therefore, arrays of CT circuits and gain stages have been made on PC boards using op-amps and other discrete components (Figure 4.6). The dc offset of the outputs can be adjusted individually, but the gain is fixed to be 10. A computer-controlled data acquisition system is used to measure all the outputs simultaneously.

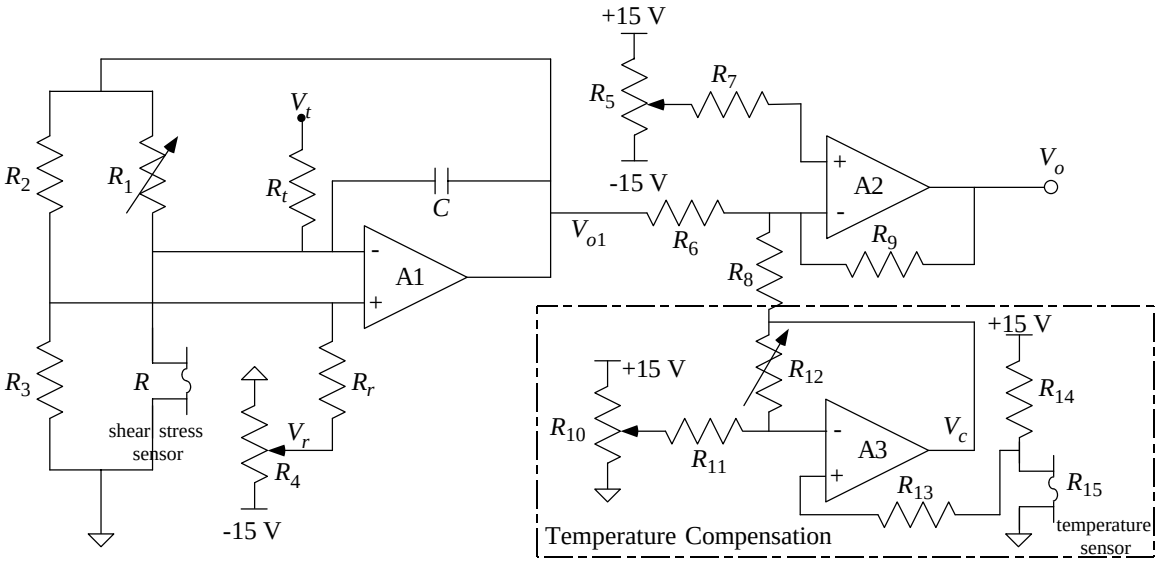

A1, A2, A3: OP-27

$R_3 = R_3/a_R$ (a_R: over-heat ratio)

C = 100-500 pF

R_1: 3.6 kΩ multi-turn precision potentiometer

$R_2 = R_3 = R_6 = R_7 = R_8 = R_{11} = R_{13}$ = 5.0 kΩ

R_4, R_5 and R_{10}: 10 kΩ multi-turn pots

$R_r = R_t$ = 1 MΩ

R_9 = 50 kΩ

R_{12}: 470 kΩ multi-turn precision pot

R_{14} = 150 kΩ

R_{15}: temperature sensor - shear stress sensor operated at very low power

Temperature conpensation stage can be shared by all channels

Figure 4.6 Constant temperature biasing circuit, gain stage and temperature compensation stage.

Before the sensors are used to measure the shear stress distribution, their dc outputs are calibrated against known wall shear stress levels which are calculated from the centerline velocity by using Eq. (4.4). Figure 4.7 shows the calibration results for 10

sensors in a row. Although each sensor has different offset, the trend of all curves are almost the same. Polynomial fitting is performed on each curve to extract the fitting parameters for later use in real data processing.

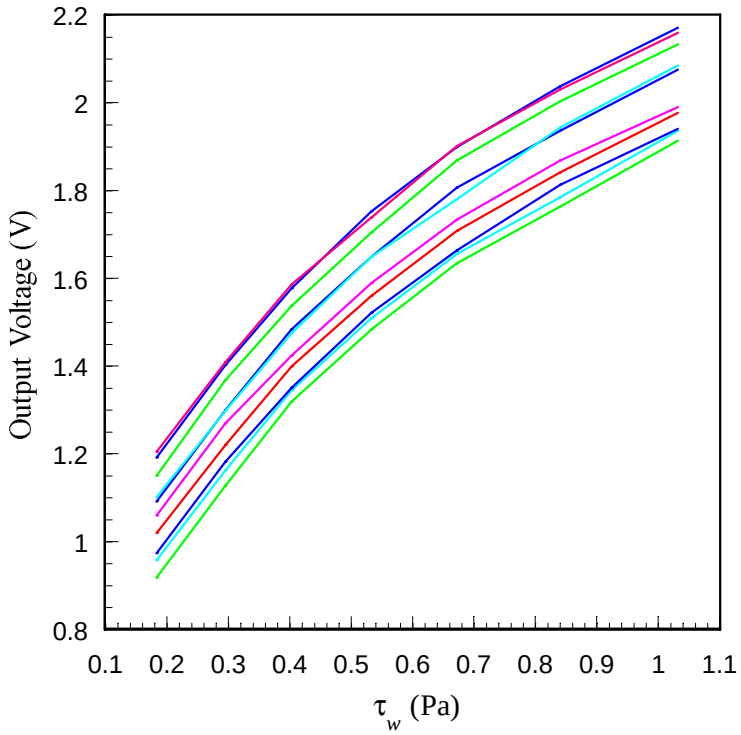

Figure 4.7 Calibration curves of 10 sensors in a row.

The temperature of the air flow in the wind tunnel is not a constant because of the warm-up of the blower and the fluctuating ambient temperature. The maximum flow temperature change can be as high as 5^{o}C. On the other hand, the shear stress sensors have temperature sensitivities in the order of -(150-200) mV/^{o}C (after gain of 10) around room temperature. Therefore, serious drifts on the DC outputs of the shear stress sensors during the real time data acquisition is expected and could cause the measured data to be useless. There are two ways to compensate for the drifts. The first method is to use the simple temperature compensation circuit in Figure 4.6. Here the temperature sensor can be a shear stress sensor operated at very low power such that the self-heating is negligible. Note that the output of the compensation circuit V_c can be shared by all the

channels so only one such circuit is needed for all the sensors in use. The results in Figure 4.8 show that an order of magnitude of improvement of the thermal stability has been achieved. The other way to compensate the drifts is to do post processing on the data, using the flow temperature history data recorded by a temperature sensor. Both methods requires calibration of the temperature sensitivity for each sensor. Obviously, the first method is suitable for real time measurement and control, but the second one is simpler.

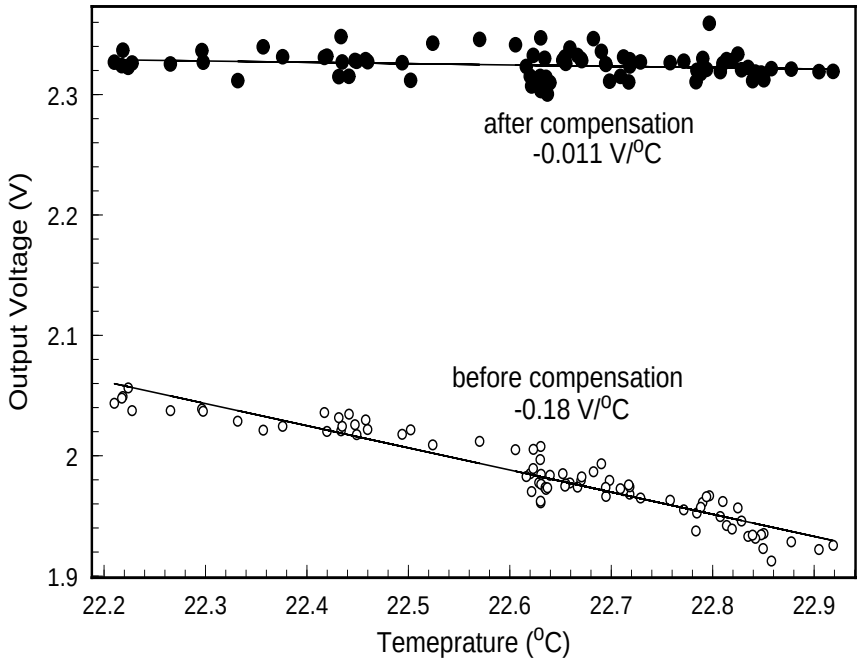

Figure 4.8 Typical temperature sensitivities before and after temperature compensation of a shear stress sensor.

4.4 Shear Stress Imaging

For real-time shear stress imaging, the output voltage is sampled at a rate higher than 10kHz and converted to a shear stress signal based on the calibration performed previously. In order to establish the credibility of the imaging chip, the turbulence statistics calculated from the shear stress fluctuations recorded by a single shear stress sensor are compared to previously established results. Figure 4.9 shows the comparison in

terms of the normalized RMS level, the skewness factor, and the flatness factor. It is obvious that the present results agree very well with previous studies in all three areas [16,17,18]. In addition, the present statistics appear to be independent of the Reynolds number which is predicted by turbulence theory.

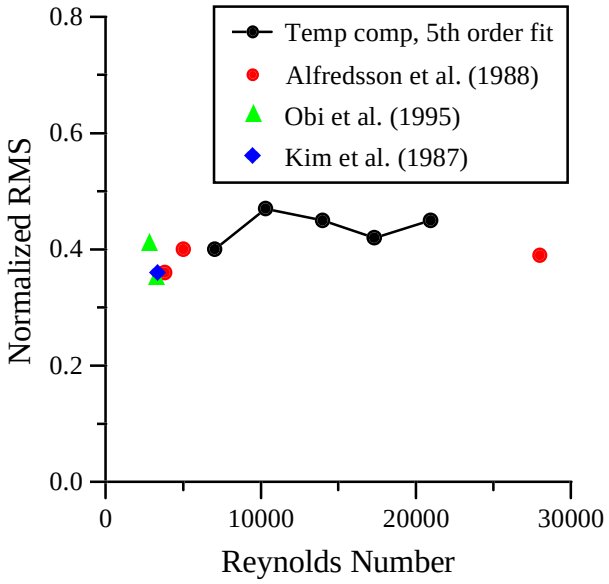

(a) RMS values of the shear stress fluctuations normalized to the corresponding DC shear stress.

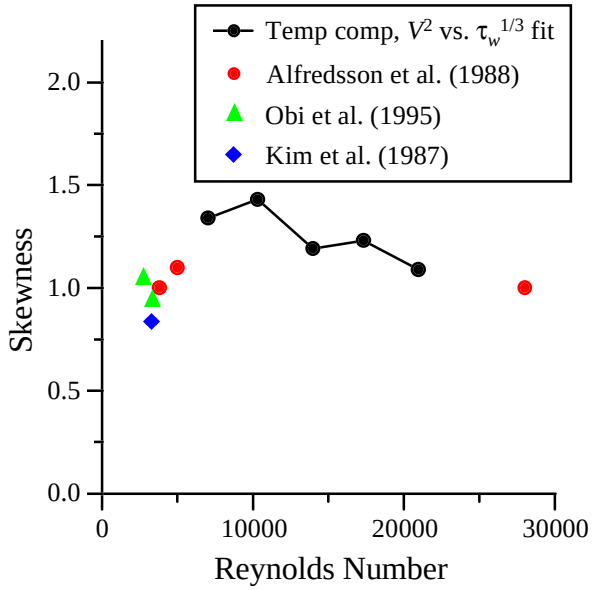

(b) Skewness factor.

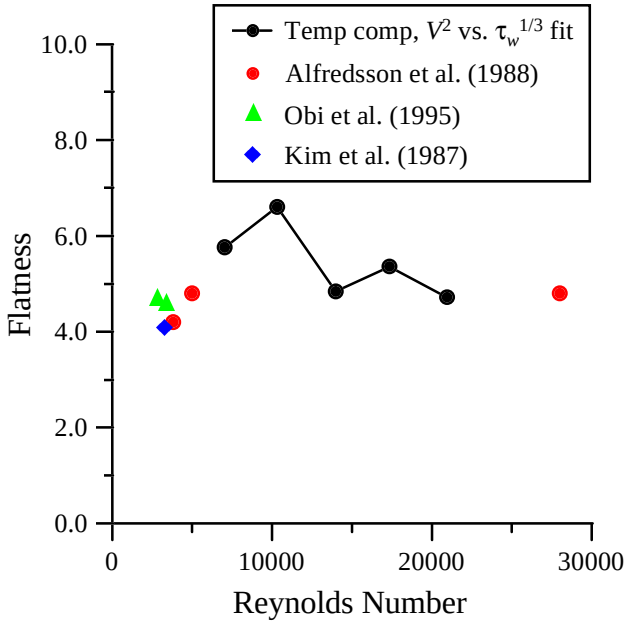

(c) Flatness factor.

Figure 4.9 Turbulence statistics based on the shear stress fluctuations recorded by the micro shear stress sensors on the imaging chip.

Another validation method is to compare the instantaneous output from a shear stress on the flush-mounted imaging chip with that from a hot-wire anemometer directly above the shear stress sensor because near wall hot wire measurement has been considered as one of the standard techniques in the studies of sub-layer structures, although it can only give instantaneous velocity signal at one location. The vertical distance from the hot wire to the wall must be smaller than the vertical half scale ($\lambda_y = 15\ \nu/u_\tau$) of a sub-layer streaky structure so that both the shear stress sensor and the hot wire are within the same structure. The hot wire we used for this test is a 1 mm long platinum wire 2.5 μm in diameter operated in CT mode with a bandwidth of 30 kHz. Its vertical distance from the shear stress sensor is about 0.4 mm, which is equivalent to 12.5 ν/u_τ at a centerline velocity of 10 m/s. The measurement results at this velocity are shown in Figure 4.10. It can be seen that the two output traces are very similar, indicating that the flush-mounted shear stress sensor is truly measuring the sub-layer structure as the widely used

conventional hot wires are. The output of the shear stress sensor gives a little more details because it is much shorter than the hot wire.

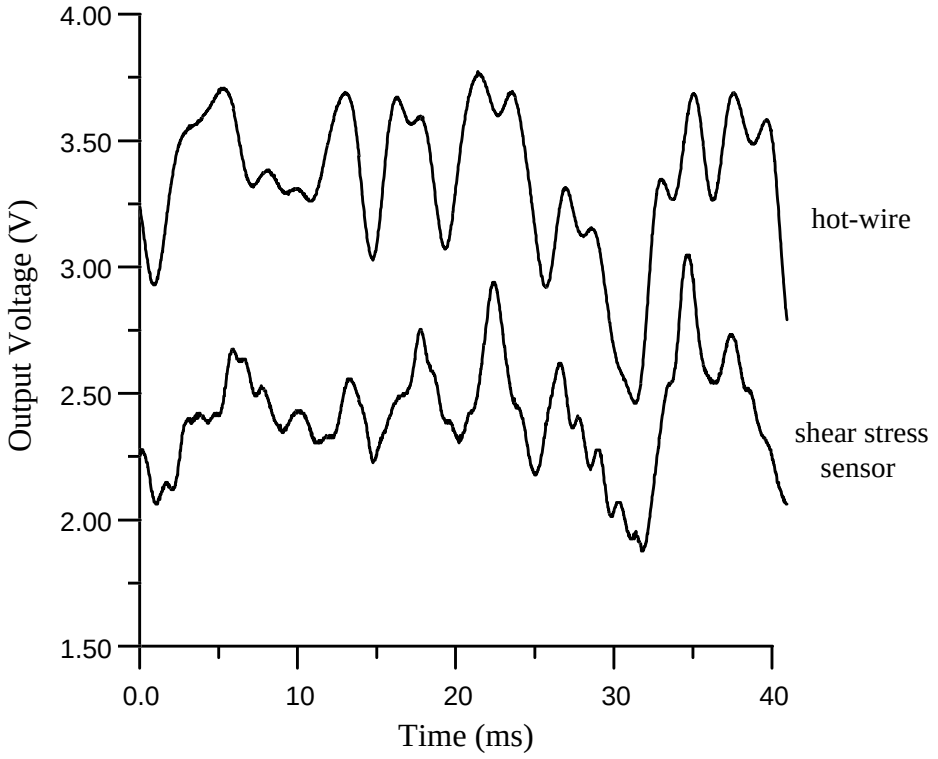

Figure 4.10 Comparison between the instantaneous outputs from a shear stress on the flush-mounted imaging chip and a 1 mm long hot-wire anemometer 0.4 mm above the shear stress sensor at a centerline velocity of 10 m/s.

The instantaneous turbulent shear stress distributions of the channel were recorded by using one of the sensor rows on the imaging chip. Figure 4.11 shows the contour plots of the time evolution of the shear stress distributions at two different centerline velocities. The red streaky structures in the plots represent regions of high shear stress on the wall of the channel where the sensor row is located. They are caused by the presence of near-wall streamwise vortices which bring high momentum fluid from the free stream to the wall. Due to the small-scale nature of these structures, previous experiments in turbulent boundary layers have only succeeded in qualitatively demonstrating their existence

without obtaining any quantitative information. This is the first time that these near-wall structures are quantitatively recorded.

In Figure 4.11, the time axis can be converted to the spatial scale in streamwise direction by multiplying it with the convection velocity U_{con} (~ (0.5-0.6)U_c) so the plots look like 2-D shear stress images. We call them *pseudo* 2-D shear stress distribution plots. They are so named because if the lifetime of the sub-layer structures passing the sensor row is longer than the data-taking time, these plots then represent the instantaneous shear stress distribution of these structures in the vicinity of the sensor row. The above assumption about the lifetime is known as Taylor's hypothesis in fluid mechanics and it holds in most cases.

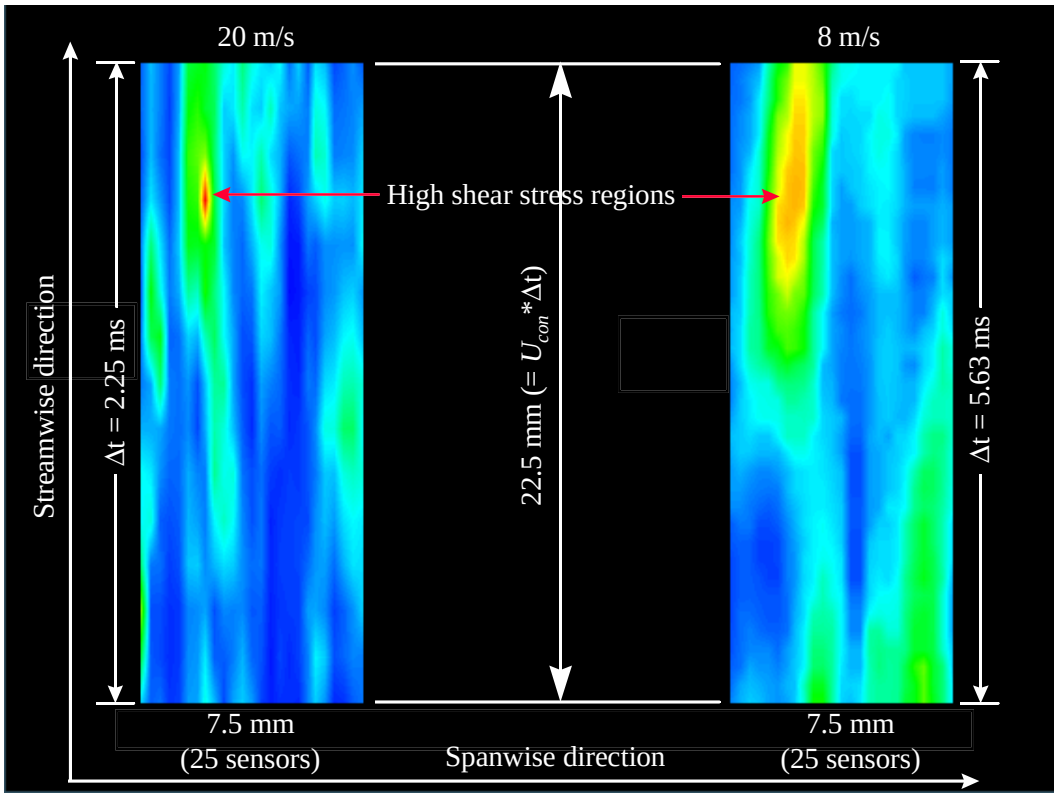

Figure 4.11 Contour plots of the pseudo 2-D shear stress distributions. Red area indicates high shear stress and blue area indicates low stress.

To confirm the validity of the above hypothesis, we have performed the real-time 2-D shear stress imaging for a period of time using the 5×4 sensor array located on the top-middle region of the imaging chip (Figure 4.3). The results are shown in Figure 4.12. On the right is a pseudo 2-D plot generated from the outputs of the 5 sensors on the first row at four different times (0 ms, 0.083 ms, 0.167 ms and 0.25 ms), while on the left is the real 2-D plot generated from the instantaneous outputs of the 5×4 sensor array recorded at the time of 0.25 ms. Note that the top and the bottom of the pseudo plot correspond to the measurements at 0 ms and 0.25 ms respectively. It can be clearly seen that these two plots are showing the same structure. The difference is on the peak shear stress level. We have found that the pseudo 2-D plots always show a lower peak level than the real 2-D plots.

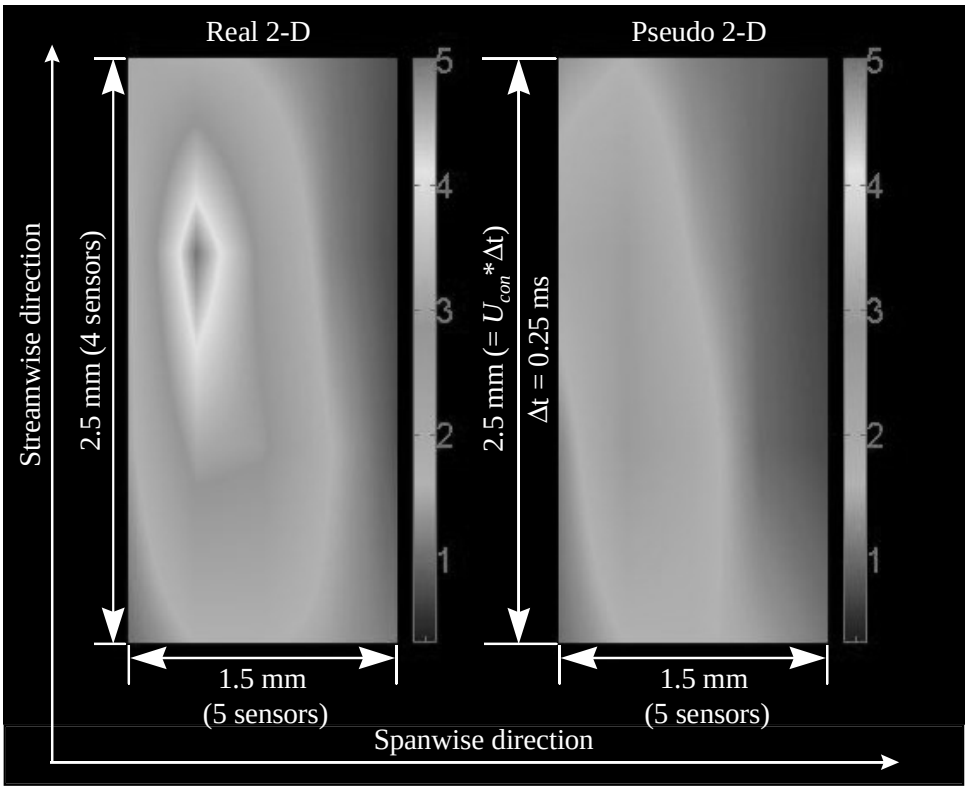

Figure 4.12 Comparison of the contour plots obtained by using 4 rows of sensors (real 2-D imaging) and by using only one row of sensors (pseudo 2-D imaging) at a centerline velocity of 20 m/s.

The contour plots in Figure 4.11 indicate that the scales of the streaks are different at different centerline velocities. The streaks in the high-speed (20 m/s) case appear to be thinner and more densely packed than those in the low-speed (8 m/s) case. Similar phenomena have also been observed in previous experiments. Based on real-time movies generated from the contour plots similar to the ones in Figure 4.11, the average streamwise length, the average spanwise scale, and the average spanwise spacing of the streaks at three different centerline velocities are estimated and shown in Figure 4.13. Once again, the present results agree well with previous studies. The average length of the present streaks falls within the upper and lower bounds of the established results. The average spanwise scale and spacing of the present streaks are either on or slightly higher than the upper bound.

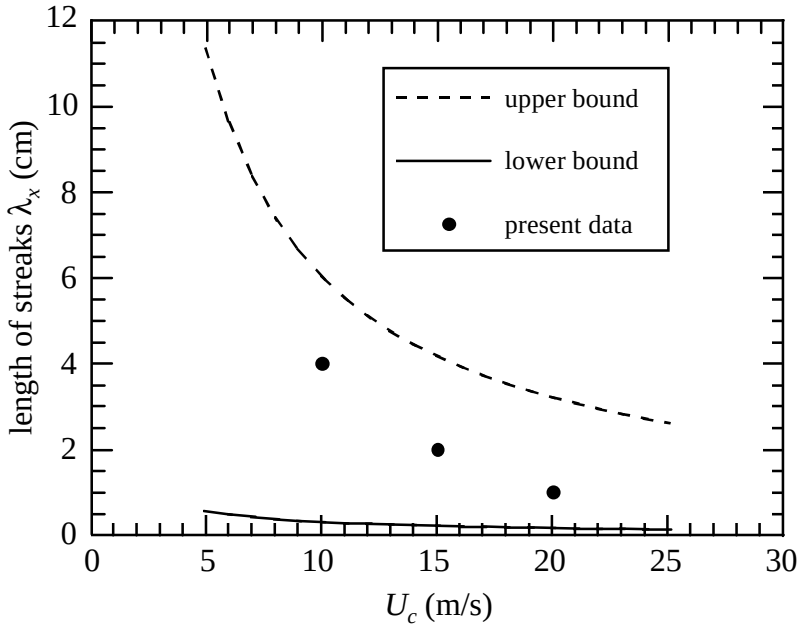

(a) The length of streaks.

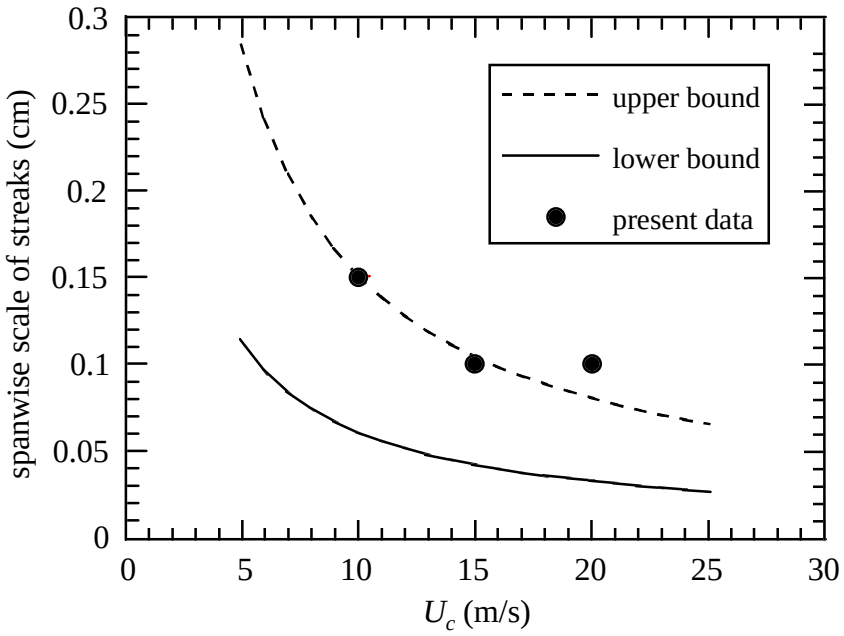

(b) The spanwise scale of streaks.

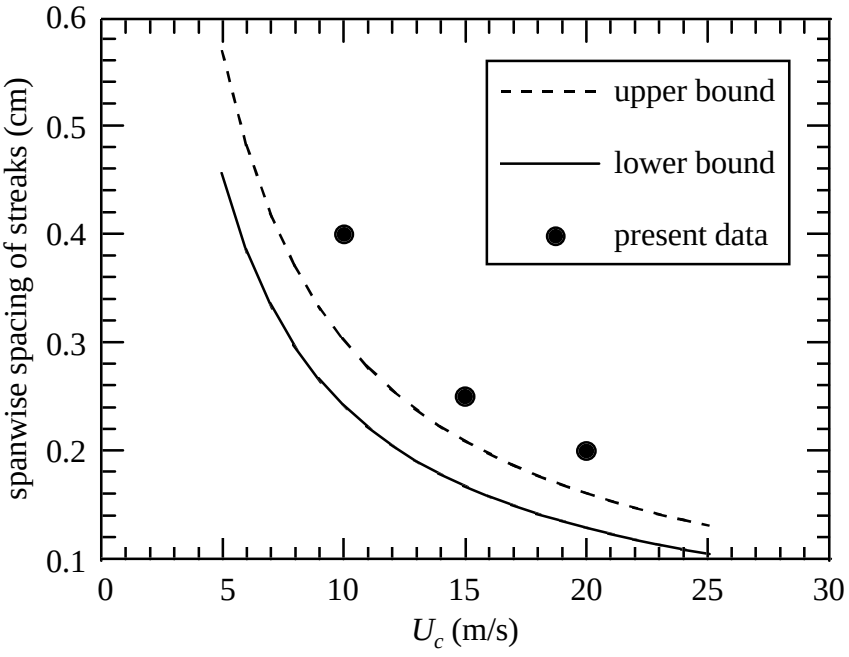

(c) The spanwise spacing of streaks.

Figure 4.13 Scales of the near-wall streaky structures at different Reynolds numbers.

4.5 Underwater Measurement

A shear stress sensor or hot-film sensor can be directly used in other electrically non-conductive fluid flows such as polymer. However, for underwater application, the leads or the entire sensor have to be coated with a layer of waterproof material for protection and electrical insulation purpose because water, especially sea water, is corrosive to metals and electrically conducting. The most commonly used coating material for conventional underwater hot-film sensors is thin (1-2 μm) quartz. It has been found that these quartz-coated hot-film sensors have serious drift problem during underwater measurement [19,20], even though they are operated at very low over-heat ratio to avoid bubble formation. The main reason is probe contamination in dirty water such as gradual build up of scale, algae, and minerals on the probe, causing a shift in the calibration. The other possibility might be that the surface of the conventional hot-film sensors before coating are rough and thin quartz coating can not cover the surface very well. Also, the sputtered quartz may not have good quality.

The coating materials for our MEMS shear stress sensors can be LPCVD silicon dioxide, PECVD silicon nitride or some organic materials such as Teflon and parylene. Among them, silicon nitride and Teflon are the best because nitride is resistant to sodium ion diffusion and Teflon is completely hydrophobic. Unfortunately, the first PECVD nitride deposition did not have good quality and spin-on Teflon did not have good adhesion to the sensor surface. As a result, only the LPCVD silicon dioxide has been successfully deposited on a shear stress imager wafer. The 2 μm thick oxide is patterned by photolithography and pad-etching to expose the bonding pads.

The packaging of the imaging chip for underwater measurement is shown in Figure 4.14. Epoxy is used to protect and insulate the bonding pads, bonding wires and soldering pads. As a result, the front surface is flat except the two bumps of epoxy on the edges of the imaging chip, which is acceptable for a demonstration and for drift testing only.

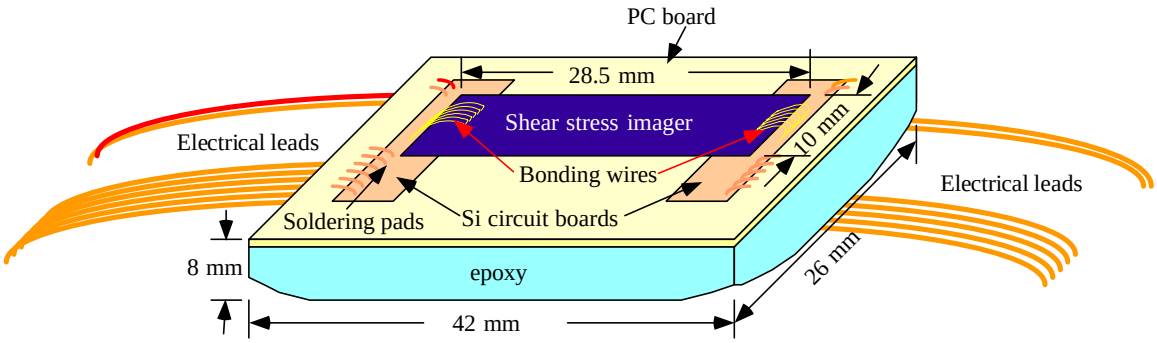

Figure 4.14 Schematic drawing of the packaging for underwater shear stress imager.

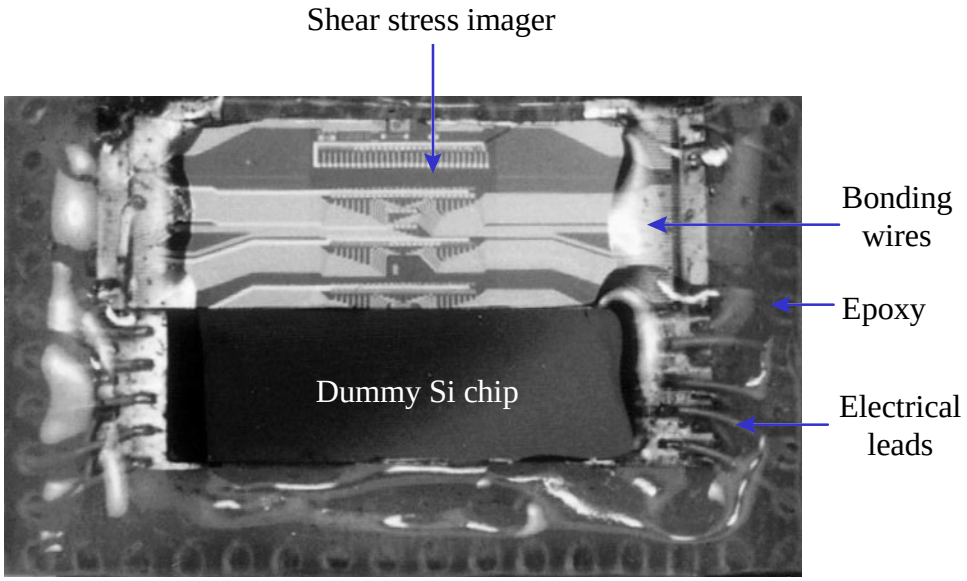

Figure 4.15 Photograph of the packaged shear stress imager for underwater measurement. Note that the imager is not diced in the same way as that in Figure 4.3 and the surface surrounding the imager and the dummy Si chip is not flat because of the hand-painted epoxy.

As usual, the sensors are biased in CT mode using the temperature compensated circuit in Figure 4.6. The over-heat ratio is only a few percent to avoid the bubble formation [21]. It has been found that the temporal drift of the sensor output voltage in water flow is very small (a few percent in 24 hours), probably because the sensor surface is smooth and the silicon dioxide deposited at 450^{o}C has much better quality than the sputtered quartz. Due to the lack of shear stress information in the water channel used for

the testing, we could only calibrate the sensor against the free-stream speed (Figure 4.16). One catch of the instantaneous output voltage fluctuation is shown in Figure 4.17.

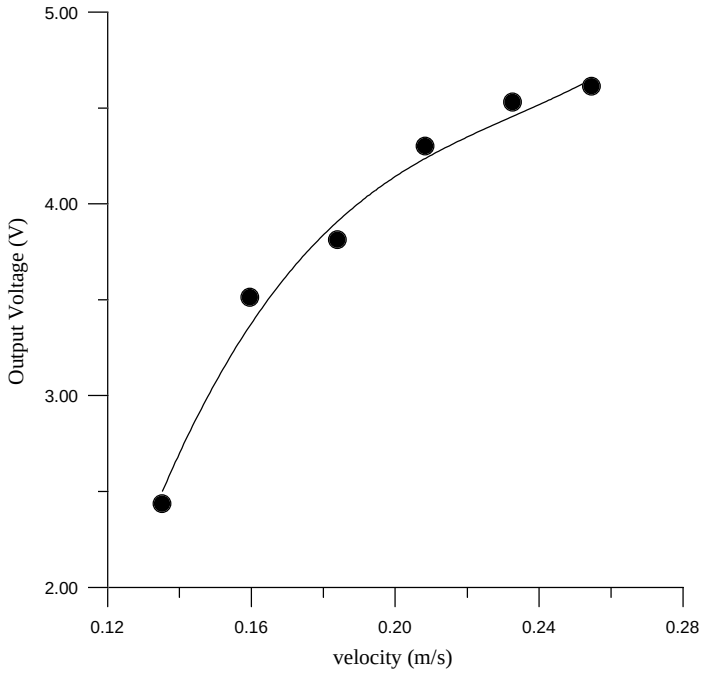

Figure 4.16 Calibration results of a shear stress sensor in a water channel.

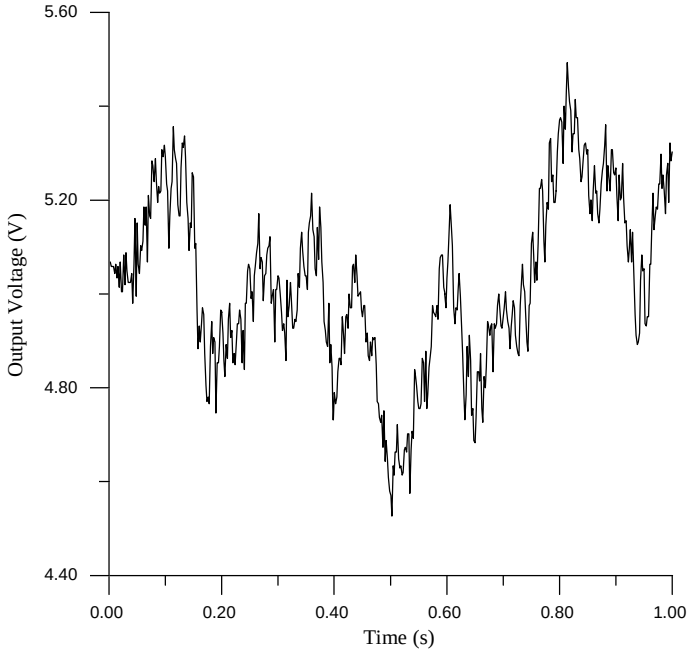

Figure 4.17 Instantaneous output voltage at a mean water flow speed of 25 cm/s.

The above preliminary study has only shown that the shear stress imager is potentially useful in underwater measurement. More work needs to be done, including better packaging and extensive steady-state and dynamic testing and analysis.

4.6 Summary

A new MEMS shear stress imager has been developed. More than 100 shear stress sensors are integrated on a 1×2.85 cm^2 Si chip. Real-time 2-D shear stress imaging in air flow has been experimentally realized for the first time by using this imaging chip. The comparison between the measured results in a fully developed 2-D channel flow and other researchers' experimental and theoretical estimation has validated the use of the imager. Its potential application includes the study and control of turbulent air flows and even water flows, if the chip is coated with a layer of waterproof material, such as silicon dioxide.

The current packaging schemes for the imaging chip in air and water flow are not ideal as it has bonding wires sticking out from the surface which more or less interfere with the flow. However, this problem can be solved by improving the design such as using buried contacts, backside contacts or the MEMS skin technology that will be described in Chapter 6.

Bibliography

[1] P. R. Bandyopadhyay, “Development of a Microfabricated Surface for Turbulence Diagnostics and Control,” *ASME Application of Microfabrication to Fluid Mechanics*, Chicago, pp. 67-74, 1994.

[2] D. M. Bushnell, “Turbulent Drag Reduction for External flows,” AIAA Paper 83-0227, 1983.

[3] P. Moin, J. Kim, and H. Choi, “On the Active Control of Wall-Bounded Turbulent Flows,” AIAA Paper 89-0960, 1989.

[4] A. K. M. F. Hussain and W. C. Reynolds, “The Mechanics of a Perturbation Wave in Turbulent Shear Flow,” AFOSR Scientific Report 70-1655TR, 1970.

[5] J. Cantwell, “Organized Motion in Turbulent Flow,” *Ann. Rev. of Fluid Mech.*, Vol. 13, pp. 475-515, 1981.

[6] C. M. Ho and P. Huerre, “Perturbed Free Shear Layers,” *Ann. Rev. Fluid Mech.*, Vol. 16, pp. 365-424, 1984.

[7] S. K. Robinson, “Coherent Motion in the Turbulent Boundary Layer,” *Ann. Rev. Fluid Mech.*, Vol. 23, pp. 601-639, 1991.

[8] J. C. Wyngaard, “Measurement of Small-Scale Turbulence Structure with Hot Wires,” *J. Phys. E: Sci. Instr.*, Vol. 1, pp. 1105-1108, 1968.

[9] R. F. Blackwelder, H. Eckelmann, “Streamwise Vortices Associated with the Bursting Phenomenon,” *J. Fluid Mech.*, Vol. 94, pp. 577-594, 1979.

[10] A. K. Praturi, R. S. Brodkey, “A Stereoscopic Visual Study of Coherent Structures in Turbulent Shear Flow,” *J. Fluid Mech.*, Vol. 89, pp. 251-272, 1978.

[11] S. J. Kline, W. C. Reynolds, F. A. Schraub, and P. W. Runstadler, “The Structure of Turbulent Boundary Layers,” *J. Fluid Mech.*, Vol. 30, pp. 741-773, 1967.

[12] H. P. Bakewell and J. L. Lumley, “Viscous Sublayer and Adjacent Region in Turbulent Pipe Flow,” *Phys. Fluids*, Vol. 10, pp. 1880-1889, 1967.

[13] L. S. G. Kovasznay, V. Kibens, and R. S. Blackwelder, "Large Scale Motion of Intermittent Region of a Turbulent Boundary Layer," *J. Fluid Mech.*, Vol. 41, pp. 283-325, 1970.

[14] H. T. Kim, S. J. Kline, and W. C. Reynolds, "The Production of the Wall Region in Turbulent Flow," *J. Fluid Mech.*, Vol. 50, pp. 133-160, 1971.

[15] T. J. Hanratty, L. G. Chorn, and D. T. Hatziavramidis, "Turbulent Fluctuations in the Viscous Wall Region of Newtonian and Drag Reducing Fluids," *Phys. Fluids*, Vol. 20 (10), pp. 112-119, 1977.

[16] P. H. Ferredoxin, A. V. Johansson, J. H. Haritonidis and H. Eckelman, "The Fluctuating Wall-Shear Stress and the Velocity Field in the Viscous Sublayer," *Phys. Fluids*, Vol. 31, pp.1026-1033, 1988.

[17] S. Obi, K. Inoue, T. Furukawa, and S. Masuda, "Experimental Study on the Statistics of Wall Shear Stress in Turbulent Channel Flows," *Tenth symposium on turbulent shear flows*, The Pennsylvania State University, Vol. 1, pp. 5-19 - 5-24, 1995.

[18] J. Kim, P. Moin and R. Moser, "Turbulence Statistics in Fully Developed Channel Flow at Low Reynolds Number," *J. Fluid Mech.*, Vol. 177, pp. 133-166, 1987.

[19] F. J. Resch, "Hot-Film Turbulence Measurements in Water Flows," *J. Hydr. Div. ASCE*, Vol. 96, No. HY3, pp. 787-800, 1970.

[20] K. A. Warschauer, J. B. A. Vijge, and G. A. Boschloo, "Some Experiences and Considerations on Measuring Turbulence in Water with Hot Films," *Appl. Sci. Res.*, Vol. 29, pp. 81-98, 1974.

[21] C. G. Rasmussen, "The Air Bubble Problem in Water Flow Hot-Film Anemometry," *DISA Info.*, No. 5, pp. 21-26, 1967.

Chapter 5

M^3 System for Viscous Drag Reduction

In aerospace engineering, drag reduction is one of the most challenging problems of aircraft. Drag limits the maximum speed, the maximum range of flight and the operational cost. For example, reduction of the drag by a few percent can amount to billions of dollars of annual savings world wide on commercial aircraft fuel cost. There are three types of drags - pressure or form drag, drag due to lift and skin-friction or viscous drag. The pressure drag involves the viscous influence upon the ideal or inviscid-flow pressure field. It is generally small in the attached flow cases but increases tremendously when flow separation occurs. Therefore, the foremost consideration for drag control is to avoid flow separation, which in most cases can be achieved by simply streamlining the body shape. The drag due to lift is caused by flow spillage on lifting surfaces from high- to low-pressure regions. Skin-friction drag is the result of the no-slip boundary condition on the wall and exists in both laminar and turbulent flows. It is equal to the integral of shear stress over the object surface area. Therefore the skin-friction drag in turbulent flow is higher than that in laminar flow. When the flow is attached, it is usually the major contributor to the total drag. For this reason, the reduction of skin-friction drag has been actively pursued by many researchers and will be the subject of study in this chapter.

5.1 Skin-Friction Drag Reduction

It has been known for more than a decade that a surface of grooves, known as riblets, can reduce skin-friction drag through the interaction with the sub-layer streaky structures in turbulent flows if the groves are aligned to the mean flow direction [1,2,3]. Optimally,

as much as 8% of drag reduction has been achieved [4]. Several flight tests performed have also confirmed the drag reduction performance of riblets. Since the riblets have to be in the inner layer (sub-layer) of the boundary layer in order to for the riblets to be effective, they are called internal manipulators. In contrast to the riblets, the large eddy break-up devices (LEBUs) which extend from the surfaces to the outer layer are known as external manipulators or outer layer devices. They can “calm” the flow passing them, thus reducing the drag [5,6]. These two types of manipulators are all *passive* control means for drag reduction because there are no adaptation of the surface to flow. One serious problem with these techniques is that they only work for a narrow velocity range.

In addition to the passive means, a number of researchers have also explored the *active* means for reducing turbulent drags. These include the mass transport through porous walls [7], selective suction and blowing derived from the drag reduction mechanism on a shark’s skin [7,8,9,10], and actuator movements [11,12]. The numerical simulations (CFD) have predicted that the *interactive* drag reduction scheme, i.e. the closed-loop feedback control systems with a large amount of distributed sensors and actuators with sizes comparable to the turbulent structures, can be much more effective than the passive means [7]. However, the experimental realization of such micro systems was not possible until just recently when MEMS technology is developed and introduced to flow control.

5.2 MEMS Skin-Friction Drag Reduction Approach

High skin-friction drag in a turbulent flow is caused by the counter-rotating vortex pairs which bring high momentum fluids down to the wall and create local high shear stress streaks. The basic mechanism of our MEMS skin-friction drag reduction approach is to pump the high momentum fluids in the vortices away from the wall by moving the surface-mounted micro-flaps up and down, thus reducing the surface shear stress. This concept has been proved by hot-wire measurements in the 2-D laminar flow section of the wind-tunnel described in Chapter 4, where a vortex generator is placed on the wall to

induce a stationary vortex pair and a micro-actuator is placed down-stream of the vortex generator [13,14,15]. In Figure 5.1, the drag coefficients (defined as the drag force normalized to the dynamic force) derived from hot-wire measurements are plotted against the phase of the actuator excited by sine waves at different frequencies. It can be seen that the drag coefficients with actuator movements are always lower than that without actuator. In fact, under certain condition (e.g., actuator in the up position at the frequency of 40 Hz), the drag coefficient is even lower than that without the vortex generator, i.e. when the flow is laminar.

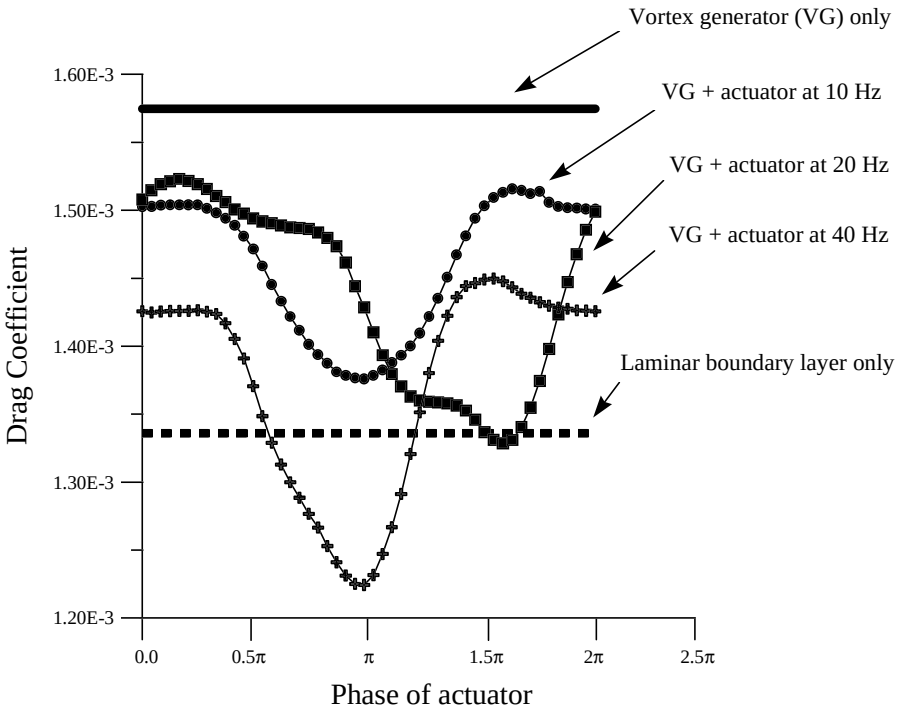

Figure 5.1 Drag coefficient (defined as the normalized drag force to dynamic force) change with the phase of the actuator excited by sine wave with different frequencies.

In addition to the hot-wire measurement, a hybrid MEMS control system using individual actuator, shear stress sensors, and integrated CMOS circuits fabricated through MOSIS is under way to directly confirm the drag reduction capability in fully developed turbulent flows [16].

5.3 System Integration

In the mean time of the drag reduction study using the hybrid system, we are exploring the possibility of integrating the micro-sensors, micro-actuators and microelectronics (M^3) on a single Si chip and eventually making a complete distributed micro-system for drag reduction on a Si wafer. We have developed a technology for the integration of the three different types of devices and the prototype M^3 chips have been fabricated by using this technology, as shown in Figure 5.2. The chip consists of three basic flow control units in parallel. Each unit uses one surface micromachined magnetic actuator with torsional support beams [16]. There are three shear stress sensors biased at constant temperature mode on the upstream of the actuator for measuring the passing sub-layer structures. Their outputs are amplified and then fed to a CMOS edge detector [17,18]. If a high shear stress streak is identified, the edge detector will send a signal to activate the driver of the actuator and the driver then outputs a sinusoidal current to oscillate the actuator. The other three shear stress sensors on the downstream of the actuator are only used to check the effect of the actuation.

The integration process of the CMOS circuits, shear stress sensors and magnetic actuators is far more complex than the sum of the individual processes. First, the CMOS process has to be finished before any MEMS devices are fabricated because of its strict requirement on the wafer cleanness and surface condition. Second, aluminum metallization for the CMOS devices can not be done until all the high temperature (> 450^oC) materials are deposited. Third, the processing temperature during the fabrication of the MEMS devices can not exceed 950^oC in order to prevent the change on the doping profiles of the fabricated CMOS transistors. This has ruled out the possibility of having a separate LOCOS just for MEMS devices. Finally, certain masking materials other than photoresist are needed to protect the structures that are not being processed during various sacrificial layer etchings (high-concentration HF etch, TMAH etch, etc.).

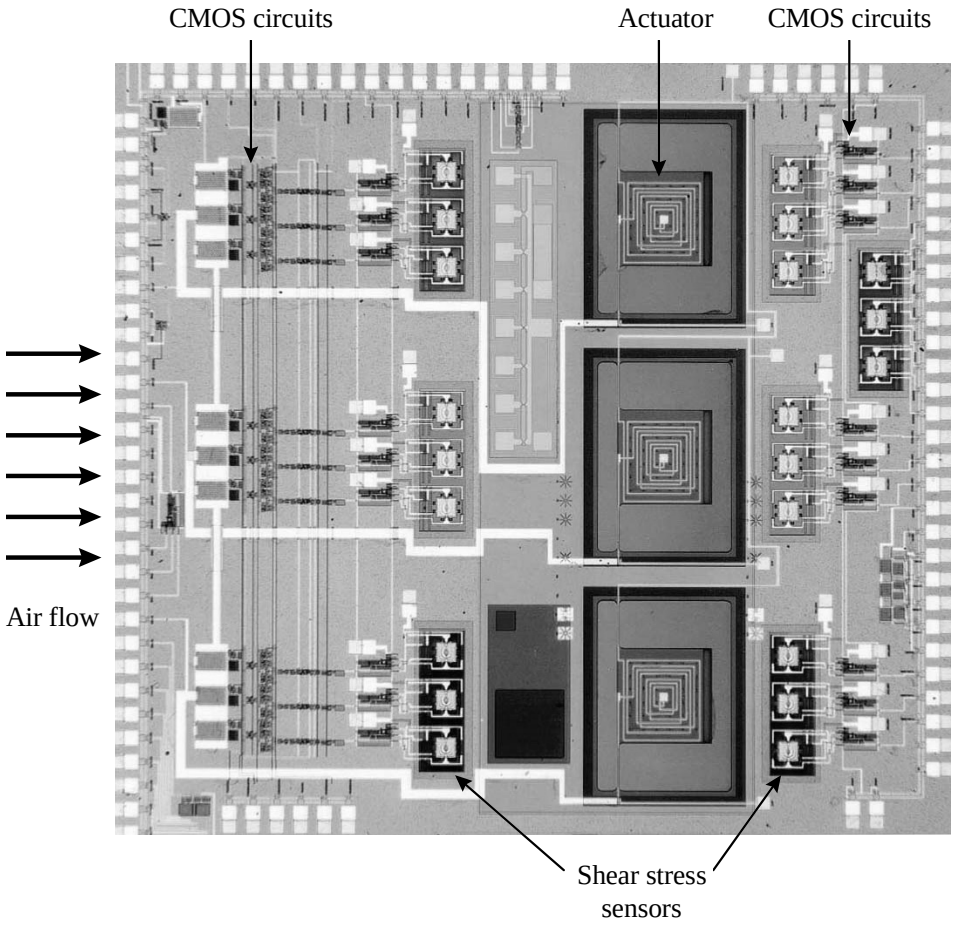

Figure 5.2 A 1×1 cm^2 prototype M^3 chip with integrated shear stress sensors, micro magnetic actuators and CMOS control circuits.

Based on the above considerations, we have designed the process for the fabrication of the prototype M^3 chips, which is described in Appendix A. Totally, the process includes 22 masking steps. The simplified process flow with cross-sections are shown in Figure 5.3. The baseline CMOS process steps up to the deposition of PSG are finished in the Microlab of the University of California at Berkeley. The wafers are then sent to our lab for the fabrication of the shear stress sensors and the processing of the high temperature materials for the actuators. Metallization for the CMOS circuits and the shear stress sensors are completed in Berkeley. Finally, we finish the low temperature processing steps for the actuators, including the deposition and patterning of LTO and chrome/gold, and the sacrificial layer (polysilicon) etching in TMAH and BrF_3 [16].

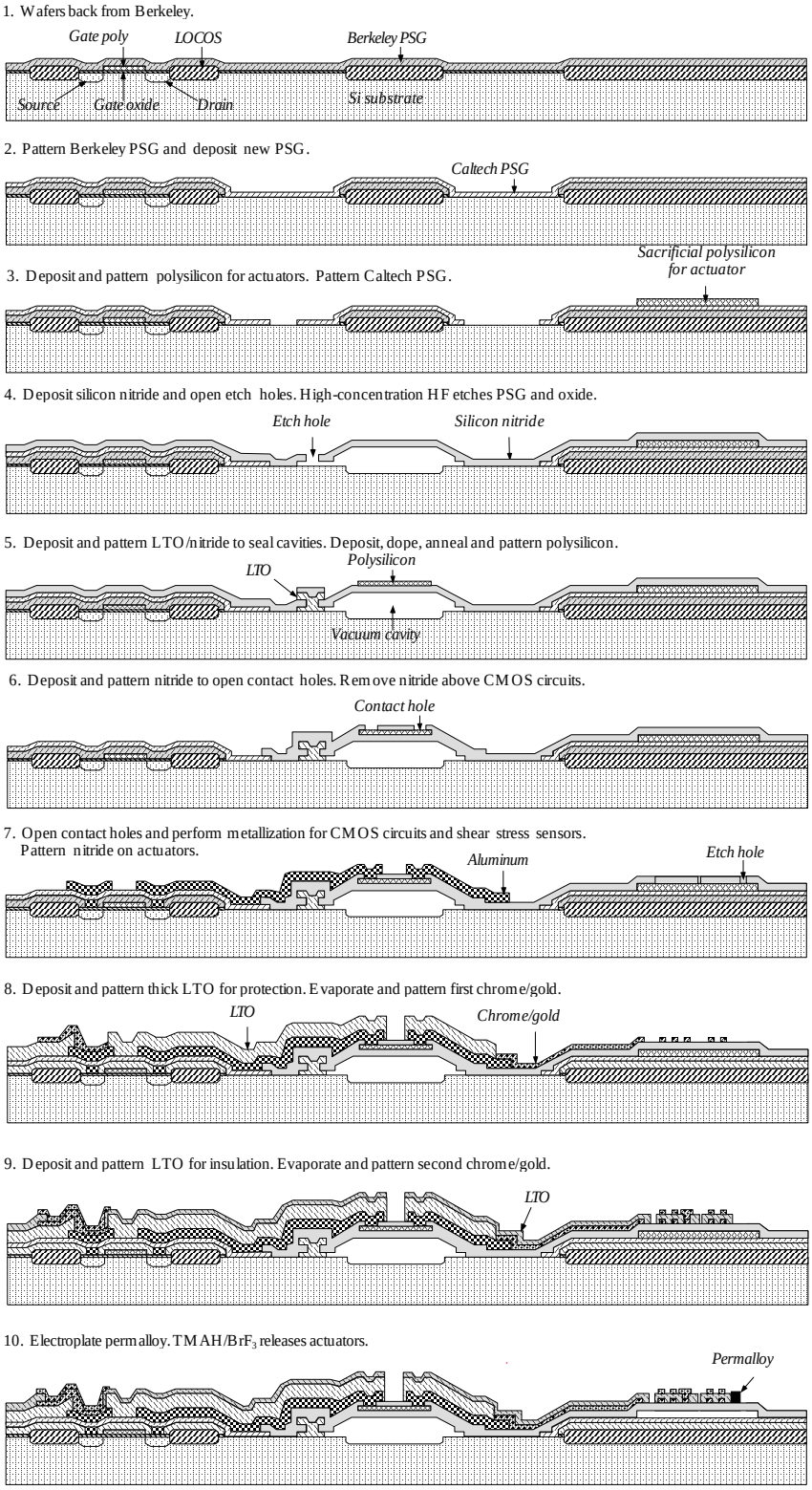

Figure 5.3 Simplified process flow the prototype M^3 chips.

Figure 5.4 shows the picture of a shear stress sensor on the M^3 chips. It is slightly different from sensors on the shear stress imagers. First, the polysilicon wire is chosen to be 15 μm wide so that the voltage drop across the 1:1 Wheatstone bridge in the CT circuit is below 5V. Second, the LOCOS thickness in Berkeley baseline CMOS process is only 0.7 μm, much less than the required 1.8 μm. We have used the 0.7 μm Berkeley PSG to compensate the LOCOS thickness. Meanwhile, we have increased the thickness of our own PSG from 0.4 μm to 0.6 μm in an attempt to further deepen the cavities to the normal 2 μm. However, these were not enough to keep the 1.2 μm thick diaphragms away from the bottom of the vacuum cavities due to the much different boundary conditions (Figure 5.5). It has been found that we need 1.6 μm or thicker diaphragms to prevent them from being sucked down to the cavity bottoms by the vacuum.

The overall wafer surface roughness before the contact hole opening and metallization for the CMOS circuits is about 2.7 μm as a result of lifting the diaphragms above wafer surfaces, which has greatly exceeded the 1 μm limit accepted by the CMOS process vendors who generally use thin photoresist for their UV lithography in order to get fine-line features. Therefore, the lithography for the contact opening and metallization of the CMOS circuits can only be done in our lab using thick photoresist. This would more or less affect the yield of the 2 μm CMOS transistors. Nevertheless, we have found that the test transistors on the wafers with finished shear stress sensors have the same yield (80-90%) as those on the wafers which only went through the complete baseline process in Berkeley Microlab. The threshold voltages of the test transistors on all wafers are about 0.8 V. This means that the additional processing steps at temperatures up to 900^oC did not have significant effect on the performance of the CMOS transistors.

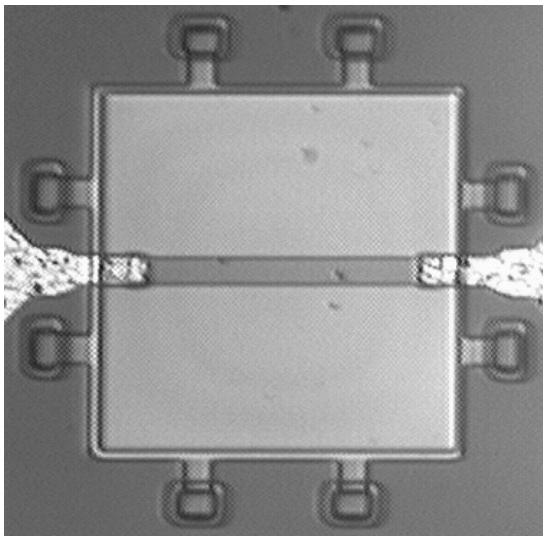

Figure 5.4 Photograph of the low voltage shear stress sensor on a M^3 chip. The polysilicon wire is 15 μm wide and 150 μm long. The Newton rings are the result of the bending on the diaphragm by the vacuum underneath.

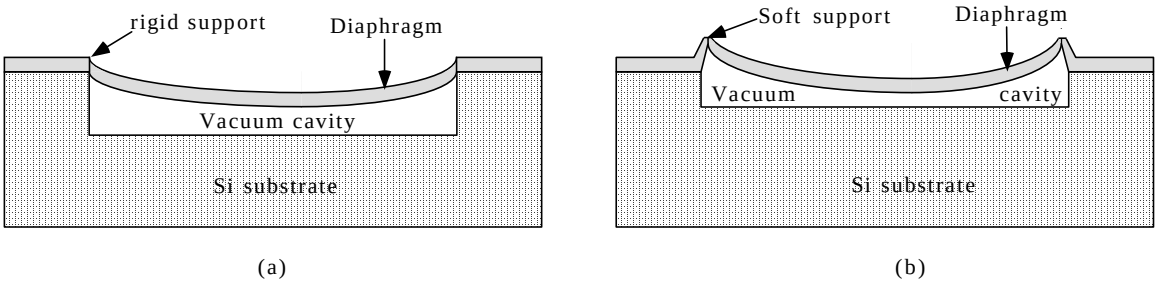

Figure 5.5 Deflection of diaphragms on top of vacuum cavities with (a) rigid and (b) soft supports.

For future efforts on the integration, we need to look into other commercial CMOS process foundries who have better yields and more flexibility in accommodating certain process steps which are important to our MEMS devices but still compatible with the CMOS process. For example, a 1 μm deep fully recessed LOCOS is not difficult to develop and is acceptable to a 2 μm CMOS process, but it can greatly reduce the surface roughness of the shear stress sensors. The proposed cross-sectional design shown in Figure 5.6 has a surface roughness less than 1.4 μm, thus allowing the wafers with

fabricated shear stress sensors to go back to the vendors to finish the remaining CMOS process steps (contact opening and metallization).

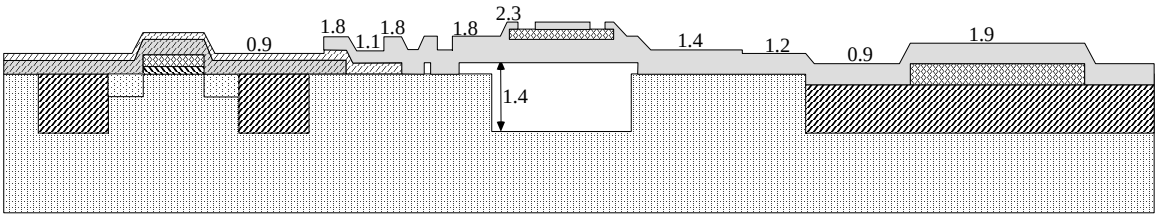

Figure 5.6 The proposed design with 1 μm fully recessed LOCOS and greatly reduced surface roughness. The numbers are the surface levels relative to the silicon surface in unit of microns.

5.4 Conclusion

We have described a novel approach that is capable of controlling turbulent boundary structures and reducing the skin-friction drag through the interaction between the flow and the micro transducers. We have also developed a technology for the integration of micro-sensors, micro-actuators and microelectronics on a single chip (M^3 chip). Prototype M^3 chips designed for the skin-friction drag reduction and consisting of micro shear stress sensors, micro magnetic actuators and CMOS circuits have been fabricated by using this technology. However, some improvements on the design of process, layout and circuits need to be done before we can produce a working M^3 chip for drag reduction.

Bibliography

[1] M. J. Walsh, “Drag Characteristics of V-Groove and Transverse Curvature Riblets,” *Proc. Symp. On Viscous Drag Reduction*, Dallas, 1979.

[2] M. J. Walsh and A. M. Liindermann, “Optimization and Application of Riblets for Turbulent Drag Reduction,” AIAA Paper 84-0347, 1984.

[3] P. Vukoslavcevic, J. M. Wallace, and J. L. Balint, “Viscous Drag Reduction Using Streamwise-Aligned Riblets,” *AIAA J.*, Vol. 30 (4), pp. 1119-1122, 1992.

[4] B. Lazos and P. Wilkinson, “Turbulent Viscous Drag Reduction with Thin-Element Riblets,” *AIAA J.*, Vol. 26 (4), pp. 496-498, 1988.

[5] J. N. Hefner, L. M. Weinstein, and D. M. Bushnell, “Large-Eddy Break-up Scheme for Turbulent Viscous Drag Reduction,” *Proc. Symp. On Viscous Drag Reduction*, Dallas, 1979.

[6] A. P. Dowling, “The Effect of Large-Eddy Breakup Devices on Oncoming Vorticity,” *J. Fluid Mech.*, Vol. 160, pp. 447-463, 1985.

[7] H. Choi, P. Moin, and J. Kim, “Active Turbulence Control For Drag Reduction in Wall-Bounded Flows,” *J. Fluid Mech.*, Vol. 262, pp. 75-110, 1994.

[8] D. W. Bechert, G. Hoppe, and W. E. Reif, “On the Drag Reduction of the Shark Skin,” AIAA Paper 85-0546, 1985.

[9] M. Gad-el-Hak, R. F. Blackwelder, “A Drag Reduction Method for Turbulent Boundary Layers,” AIAA Paper 87-0358, 1987.

[10] S. P. Wilkinson, “Direct Drag Measurements on Thin-Element Riblets with Suction and Blowing,” AIAA Paper 88-3670, 1988.

[11] H. A. Carlson and J. L. Lumley, “Active Control in the Turbulent Wall Layer of a Minimal Flow Unit,” *J. Fluid Mech.*, Vol. 329, pp. 341-371, 1996.

[12] S. P. Wilkinson, “Interactive Wall Turbulence Control,” *Viscous Drag Reduction in Boundary Layers, Progress in Astronautics and Aeronautics*, Vol. 123, pp.479-509, 1989.

[13] R. Miller, Y. C. Tai, G. Burr, D. Psaltis, C. M. Ho, and R. Katti, "Electromagnetic MEMS Scanning Mirrors for Holographic Data Storage," *Solid-State Sensor and Actuator Workshop*, Hilton Head, SC, pp. 183-186, 1996.

[14] C. H. Ho, S. Tung, and Y. C. Tai, "Interactive Control of Wall Structures by MEMS-Based Transducers," *Proc. of the Sixth European Turbulence Conference*, Lausanne, Switzerland, p. 413, 1996.

[15] C. H. Ho, S. Tung, G. W. Lee, Y. C. Tai, F. Jiang, T. Tsao, "MEMS - A Technology for Advancements in Aerospace Engineering," AIAA Paper 97-0545, 1997.

[16] T. Tsao, F. Jiang, R. Miller, Y. C. Tai, B. Gupta, R. Goodman, S. Tung, and C. H. Ho, "An Integrated MEMS System for Turbulent Boundary Layer Control," *Transducers'97*, Chicago, pp. 315-318, 1997.

[17] B. Gupta, R. Goodman, F. Jiang, Y. C. Tai, S. Tung, and C. H. Ho, "Analog VLSI System for Active Drag Reduction," *IEEE Micro*, Vol. 16 (5), pp. 53-59, 1996.

[18] B. Gupta, *Analog VLSI for Active Drag Reduction*, Ph. D. Thesis, The California Institute of Technology, 1997.

Chapter 6

Flexible MEMS Technology and Shear Stress Sensor Skin

6.1 Introduction

In some research involving the study and control of a distributed system, it is essential to obtain the real-time profiling of certain physical parameters such as temperature, force, pressure or shear stress on a 3-D object. If the surface of the object is flat, the profiling can be achieved by using a monolithic MEMS sensor array [1]. However, this can be much more difficult if the surface is non-planar. For example, in aerodynamics study, the most popular research objects such as an air foil have non-planar or even high-curvature surfaces. In the past, when real-time distribution measurement was necessary, embedding all the discrete sensors on a surface was the only way. Nevertheless, large sensor size and difficulty in packaging, i.e., plumbing and wiring, have limited the wide application of these measurements.

It has been our goal to develop a flexible MEMS technology to produce smart skins (with integrated MEMS devices) that can be easily taped or glued on non-planar surfaces. Retrospectively, Barth et al. [2] in 1985 reported the first version of this idea with a one-dimensional flexible Si-diode temperature sensor array in which a polyimide strip was the flexible material connecting Si islands formed by isotropic HNA etching. However, the authors claimed that this technology needed some major improvements before it could be applied to more sophisticated sensor systems. This sensor skin concept, unfortunately, was not pursued further until 1994, when Beebe and Denton [3] presented their effort on improving the robustness and reliability of flexible polyimide skins. Their skins did not

bear any real devices. The major lead failure mechanism was identified as the breakage of the thin silicon on the island periphery (Figure 6.1). Since the basic process was the same as that developed by Barth, the methods used to enhance the robustness, including taping and coating of epoxy on both front and back sides of the skins, were all performed manually as post-processing steps. It is obvious that these are not the ideal solutions for a reliable as well as mass-producible smart skin technology. Recently, we learned that, almost concurrent to our effort, Bang and Pan [4] also have an on-going project to develop a flexible heat-flux sensor array which is made by direct deposition of thin-film metals on commercial Kapton polyimide substrates, based on the smart skin technology reported by Mehregany et al. [5]. As a matter of fact, this basic technology is nothing new and has already been used to make polyimide-based hot-film shear stress sensors [6,7,8,9,10,11]. A large array of metal temperature sensors can be made in this way, but its drawback is that neither ICs nor silicon MEMS can be integrated with this approach; hence, only limited types of sensors are available and hybrid assembly of electronic circuits is unavoidable.

In comparison, the work we present here is a new flexible skin technology designed to be compatible with both IC and MEMS fabrications. Due to the much stronger periphery of the silicon islands formed by nearly vertical RIE, the skin reliability has been greatly improved. Moreover, we have realized a 2-D flexible skin integrated with more than 100 shear stress sensors. This skin has further been mounted on a 3-D leading edge of a delta wing and successful 2-D shear stress measurements are obtained. For the first time, the air flow boundary layer separation over the leading edge of a delta wing is determined experimentally in real time.

6.2 Flexible Skin Technology

As mentioned in the previous section, almost all the lead failures on the flexible skins made by Barth and Beebe were caused by the breakage of the thin peripheries on the Si island during the squeezing and folding test. The thin and weak Si island periphery was

the natural result of isotropic HNA etching (Figure 6.1a). In comparison, the island shapes formed by caustic anistropic etchants such as TMAH or KOH and by the combination of anisotropic etching and RIE are much more robust when subjected to squeezing and folding (Figure 6.1b & c). Unfortunately, the above caustic etchants attack all types of polyimides, so that polyimide layers must be coated after the islands are formed or protected from the etchants during the etching. Using gold or other expensive metals as the protection materials is not only costly, but also incompatible with IC processes. The one-sided etching apparatus is not usable as the pressure difference between the two sides would cause the rupture of the polyimide near the end of the etching, or a small leak on the wafer near the end of the etching would attack the polyimide on the front side. The approach of coating polyimide after island formation is not feasible either, unless proper material remains to support the islands after the etching and can be removed with ease after the polyimide is coated. Our new flexible MEMS technology is based on this idea with additional modifications.

Figure 6.2 is the simplified process flow of this new technology. It starts with selective TMAH or KOH etching on the backside of a double-side polished (100) Si wafer with silicon nitride being the mask material to form a Si membrane of desired thickness. Aluminum is evaporated on the front side and patterned to cover the area between future Si islands. Polyimide is spun-on, cured and patterned to cover the patterned Al completely. Normal Al metallization then follows to provide electrical leads. Another polyimide layer is spun-on and patterned to expose the bonding pads. RIE etching on the backside using Al as masking material removes the Si on the streets between Si islands. Here the first layer of Al serves as the etch stop during this SF_6-based RIE etching step. Finally, a thick polyimide layer is spun-on and cured on the backside to sandwich the Si islands. The finished skins are then cut off from the Si wafer frame by a razor blade.

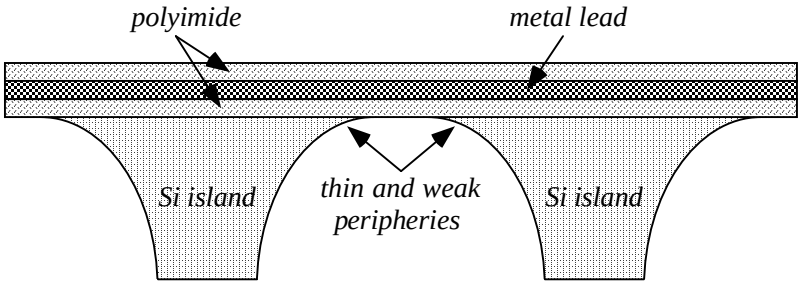

(a) by HNA isotropic etching.

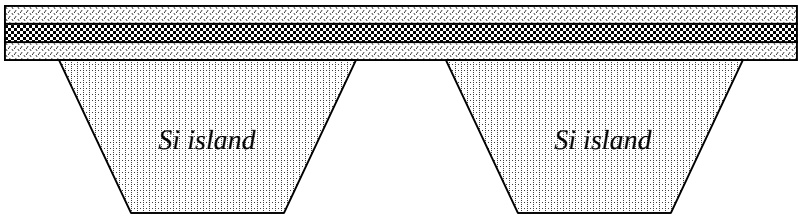

(b) by anisotropic etching (TMAH or KOH).

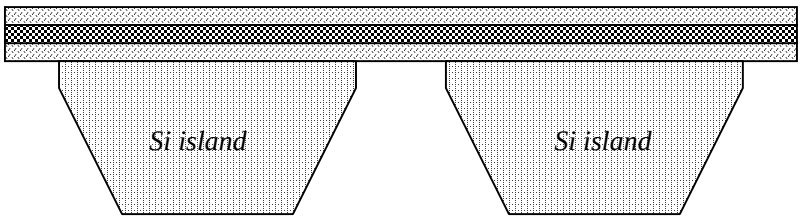

(c) by a combination of anisotropic etching and RIE.

Figure 6.1 Si island shapes formed by different ways.

Figure 6.3 shows the photograph of a fabricated flexible skin about 8 cm in diameter with 2 x 2 mm^2 Si islands. Since we are only demonstrating the concept here, the skin did not contain actual devices. However, it is obvious that the above process is compatible with IC process as it involves only aluminum and polyimide which are commonly used in IC fabrication. We can start with a wafer with fabricated IC and MEMS (without metallization) and the above process needs only minimal adjustment to produce flexible MEMS skins. Such flexible MEMS skins have already been realized and will be presented in the next section.

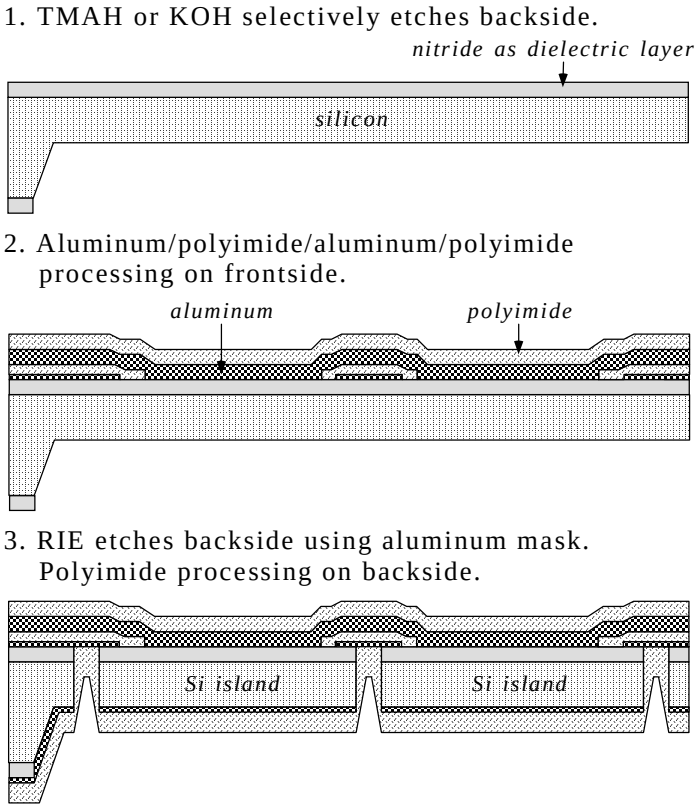

Figure 6.2 Simplified process flow of the new flexible skin technology.

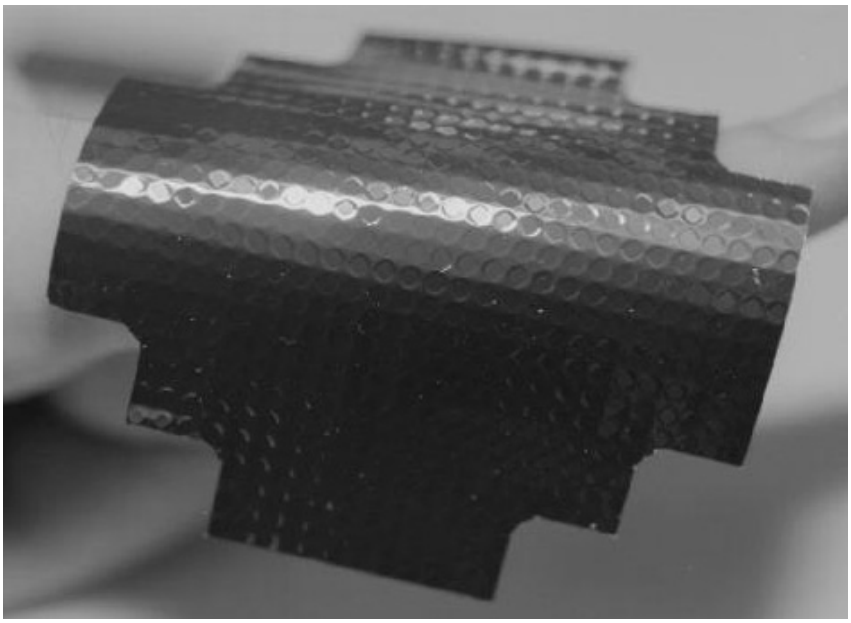

Figure 6.3 Picture of a wafer-size flexible skin.

In the above process, the Si islands are formed by RIE-etching the Si diaphragm. Since the diaphragm thickness is less than 100 μm and the RIE etching is nearly vertical, we can well-define islands with dimension as small as 100 μm and spacing less than 50 μm, which makes it possible for the skin to be applied on a very high-curvature surface with good conformal coverage. For obvious reasons this can not happen if any of the island-forming techniques shown in Figure 6.1 are used (HNA etching is isotropic and TMAH or KOH etching requires large corner compensation structures to avoid fast undercut of corners). Of course, there is some disadvantages in using Si diaphragm and thin islands. First, extreme care must be taken of the wafers during processing as they are very fragile. However, if the individual skin is not too big, the wafers are reasonably robust to survive the whole process. Moreover, if a robust one-sided wet Si etching or deep RIE etching is available, the formation of Si diaphragm can be delayed until all the processing steps on the wafer front side are finished, thus reducing the risk of wafer breakage significantly. Second, thin Si islands can not take as much force as thick ones. This is generally not a concern for most applications where the skins do not contact other objects after being mounted.

Table 6.1 Properties of DuPont Pyralin® PI-2808 polyimide.

Density	2.3 g/cm^2
Tensile strength	210 MPa
Young's modulus	2.3 GPa
Elongation at break	88%
Stress for 10 μm thick film	18 MPa
Peel test adhesion	0.23 g/mm
Dielectric constant	3.3
Cure temperature	350 °C
Decomposition temperature	580 °C

Polyimide was chosen as flexible skin material, just as in the previous works due to

its good mechanical strength and flexibility. We used DuPont's Pyralin® PI-2808 polyimide which has a tensile strength of 210 MPa [12]. This value is one of the highest among all the spin-coated polyimides and is almost the same as that of Kapton (231 MPa) [13], a product also made by DuPont and commonly used as a flexible runner for providing reliable connections to moving print heads. Some properties of the PI-2808 polyimide are listed in Table 6.1.

In the process, the thickness of each polyimide layer on the front side of the wafer is 3-4 μm after curing at 350°C. Since the polyimide layers are not exposed to strong acids or bases, their mechanical properties are not degraded. Then a total of 7 μm thick polyimide on the front should be able to stand a tensile force of 1.47 kg/mm, which is fairly strong. However, the peel-off forces of the polyimide from Si substrates given by the manufacturer is only about 0.23 g/mm. Therefore, even a very small shear force exerted on a Si island would peel it off. One solution to this problem is to spin thick polyimide (10 μm) on the back side of the wafer to fully encapsulate the islands. The total polyimide thickness between islands becomes 17 μm and the maximum tensile force that the skin can stand is increased to 3.57 kg/mm.

As for the metal leads, they are completely embedded in two polyimide layers on the flexible area. Also, the Si islands they are sitting on do not have weak edges. Therefore, they should be able to stand repetitive squeezing and bending without breakage. In our initial testing, no metal lead failure has been observed after more than 100 times of 90°-180° bending.

6.3 Flexible Shear Stress Sensor Array

It is important to demonstrate that useful MEMS devices can indeed be integrated on a flexible substrate with this flexible skin technology. Based on the following two considerations, we target our first effort on the development of a flexible shear stress sensor array. First, the micromachined thermal shear stress sensor we developed previously has been useful in turbulent flow study since its invention. For example, arrays

of shear stress sensor on a rigid substrate have been used to detect the real-time shear stress distribution on a flat (i.e., 2-D) surface for flow-induced drag reduction study [1,14]. However, its application has so far been limited to 2-D flow due to the lack of flexible packages. The development of a flexible shear stress sensor array is the only way to extend its application to 3-D flow. Second, the fabrication of shear stress sensors is a surface micromachining process with reasonably high complexity. It will be a good demonstration of the compatibility between the flexible skin and MEMS technologies.

Figure 6.4 shows the simplified fabrication process flow with cross-sections of the flexible shear stress sensor array. The detailed process description is in Appendix A. It is basically the combined fabrication processes for the shear stress sensor and the skin. The only mixing is that contact holes are opened after the first aluminum/polyimide processing so that they are fresh and clean for the immediately following metallization. High-quality double-side polished (100) Si wafers and good double-side alignment marks made at the very beginning of the fabrication are crucial to this complicated process. Figure 6.5 and Figure 6.6 are the photographs of a shear stress sensor and the finished flexible sensor respectively. The skin is 1 cm wide, 3 cm long, and it consists of two 32-sensor rows with a horizontal pitch of 635 μm and many other test devices (a total of more than 100 sensors). The two sensor rows are 5 mm apart and located between the pairs of white square boxes in the picture. Their bonding pads are extended to the left and right edges of the skin. The layout is designed in such a way that each sensor row spans the semi-cylindrical surface (1.3 cm in diameter) of a delta wing leading edge under study with an angular resolution of 5.6^{o}. Each sensor occupies 250 x 250 μm^2 and the dimension of each Si island is 450 μm x 550 μm (75 μm thick) to fully accommodate one sensor and to achieve excellent surface smoothness and conformability. Fig. 7 shows the picture of a skin sitting on a conic object. Its good flexibility is seen from the bending of the skin due to gravitation.

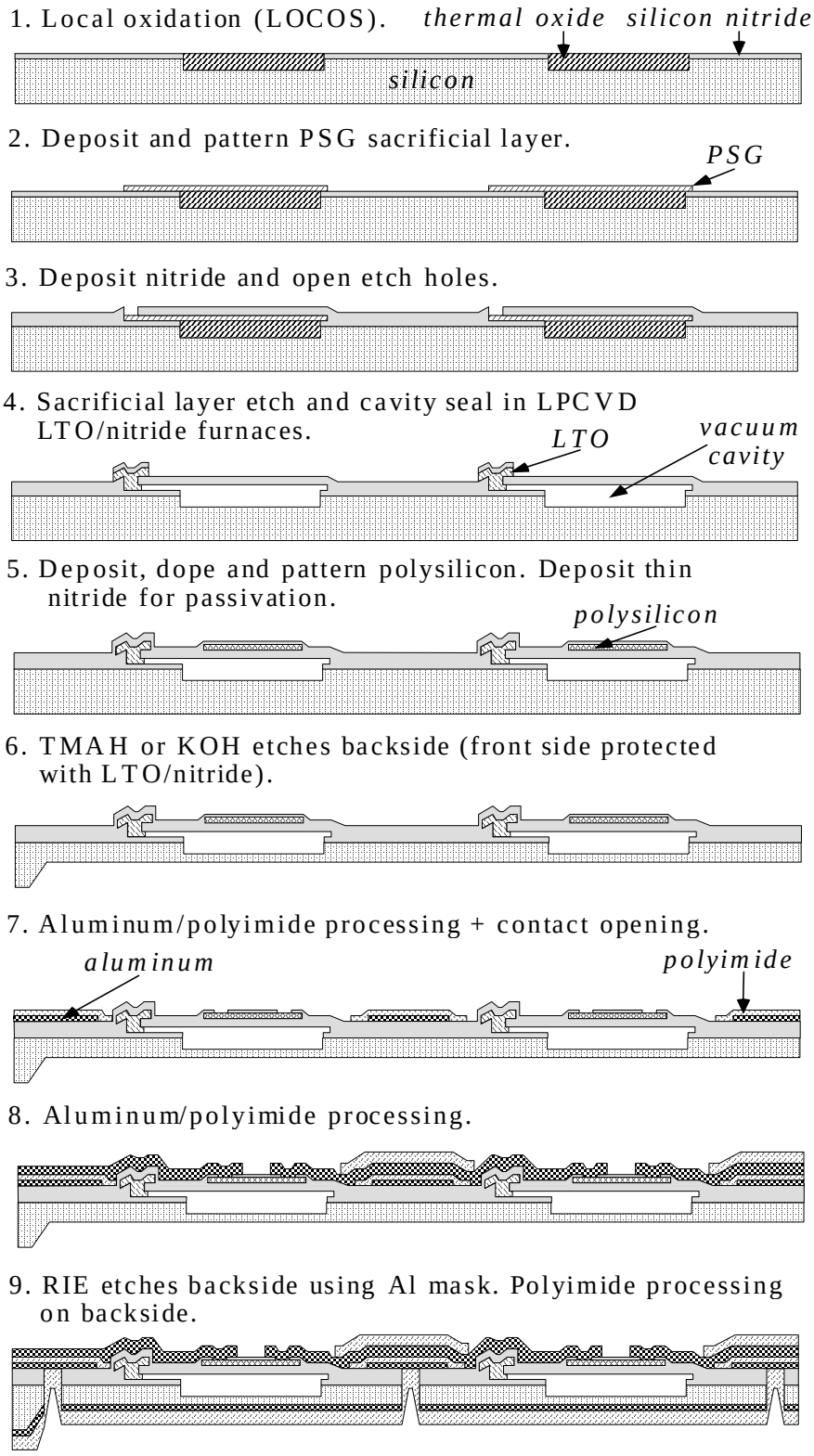

Figure 6.4 Fabrication process flow of the flexible shear stress sensor skin.

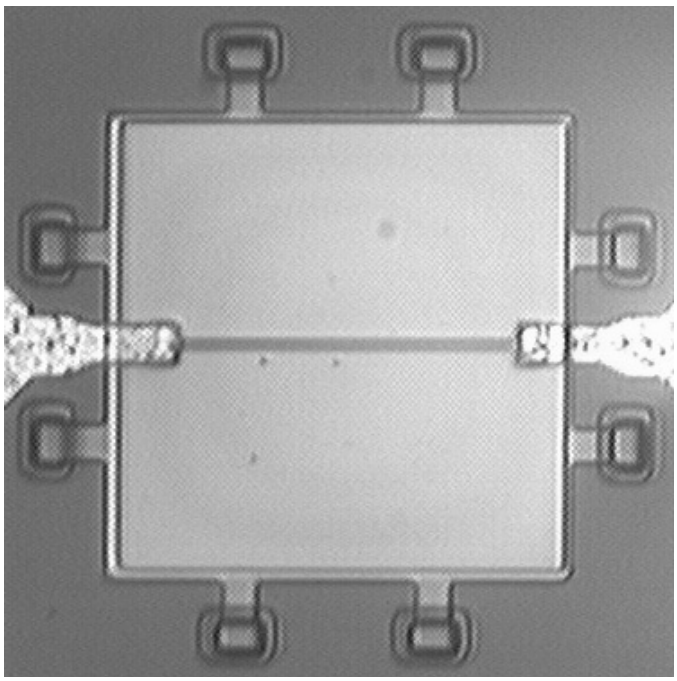

Figure 6.5 Photograph of a shear stress sensor. A square silicon nitride diaphragm (200×200 μm^2) with an embedded polysilicon wire is on top of a vacuum-sealed cavity.

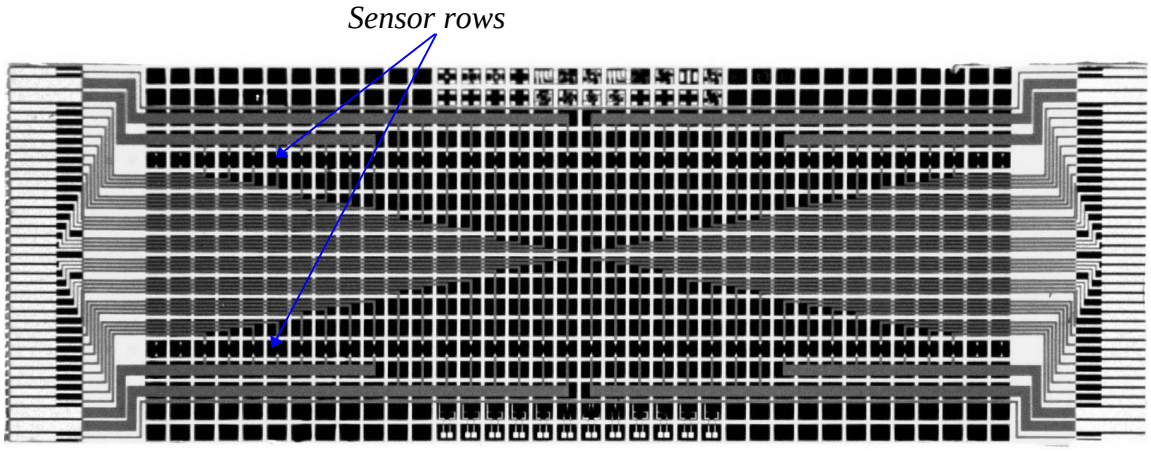

Figure 6.6 Picture of a flexible shear stress sensor array (1 cm × 3 cm).

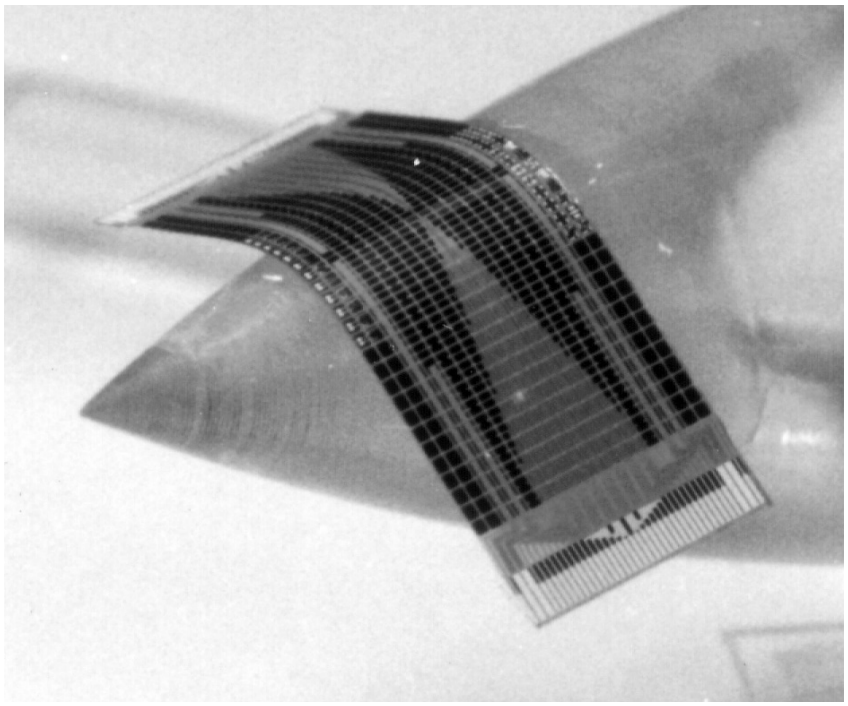

Figure 6.7 A flexible shear stress sensor skin sits on a conic object. The bending is caused by gravitation.

6.4 Packaging and Calibration of the Shear Stress Sensor Skin

The shear stress sensor skin is specially designed for the shear stress measurement on the leading edges of the delta-wing model in the UCLA Fluid Mechanics Laboratory, which is shown in Figure 6.8. It has a swept angle of 56.5^{o}. The leading edges span 36.5 cm from the apex to the trailing edge. Their surfaces are semi-cylindrical with a diameter of 1.3 cm. For the testing purpose, the leading edges are detachable and one of them is further divided into many blocks of removable semi-cylinders 2 cm long and 1.3 cm in diameter. The block on which the sensor skins will be mounted is recessed by about 100 μm to compensate the skin thickness. By moving the skin block along the whole leading edge block by block, we are able to map out the steady-state shear stress distribution, which is enough in laboratory testing. Of course, if instantaneous shear stress profiling is required, the whole leading edge surface has to be covered with sensor skins. This will be difficult, if not impossible, because of the huge amount of external leads and

electronics involved. The best solution will be the integration of sensors with electronics, as we will discuss later in this chapter.

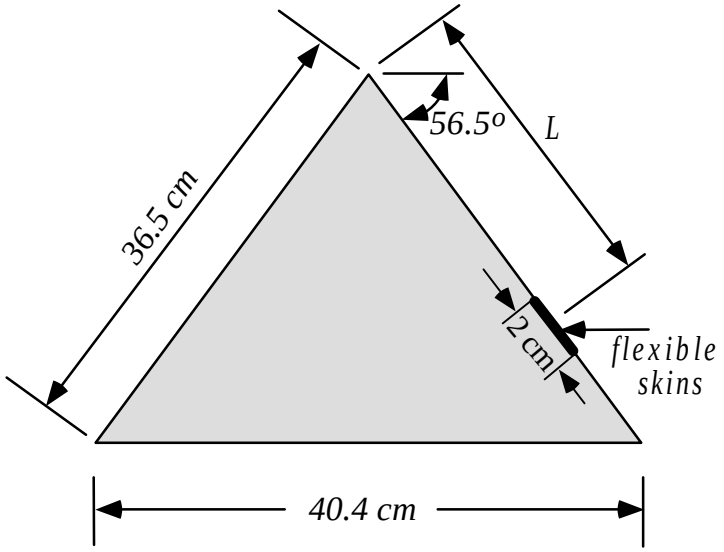

Figure 6.8 Schematic of the delta wing.

Figure 6.9 shows the schematic of the cross section of the packaged skin block. The packaging procedures are as follows: first, two skins are glued to the semi-cylinder with the sensors on the curved surface and the bonding pads extended to the flat surface; then a circuit board with pre-soldered wires is attached to the flat surface next to the bonding pads of the skins; ultrasonic wire bonding is performed to electrically connect the sensor leads on the skin to the circuit board; finally the bonding wires are fixed by epoxy. Here, the circuit board is a piece of Si with gold bonding and soldering pads specially designed and fabricated for this purpose (Figure 6.10). The finished block is then shown in Figure 6.11, which is ready for delta wing testing.

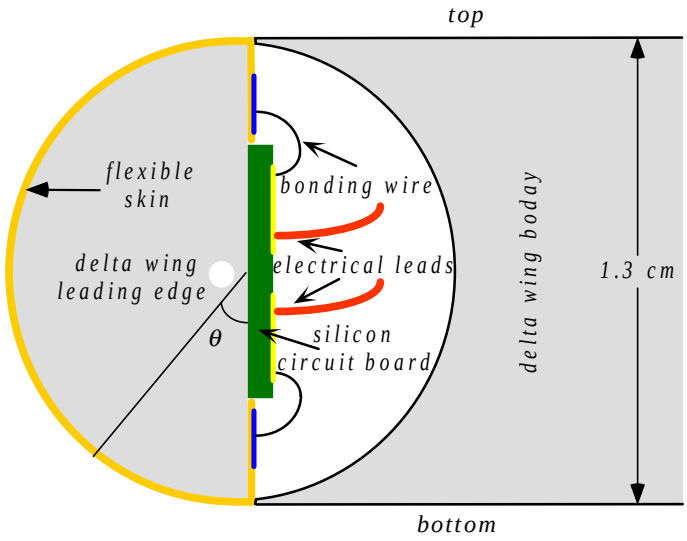

Figure 6.9 Packaging scheme for the flexible shear stress sensor skin on delta wing leading edge block.

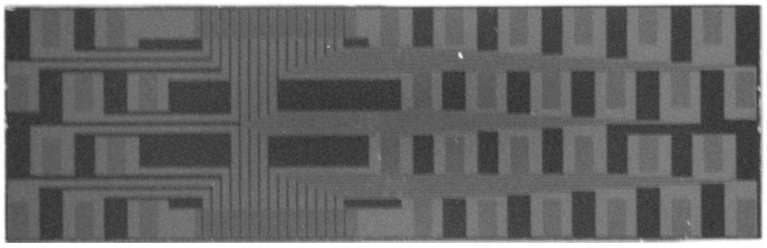

Figure 6.10 Picture of a Si circuit board.

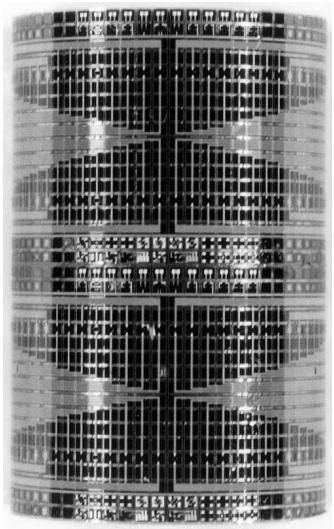

Figure 6.11 Two flexible skins wrapped around on a semi-cylindrical block, 2 cm long and 1.3 cm in diameter.

Before the packaged skin block is mounted on the delta wing for shear stress distribution measurement, it is calibrated by using the flow-over-cylinder method. The skin block and the other dummy blocks are combined together to form a long semi-cylinder. Another piece of semi-cylinder with the same length is attached to the long semi-cylinder to form a full cylinder, which is placed inside the wind tunnel with the skin surface facing the flow. The sensor outputs at different flow velocities are measured by using an A/D converter. Since the shear stresses at different ϕ on the middle section of the cylinder can be calculated from the flow velocity, the sensors are calibrated. These calibration results agree well with those obtained in a fully developed 2-D channel flow where a skin is flushed mounted on the wind-tunnel wall (Figure 6.12). We can conclude that the sensors on the flexible skin behave the same as those on rigid substrates because the square of the output voltage is proportional to the one-third power of shear stress τ with a sensitivity of 100 mV/Pa under constant temperature bias.

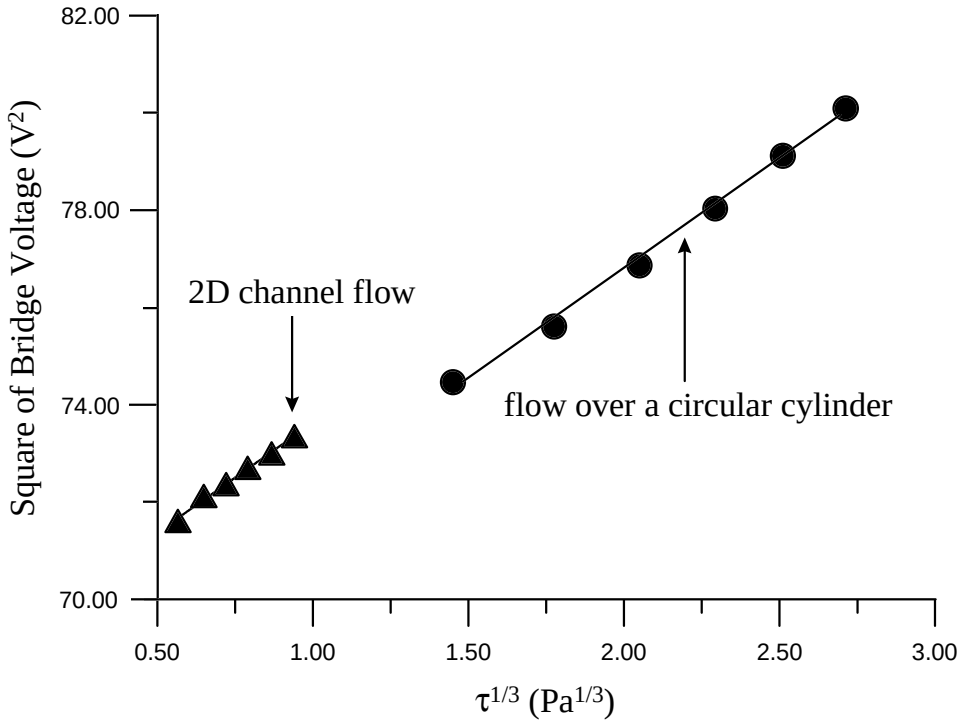

Figure 6.12 Calibration results of the sensors on flexible skins.

Another interesting result obtained from the flow-over-cylinder calibration method is the detection of flow separation by the sensor skin. In Figure 6.13, the local shear stress has a minima at $\phi \approx 85^{o}$, which is corresponding to the flow separation point in the 2-D flow field. This value is very close to that reported by other researchers [15,16].

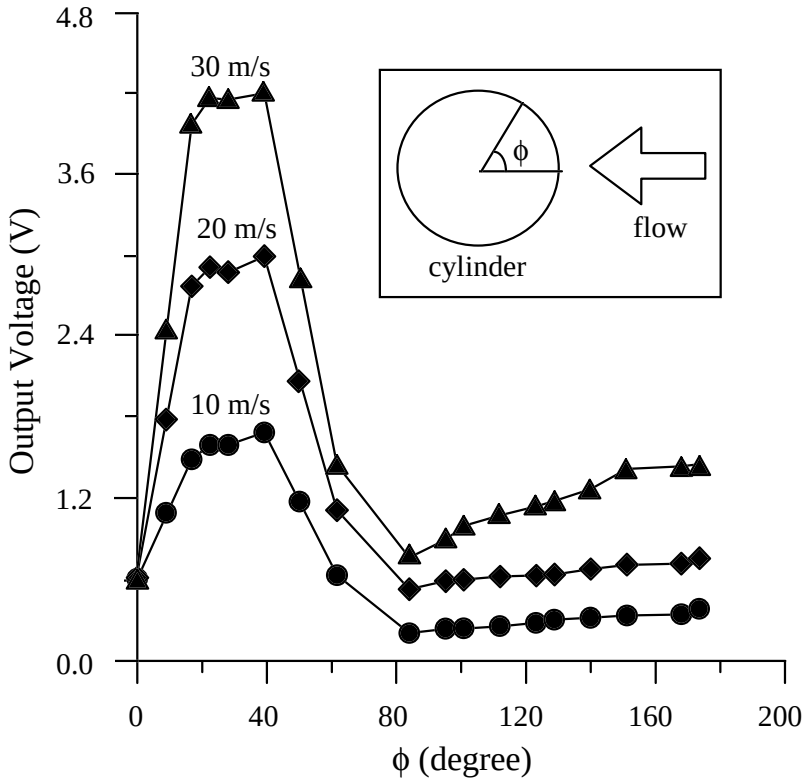

Figure 6.13 Flow separation at $\phi \approx 85^{o}$ on a cylinder is detected during the calibration.

6.5 Measurement on Delta Wing

The operation of a delta-wing at certain angle of attack depends on the counter-rotating leading edge vortex pair, as shown in Figure 6.14. Recently, there have been some studies on manipulating the vortex patterns to achieve better stability and maneuvrability at high angle of attack. The control scheme developed by the UCLA-Caltech research group is to selectively activate millimeter-size micro-flaps on the leading edge curvature. It has been experimentally confirmed that the control is most effective when the flaps just before the flow separation line are deflected out of plane

[17,18]. Therefore, the correct measurement of the flow separation line along the leading edge surface is essential to the success of this control scheme.

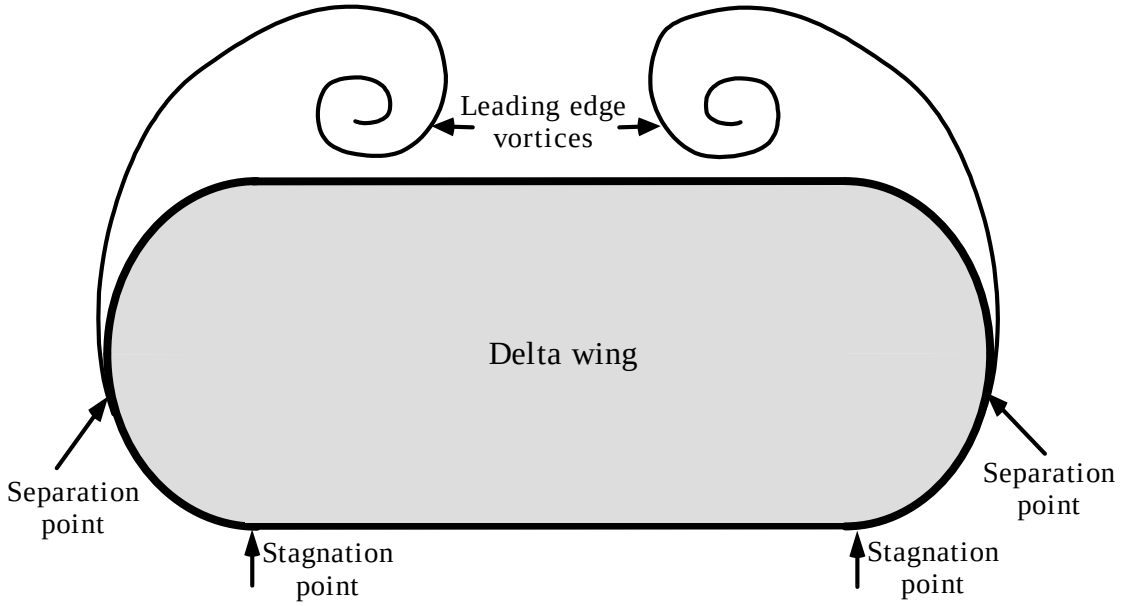

Figure 6.14 Flow separation on the leading edges of a delta wing.

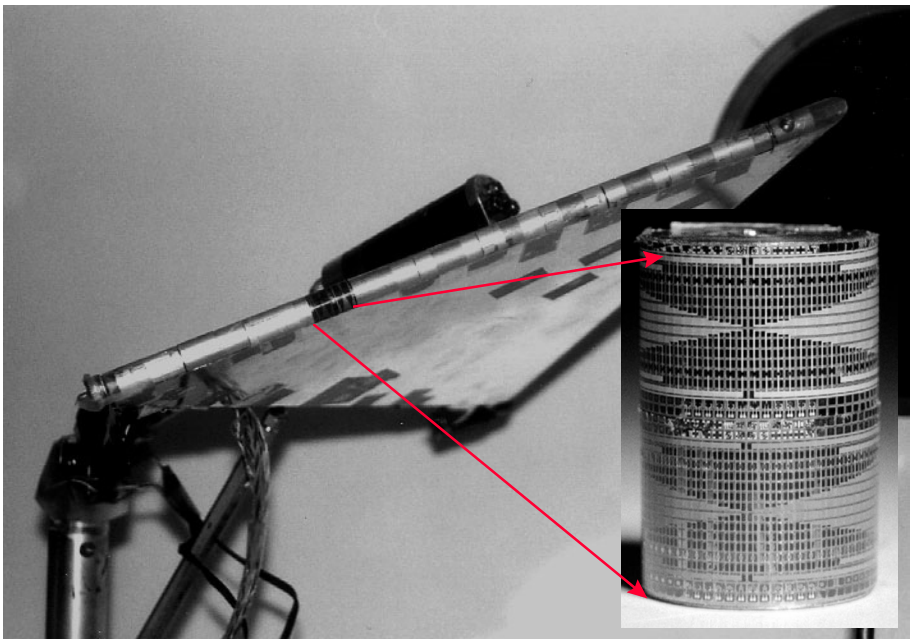

Figure 6.15 Picture of the skin-mounted delta wing model.

The test section of the wind-tunnel used for this study is 22 ft (6.7 m) long with a cross-sectional area of 3 ft by 3 ft or 0.9×0.9 m^2. The maximum air flow speed is 45 m/s. Figure 6.15 shows the delta wing model together with the mounted flexible skins installed in the wind-tunnel. The Reynolds number can be calculated by using the chord length of the delta wing, i.e., the distance from the apex to the middle of the trailing edge, as the characteristic length l. It is about 5.4×10^5 at an air flow speed of 30 m/s.

Measurements have been done for different flow velocities (U), skin locations (L) and angles of attack (AOA, defined as the angle between the air flow and the delta wing plane). For example, Figure 6.16 shows the averaged output voltages (after gain of 10) of the sensors for U = 30 m/s, L = 29 cm and $AOA = 30^o$. Sensor locations are indicated by θ, which is 0° at the bottom surface and 180° at the top surface. The averaged shear stress has a minima at about 110^o. Here, we can not assume that the flow boundary layer starts to separate from the leading edge surface at this location because the 3-D flow field is much more complicated than the flow over a cylinder. Fortunately, there is another unique phenomenon related to the flow separation, that is, the surface shear stress fluctuation stays low before separation, and rises sharply after separation (Figure 6.17). Therefore, we can identify a separation point through the measurement of the root-mean-square (RMS) value of shear stress fluctuation. Figure 6.18 shows the RMS results of one measurement, from which the separation point is found to be at $\theta = 80^o$. In fact, this is the first time separation points are experimentally determined in real time. The separation line along the leading edge is consistent with the data measured from a single shear stress sensor that was placed around the leading edge point by point in steady state flow (Figure 6.19) [19]. Based on our data, it is concluded that, for real time flow control, a single sensor is no longer enough and the flexible shear stress arrays are necessary because the flow separation point along the leading edge is a function of changing U, L and AOA in real flow field.

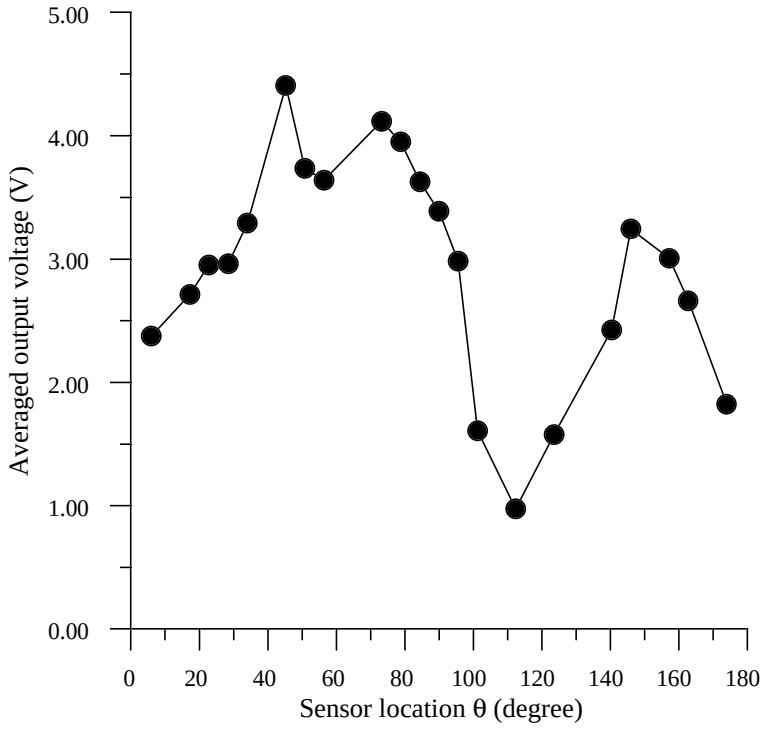

Figure 6.16 Averaged output from one row of sensors on a skin.

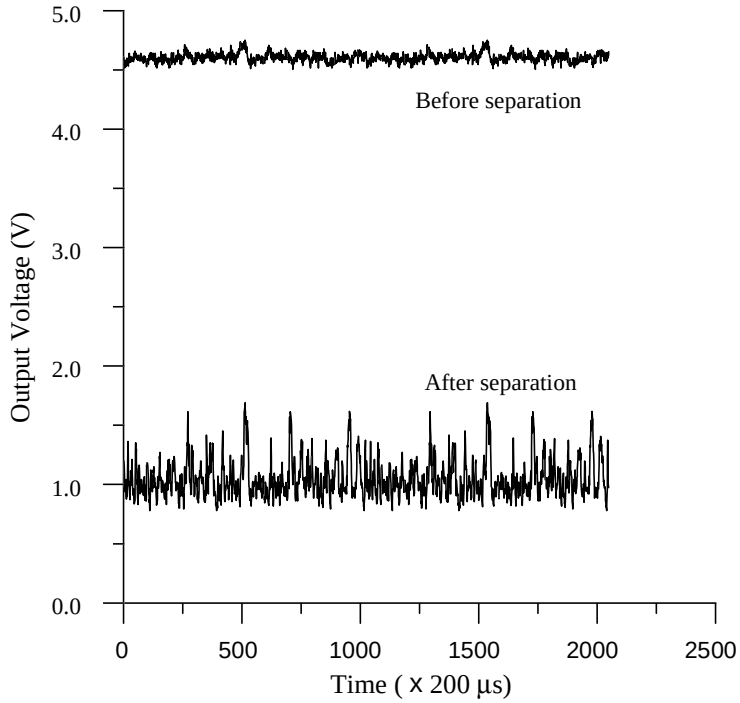

Figure 6.17 Output voltages (after gain of 10) from the sensors located before and after the flow separation point at velocity of 30 m/s.

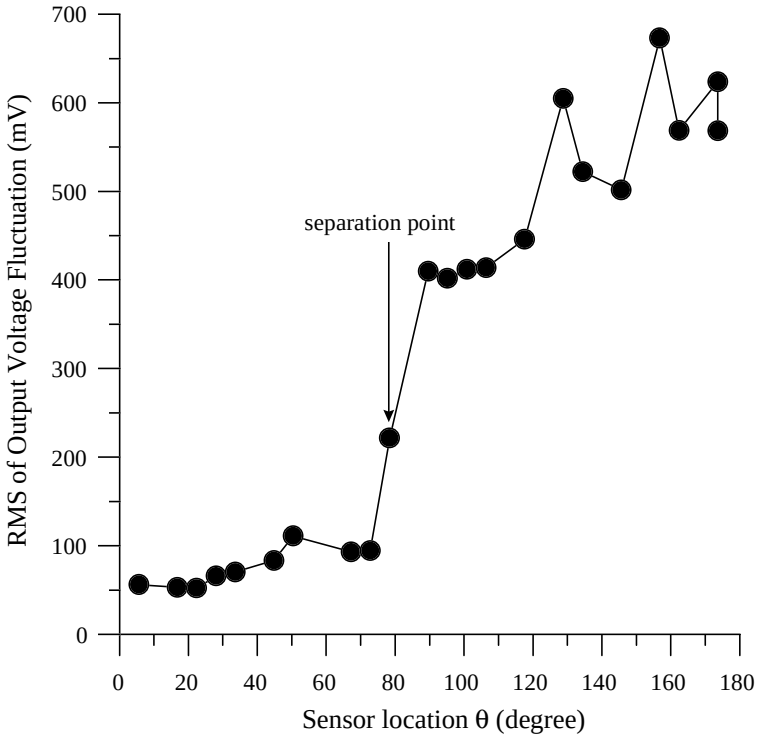

Figure 6.18 RMS fluctuation used to identify separation point.

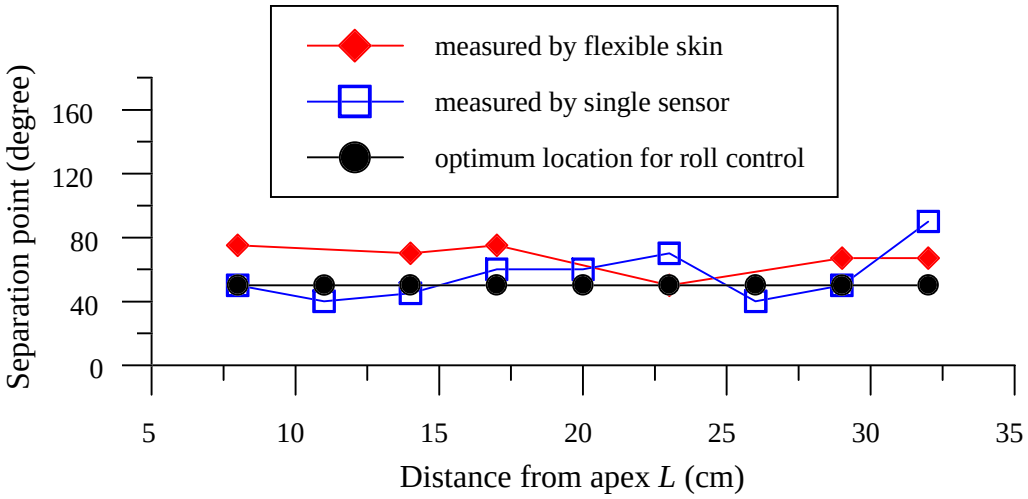

Figure 6.19 Comparison of separation lines measured by a single sensor and a flexible shear stress sensor array.

6.6 Sensor-Actuators Skin and Conformable M^3 System

The flexible MEMS technology has been applied to the fabrication of sensor-actuator skins. The sensors are the shear stress sensors and the actuators are the surface micromachined magnetic coil flap previously developed by the Caltech Micromachining Lab [20]. Figure 6.20 shows the layout of the sensor and actuator arrays on the 1×3 cm^2 skin. It has 1×36 sensors and 3×9 actuators. The purpose of the skin with this layout design is for the real-time control of the delta wing model in UCLA.

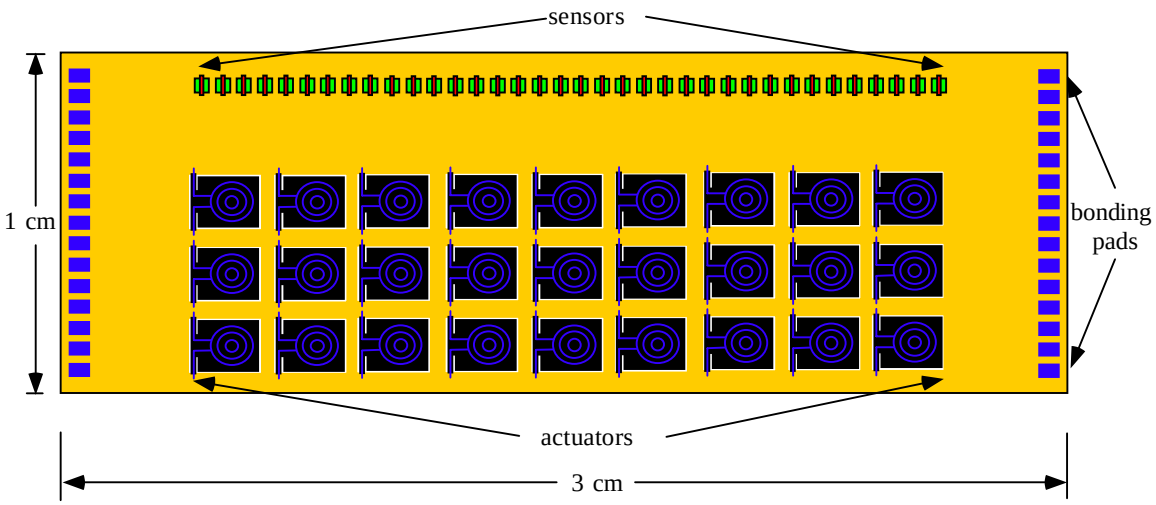

Figure 6.20 Layout design of the sensor-actuator skin for delta wing control.

Figure 6.21 the simplified fabrication process flow. Here, thick (2 μm) thermal silicon dioxide, instead of aluminum, is used as the etch stop in the final RIE etch step because aluminum can not be deposited under the flaps. This small change has actually caused some major problems. First, since the thermal oxide is grown on most of the front side but not on the backside, the wafer warpage caused by its intrinsic stress after the Si diapgram is formed becomes very serious. The solution is to grow thermal oxide on the backside. Second, as soon as the silicon under the flap area is removed by the final RIE etching, the flaps curl so badly due to the huge intrinsic stress that many of their torsional beams are broken. Figure 6.22 shown the sensor-actuator skin with the highest flap survival rate (80%) on a wafer. The solution is to spin-coat a few microns of polyimide

on the front side and bake the wafer at 150^{o}C for 30 min. before the RIE etching. The flaps are then protected against curling by the polyimide during and after the RIE etching. By first etching away the exposed oxide with BHF and then removing the protective polyimide with acetone/alcohol, the flaps are free-standing. However, even the surface flaps can survive the process, they are usually not robust in flow field and not very effective in flow control. The bulk flap is probably the better choice.

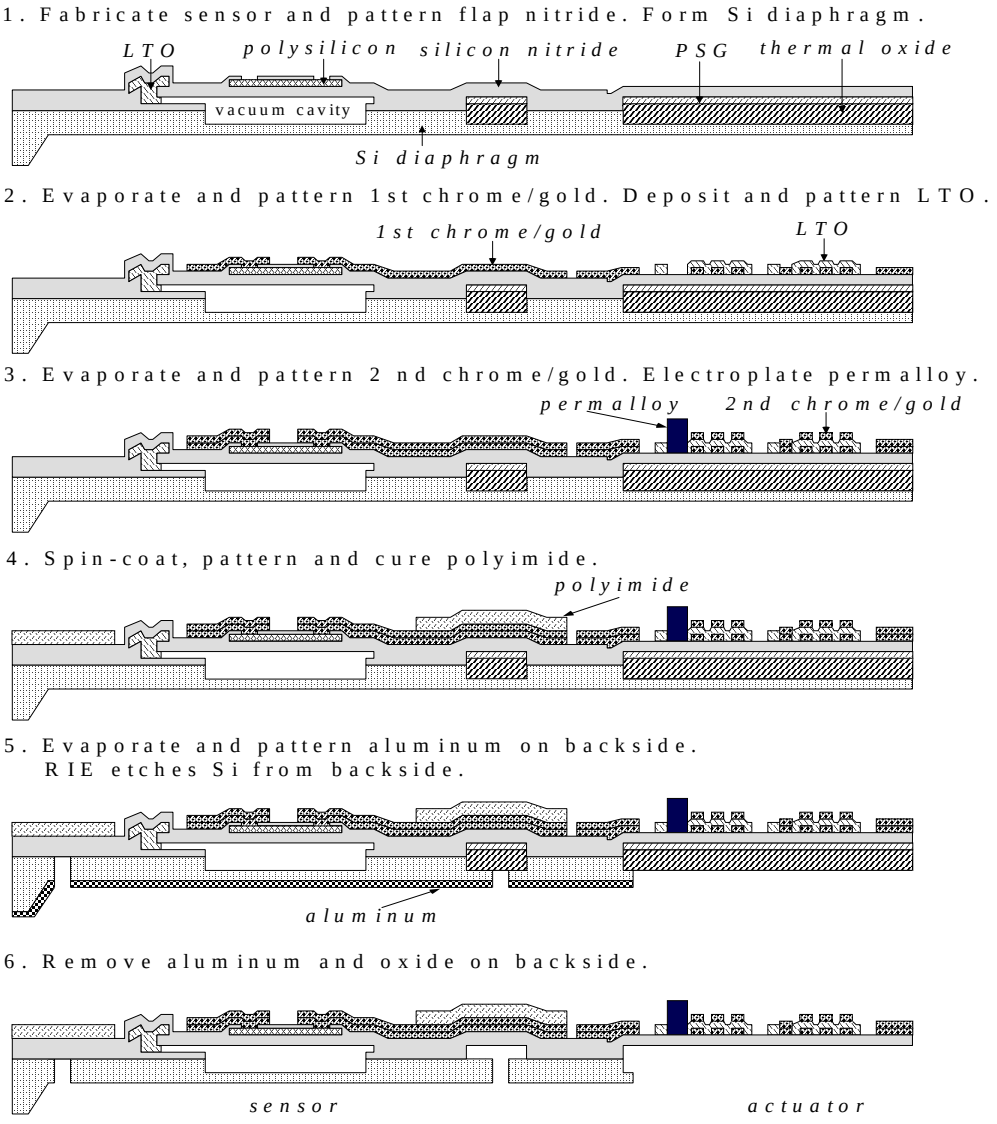

Figure 6.21 Simplified process flow for the sensor-actuator skin.

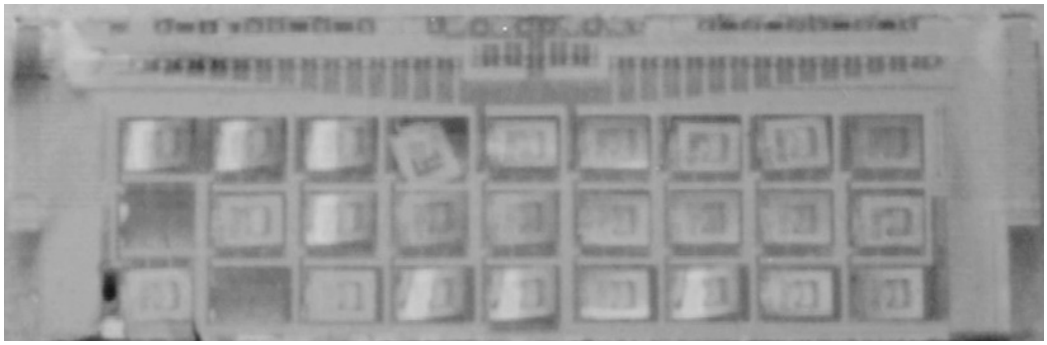

Figure 6.22 Picture of the best sensor-actuator skin on a wafer.

Finally, we propose the conformable M^3 system for delta wing control. Its cross-section is shown in Figure 6.23, which is basically the flexible skin version of the M^3 system for drag reduction described in Chapter 5. Here we have chosen the bulk micromachined flaps as the micro-actuators. The first polyimide layer serves as the inter-metal insulation for the flaps as well as the part of the flexible skin. It can be replaced by PSG or other inter-metal insulation materials with only a minor sacrifice on the robustness of the skin if it is not used by the IC manufacturers.

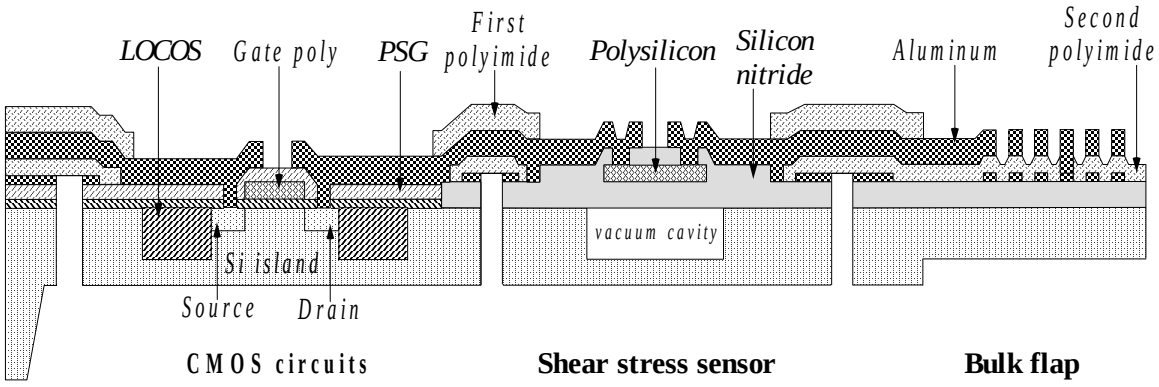

Figure 6.23 Cross-section of the proposed conformable M^3 system for delta wing control.

6.7 Summary

A novel flexible MEMS skin technology has been developed and it is fully compatible with IC process. The major lead failure occurred in previously reported technologies has been eliminated through the proper shaping of Si islands. Moreover, Si

islands as small as 100 μm can be defined with good accuracy, which allows the skins to be applied on small surfaces with large curvatures. The first application of this technology has produced a flexible shear stress sensor array that was successfully used in aerodynamics for the real-time measurement of shear stress distribution on 3-D surfaces.

Bibliography

[1] F. Jiang, Y.C. Tai, B. Gupta, R. Goodman, S. Tung, J.B. Huang, and C.H. Ho, "A Micromachined Shear Stress Sensor Array," *Proc. IEEE MEMS-96 Workshop*, San Diego, pp. 110-115, 1996.

[2] P.W. Barth, S. L. Bernard, and J. B. Angell, "Flexible Circuit and Sensor Arrays Fabricated by Monolithic Silicon Technology," *IEEE Trans. Electron. Devices*, Vol. ED-32 (7), pp. 1202-1205, 1985.

[3] D. J. Beebe and D. D. Denton, "A Flexible Polyimide-Based Package for Silicon Sensors," *Sensors and Actuators*, Vol. A44, pp. 57-64, 1994.

[4] C. Bang and T. Pan, "Flexible Heat Flux Sensor Arrays," *AFOSR Contractor and Grantee Meeting on Turbulence and Internal Flows*, Atlanta, Georgia, Sept. 1996.

[5] M. Mehregany, R. G. DeAnna, and E. Reshotko, "Microelectromechanical Systems for Aerodynamics Applications," AIAA Paper 96-0421, 1996.

[6] W. J. McCroskey and E. J. Durbin, "Flow Angle and Shear Stress Measurements using Heated Films and Wires," *ASME J. Basic Engineering*, Vol., pp. 46-52, 1972.

[7] H. H. Bruun, *Hot-Wire Anemometry: Principles and Signal Analysis*, Oxford University Press, p. 276, 1995.

[8] D. C. Reda, "Rise-Time Response of Nickel-Foil-on Kapton-Substrate, Hot-Film, Shear-Stress Sensors," AIAA Paper 91-0169, 1991.

[9] M. S. Wusk, D. L. Carraway, and B. J. Holmes, "An Arrayed Hot-Film Sensor for Detection of Laminar Boundary-Layer Flow Disturbance Spatial Characteristics," AIAA Paper 88-4677, 1988.

[10] J. P. Stack, S. M. Mangalam, and S. A. Berry, "A Unique Measurement Technique to Study Laminar-Separation Bubble Characteristics," AIAA Paper 87-1271, 1987.

[11] J. P. Stack, S. M. Mangalam, and V. Kalburgi, "The Phase Reversal Phenomenon at Flow Separation and Reattachment," AIAA Paper 88-0408, 1088.

[12] DuPont Electronic Materials, *PI-2808 Polyimide Product Information*, 1994.

[13] DuPont, *Kapton Polyimide film Productor Information*.

[14] B. Gupta, R. Goodman, F. Jiang, Y. C. Tai, S. Tung, and C. H. Ho, "Analog VLSI System for Active Drag Reduction," *IEEE Micro*, Vol. 16, No. 5, pp. 53-59, 1996.

[15] B. J. Bellhouse and D. L. Schultz, "Determination of Mean and Dynamic Skin Friction, Separation and Transition in Low-Speed Flow with a Thin-Film Heated Element," *J. Fluid Mech.*, Vol. 24, part 2, pp. 379-400, 1966.

[16] E. Achenbach, "Total and Local Heat Transfer from a Smooth Circular Cylinder in Cross-Flow at High Reynolds Number," *Int. J. Heat & Mass Transfer*, Vol. 18, pp.1387-1396, 1975.

[17] C. Liu, T. Tsao, Y. C. Tai, J. Leu, and C. H. Ho, "Out-of-Plane Permalloy Magnetic Actuators for Delta-Wing Control," *Proc. IEEE MEMS'95*, pp. 328-331, 1995.

[18] G. B. Lee, F. Jiang, T. Tsao, Y. C. Tai, and C. M. Ho, "Macro Aerodynamic Devices Controlled by Micro Systems," *IEEE Aerospace Conference*, Snowmass, Colorado, 1997.

[19] G. B. Lee, C. M. Ho, F. Jiang, C. Liu, T. Tsao and Y. C. Tai, "Distributed Flow Control by MEMS," *ASME 1996 International Mechanical Engineering Congress and Exposition*, Atlanta, Nov. 17-22, 1996.

[20] T. Tsao, F. Jiang, R. Miller, Y. C. Tai, B. Gupta, R. Goodman, S. Tung, and C. H. Ho, "An Integrated MEMS System for Turbulent Boundary Layer Control," *Transducers'97*, Chicago, pp. 315-318, 1997.

Appendix A

Description of Fabrication Processes

The detailed description of each fabrication process developed in the thesis is presented in this appendix.

A.1 Micromachined Hot-Wire Anemometer

1. Start with 4" (100) Si wafers with 70 μm epitaxial layer and 8 μm heavily boron-doped layer.
2. LPCVD low stress silicon nitride.
   2.1 Standard piranha wafer cleaning.
   2.2 Silicon nitride deposition: 835 ^{o}C, DCS 65 sccm, NH3 16 sccm, 30 min.. Target: 0.2 μm.
3. LPCVD LTO.
   3.1 Standard piranha wafer cleaning (omitted if immediately follow step #2).
   3.2 LTO deposition: 450 ^{o}C, SiH_4 42.8 sccm, O_2 62 sccm, 200 min.. Target thickness: 2 μm.
4. LPCVD polysilicon.
   4.1 Standard piranha wafer cleaning (omitted if immediately follow step #3).
   4.2 Polysilicon deposition: 560 ^{o}C, SiH_4 80 sccm, 170 min.. Target thickness: 0.55 μm.
5. Dope and anneal polysilicon.
   5.1 Boron ion implantation: energy 80 keV, dose 1×10^{16} cm^{-2}.
   5.2 Standard piranha wafer cleaning.

5.3 Annealing: 1050 ^{o}C, 1 hr..

6. Pattern polysilicon.
   6.1 Standard photolithography.
   6.2 RIE etching: SF_6 65 sccm, O_2 15 sccm, 600 W, 4 min. for both front and back side.
   6.3 Remove photoresist with acetone followed by plasma ashing.
7. Deposit metals.
   7.1 Standard piranha wafer cleaning.
   7.2 Evaporate 1 μm Cr/Au.
8. Pattern Cr/Au.
   8.1 Standard photolithography.
   8.2 Etch Au with gold etchant.
   8.3 Etch Cr with chrome etchant.
9. LPCVD LTO.
   9.1 TCE wafer cleaning.
   9.2 LTO deposition: 450 ^{o}C, SiH_4 42.8 sccm, O_2 62 sccm, 400 min.. Target thickness: 4 μm.
10. Pattern front side.
   10.1 Standard photolithography.
   10.2 Etch LTO with BHF: 0.2 μm/min.
   10.3 Plasma-etch nitride (from step #3): CF_4/O_2, 200 mT, 200 W, 4 min.. Target etching depth: 0.4 μm.
   10.4 Etch thermal oxide (from step #2) with BHF: 80 nm/min..
   10.5 Remove photoresist with acetone followed by plasma ashing.
11. Pattern backside.
   11.1 Standard piranha wafer cleaning.
   11.2 Standard photolithography on backside.
   11.3 Plasma-etch nitride (from step #3): CF_4/O_2, 200 mT, 200 W, 4 min.. Target etching depth: 0.4 μm.

11.4 Etch thermal oxide (from step #2) with BHF: 80 nm/min..

11.5 Remove photoresist with acetone followed by plasma ashing.

12. EDP etching.

12.1 Standard piranha wafer cleaning with 5% HF dip.

12.2 EDP etching: 95 ^{o}C, 10 hrs.

13. Boron layer, nitride and LTO removal.

13.1 TCE wafer cleaning.

13.2 RIE etching on wafer backside: SF_6 65 sccm, O_2 15 sccm, 600 W, 16 min..

13.3 BHF etching: 40 min..

A.2 Micromachined Shear Stress Sensor

1. Start with 4" single-side polished Si wafers.
2. LPCVD low stress nitride deposition.
   2.1 Standard piranha wafer cleaning.
   2.2 Silicon nitride deposition: 835 ^{o}C, DCS 65 sccm, NH3 16 sccm, 70 min.. Target: 0.5 μm.
3. Pattern nitride.
   3.1 Standard photolithography.
   3.2 Plasma etching: CF_4/O_2, 200 mT, 200 W, 6 min.. Target etching depth: 0.9 μm.
   3.3 Remove photoresist with acetone followed by plasma ashing.
4. Local oxidation (LOCOS).
   4.1 Standard piranha wafer cleaning.
   4.2 Thermal oxidation: 1050 ^{o}C, O_2 0.5 liter/min., DI water 10 drops/min., 12 hrs.. Target thickness: 2.1 μm.
   4.3 Planarization: BHF etches back.
5. LPCVD PSG.
   5.1 Standard piranha wafer cleaning.

5.2 PSG deposition: 450 ^{o}C, SiH_4 20 sccm, O_2 62 sccm, PH_3 10 sccm, 60 min.. Target thickness: 0.4 μm.

5.3 Anneal PSG: 950 ^{o}C, 30 min..

6. Pattern PSG.

6.1 Standard photolithography.

6.2 BHF etch PSG: 2.5 min..

6.3 Remove photoresist with acetone followed by plasma ashing.

7. Anneal PSG.

7.1 Standard piranha wafer cleaning.

7.2 Anneal PSG: 1050 ^{o}C, 30 min..

8. LPCVD low stress silicon nitride.

8.1 Standard piranha wafer cleaning (omitted if immediately follow step #8).

8.2 Nitride deposition: 835 ^{o}C, DCS 65 sccm, NH3 16 sccm, 180 min.. Target: 1.3 μm.

9. Pattern nitride to open etch holes.

9.1 Standard photolithography.

9.2 RIE etching: SF_6 65 sccm, O_2 15 sccm, 600 W, 20 min.. Target etching depth: 1.5 μm.

9.3 Remove photoresist with acetone followed by plasma ashing.

10. Sacrificial layer etching.

10.1 Standard piranha wafer cleaning.

10.2 High concentrion HF (49%) etches PSG and thermal oxide: 25 - 30 min..

10.3 DI water rinse: 20 min.. Spin dry.

11. Seal cavities in vacuum.

11.1 Standard piranha wafer cleaning.

11.2 Bake at 600 ^{o}C for 30 min..

11.3 LPCVD LTO deposition: 450 ^{o}C, SiH_4 42.8 sccm, O_2 62 sccm.Target thickness: 1 μm.

11.4 LPCVD low stress nitride deposition: 835 ^{o}C, DCS 65 sccm, NH3 16 sccm, 70 min.. Target: 0.5 μm.

12. Pattern sealing materials.
    12.1 Standard photolithography.
    12.2 Plasma-etch nitride: CF_4/O_2, 200 mT, 200 W, 6 min.. Target etching depth: 0.6 μm.
    12.3 BHF-etch LTO: 6 min..
    12.4 Remove photoresist with acetone followed by plasma ashing.
13. LPCVD polysilicon.
    13.1 Standard piranha wafer cleaning.
    13.2 Polysilicon deposition: 560 ^{o}C, SiH_4 80 sccm, 170 min.. Target thickness: 0.55 μm.
14. Dope and anneal polysilicon.
    14.1 Boron ion implantation: energy 80 keV, dose 1×10^{16} cm^{-2}.
    14.2 Standard piranha wafer cleaning.
    14.3 Annealing: 1050 ^{o}C, 1 hr..
15. Pattern polysilicon.
    15.1 Standard photolithography.
    15.2 RIE etching: SF_6 65 sccm, O_2 15 sccm, 600 W, 4 min..
    15.3 Remove photoresist with acetone followed by plasma ashing.
16. LPCVD low stress silicon nitride deposition.
    16.1 Standard piranha wafer cleaning.
    16.2 Nitride deposition: 835 ^{o}C, DCS 65 sccm, NH3 16 sccm, 30 min.. Target: 0.2 μm.

A.3 M^3 System

1. Start with p-type (100) Si wafer with resistivity of 8-12 Ω·cm.
2. Grow 0.1 μm SiO_2.

3. Define N well {CWN}.
4. Implant phosphorus with dose of $5\times10^{12}/cm^2$ at energy of 150 keV.
5. Drive-in well to 3.4 μm.
6. Grow 30nm SiO_2 (pad ox)
7. Deposit 0.1 μm silicon nitride.
8. Pattern silicon nitride to define active area (PR1) [Active] and LOCOS {CAA}.
9. Define p-field (PR2).
10. Implant boron with dose of $1.5\times10^{13}/cm^2$ at energy of 70 keV.
11. Grow LOCOS 0.65-0.7 μm.
12. Remove silicon nitride (from step #7).
13. Remove oxide (from 6 - pad ox).
14. Grow sac. oxide 20 nm.
15. Implant boron $1.7\times10^{12}/cm^2$ at energy of 30 keV.
16. Remove sac. oxide (from step #14).
17. Grow gate oxide 30nm.
18. Deposit 0.450 μm gate polysilicon [Poly].
19. Pattern gate polysilicon {CPG}.
20. Deposit cap. oxide 80 nm.
21. Deposit 0.45 μm cap. polysilicon [Poly2].
22. Pattern cap. polysilicon {CEL}.
23. Define N+ source and drain.
24. Implant arsenic with dose of $5\times10^{15}/cm^2$ at energy of 160 keV.
25. Anneal N+ source and drain.
26. Deposit 0.7 μm PSG.

*** Back to Caltech at this point ***

27. Pattern PSG (from step #26) [fberk_psg] {FEP}.

28. Deposit 0.4 μm PSG at 450 ^{o}C (SiH_4 20 sccm, O_2 62 sccm, PH_3 10 sccm).
29. Deposit 1 μm polysilicon at 620 ^{o}C (SiH_4 80 sccm, 140 A/min.).
30. Pattern polysilicon [tpoly] {TNP}.
31. Pattern PSG (from step #28) [fcaltech_psg] {NG}.
32. Deposit 1.3 μm low stress silicon nitride at 835 ^{o}C (DCS 64.7 sccm, NH3 15.6 sccm).
33. Pattern nitride to open etch holes [fhole_etch] {NS}.
34. Sacrificial layer (PSG and oxide) etching with 49% HF.
35. Deposit 1 μm LTO at 450 ^{o}C (SiH_4: 42.8, O2: 62 sccm).
36. Deposit 0.4 μm low stress silicon nitride at 835 ^{o}C.
37. Pattern silicon nitride [fseal_pad_nitride].
38. Etch LTO (from step #35).
39. Deposit 0.55 μm polysilicon at 560 ^{o}C (SH4 80sccm)
40. Implant boron on polysilicon with dose of 1×10^{16} cm-2 at energy of 80 keV;
41. Anneal polysilicon at 900 ^{o}C for 1 hour.
42. Pattern polysilicon [fpoly].
43. Deposit 0.2 μm low stress silicon nitride.
44. Pattern silicon nitride [fcontact] {NC}.
45. Pattern silicon nitride (from step #32) [fnitride] {FN}.
46. Define contact holes for electronics.
47. Etch contact holes (Berkeley).
48. Sputter 0.6 μm aluminum (Berkeley).
49. Define aluminum (Caltech).
50. Etch aluminum (Lam/plasma) [Metal1] {CMF} (Berkeley).
51. Sintering (Berkeley).
52. Pattern aluminum (wet etch) [fberk_metal] {NM}.
53. Pattern silicon nitride (from step #32) [tnitride_etch] {TNC}.
54. Deposit 2 μm LTO.

55. Pattern LTO [tlto_etch] {TNG}.
56. Evaporate 0.4 μm Cr/Au.
57. Pattern Cr/Au [tmetal1+] {TNM}.
58. Deposit o.5 μm LTO.
59. Pattern LTO [tlto2_etch] {TLYRL} <add to over sensor like LTO1>
60. Evaporate 0.4 μm Cr/Au.
61. Pattern Cr/Au [tmetal2+] {TNMS}.
62. Evaporate Cr/Cu seed layer.
63. Pattern seed layer [tplating] {TNS}.
64. Plate NiFe.
65. Protect NiFe [tcr_protect] {TLYRR}.
66. Remove seed layer.
67. Release actuators by TMAH and BrF_3 etching.

A.4 Flexible Shear Stress Sensor Array

1. Start with 4” double-side polished (100) Si wafers.
2. Make double-side alignment marks.
   2.1 Spin-coat and soft-bake 3 μm photoresist on both sides of wafers.
   2.2 Mount wafers on the double-side alignment jig. Flush-expose each side of a wafer under UV light.
   2.3 Develop photoresist.
   2.4 RIE etching: SF_6 65 sccm, O_2 15 sccm, 600 W, 15 min. for each side.
   2.5 Remove photoresist with acetone followed by plasma ashing.
3. LPCVD low stress nitride deposition.
   3.1 Standard piranha wafer cleaning.
   3.2 Silicon nitride deposition: 835 ^{o}C, DCS 64.7 sccm, NH3 15.6 sccm, 70 min.. Target: 0.5 μm.
4. Pattern nitride.

4.1 Standard photolithography.

4.2 Plasma etching: CF_4/O_2, 200 mT, 200 W, 6 min.. Target etching depth: 0.9 μm.

4.3 Remove photoresist with acetone followed by plasma ashing.

5. Local oxidation (LOCOS).

5.1 Standard piranha wafer cleaning.

5.2 Thermal oxidation: 1050 ^oC, O_2 0.5 liter/min., DI water 10 drops/min., 12 hrs.. Target thickness: 2.1 μm.

5.3 Planarization: BHF etches back.

6. LPCVD PSG.

6.1 Standard piranha wafer cleaning.

6.2 PSG deposition: 450 ^oC, SiH_4 20 sccm, O_2 62 sccm, PH_3 10 sccm, 60 min.. Target thickness: 0.4 μm.

6.3 Anneal PSG: 950 ^oC, 30 min..

7. Pattern PSG.

7.1 Standard photolithography.

7.2 BHF etch PSG: 2.5 min..

7.3 Remove photoresist with acetone followed by plasma ashing.

8. Anneal PSG.

8.1 Standard piranha wafer cleaning.

8.2 Anneal PSG: 1050 ^oC, 30 min..

9. LPCVD low stress silicon nitride.

9.1 Standard piranha wafer cleaning (omitted if immediately follow step #8).

9.2 Nitride deposition: 835 ^oC, DCS 64.7 sccm, NH3 15.6 sccm, 180 min.. Target: 1.3 μm.

10. Pattern nitride to open etch holes.

10.1 Standard photolithography.

10.2 RIE etching: SF_6 65 sccm, O_2 15 sccm, 600 W, 20 min.. Target etching depth: 1.5 μm.

10.3 Remove photoresist with acetone followed by plasma ashing.

11. Sacrificial layer etching.

11.1 Standard piranha wafer cleaning.

11.2 High concentrion HF (49%) etches PSG and thermal oxide: 25 - 30 min..

11.3 DI water rinse: 20 min.. Spin dry.

12. Seal cavities in vacuum.

12.1 Standard piranha wafer cleaning.

12.2 Bake at 600 ^{o}C for 30 min..

12.3 LPCVD LTO deposition: SiH_4 42.8 sccm, O_2 62 sccm. Target thickness: 1 μm.

12.4 LPCVD low stress nitride deposition: 835 ^{o}C, DCS 64.7 sccm, NH3 15.6 sccm, 70 min.. Target: 0.5 μm.

13. Pattern sealing materials.

13.1 Standard photolithography.

13.2 Plasma-etch nitride: CF_4/O_2, 200 mT, 200 W, 6 min.. Target etching depth: 0.6 μm.

13.3 BHF-etch LTO: 6 min..

13.4 Remove photoresist with acetone followed by plasma ashing.

14. LPCVD polysilicon.

14.1 Standard piranha wafer cleaning.

14.2 Polysilicon deposition: 560 ^{o}C, SiH_4 80 sccm, 170 min.. Target thickness: 0.55 μm.

15. Dope and anneal polysilicon.

15.1 Boron ion implantation: energy 80 keV, dose 1×1016 cm^{-2}.

15.2 Annealing: 1050 ^{o}C, 1 hr..

16. Pattern polysilicon.

16.1 Standard photolithography.

16.2 RIE etching: SF_6 65 sccm, O_2 15 sccm, 600 W, 4 min. for both front and back side.

16.3 Remove photoresist with acetone followed by plasma ashing.

17. LPCVD low stress silicon nitride deposition.
    17.1 Standard piranha wafer cleaning.
    17.2 Nitride deposition: 835 ^{o}C, DCS 64.7 sccm, NH3 15.6 sccm, 30 min.. Target: 0.2 μm.
18. LPCVD LTO and low stress silicon nitride.
    18.1 Standard piranha wafer cleaning (omitted if immediately follow step #17).
    18.2 LTO deposition: SiH_4 42.8 sccm, O_2 62 sccm. Target thickness: 1 μm.
    18.3 Nitride deposition: 835 ^{o}C, DCS 64.7 sccm, NH3 15.6 sccm, 100 min.. Target: 0.7 μm.
19. Pattern backside.
    19.1 Plasma-etch nitride: CF_4/O_2, 200 mT, 200 W, 9 min.. Target etching depth: 0.9 μm.
    19.2 BHF-etch LTO: 6 min..
    19.3 Standard photolithography (6 μm photoresist).
    19.4 RIE-etch nitride: SF_6 65 sccm, O_2 15 sccm, 600 W, 14 min.. Target etching depth: 0.9 μm.
    19.5 BHF-etch LTO: 6 min..
    19.6 RIE-etch nitride: SF_6 65 sccm, O_2 15 sccm, 600 W, 30 min.. Target etching depth: 1.9 μm.
    19.7 Remove photoresist with acetone followed by plasma ashing.
20. KOH etching.
    20.1 Standard piranha wafer cleaning with 5% HF dip.
    20.2 KOH etching: 58 ^{o}C, 20 hrs. Monitor remaining thickness closely after 16 hr. etching. Stop when it is 80 μm.
21. Remove nitride and LTO on the front side.
    21.1 Standard piranha wafer cleaning.
    21.2 Plasma-etch nitride: 9 min..

21.3 BHF-etch LTO: 6 min..

22. Evaporate aluminum.

22.1 Standard piranha wafer cleaning.

22.2 Evaporate 0.5 μm pure aluminum.

23. Pattern aluminum.

23.1 Standard photolithography.

23.2 Etch aluminum with aluminum etchant: 35 ^{o}C, 2 min..

23.3 Remove photoresist with acetone followed by plasma ashing.

24. Polyimide processing

24.1 TCE wafer cleaning.

24.2 Spin diluted VM-651 polyimide adhesion promoter water solution (0.5% - 1%) at 5 krpm/min..

24.3 Bake at 130 ^{o}C for 10 min..

24.4 Spin-coat polyimide PI-2808 at 4 krpm/min..

24.5 Bake at 130 ^{o}C for 15 min..

24.6 Standard photolithography. Polyimide etched during developing.

24.7 Remove photoresist by butyl acetate.

24.8 Cure polyimide: Ramp up from room temperature to 200 ^{o}C at a rate less than 4 ^{o}C/min.; Stay at 200 ^{o}C in air for 30 min.; ramp up to 350 ^{o}C at a rate less than 2.5 ^{o}C/min.; Stay at 350 ^{o}C with 10 liter/min. nitrogen purging for 1 hr.; Ramp down to room temperature at a rate less than 3 ^{o}C/min..

25. Open contact holes.

25.1 TCE wafer cleaning.

25.2 Standard photolithography.

25.3 RIE-etch nitride: SF_6 65 sccm, O_2 15 sccm, 600 W, 4 min.. Monitor closely.

25.4 Remove photoresist with acetone.

26. Metallization.

26.1 TCE wafer cleaning.

26.2 Evaporate 2.5 μm aluminum.

26.3 Standard photolithography.

26.4 Etch aluminum with aluminum etchant: 35 ^{o}C, 6 min..

26.5 Remove photoresist with acetone.

26.6 TCE wafer cleaning.

26.7 Evaporate 1 μm aluminum.

26.8 Standard photolithography.

26.9 Etch aluminum with aluminum etchant: 35 ^{o}C, 3.5 min..

26.10 Remove photoresist with acetone.

27. Polyimide processing (repeat step #24).

28. Form aluminum mask on backside.

28.1 TCE wafer cleaning.

28.2 Evaporate 0.5 μm pure aluminum on backside.

28.3 Standard photolithography (focus on Si diaphragm).

28.4 Etch aluminum with aluminum etchant: 35 ^{o}C, 2 min..

28.5 Remove photoresist with acetone.

29. Form Si islands.

29.1 TCE wafer cleaning.

29.2 RIE etching: SF_6 65 sccm, O_2 15 sccm, 600 W, 240 min.. Target etching depth: 80 μm. Monitor closed after 120 min. etching.

30. Strip aluminum on backside.

30.1 Spin-coat and bake 6 μm photoreist on front side.

30.2 Etch aluminum with aluminum etchant: 35 ^{o}C, 2 min..

31. Polyimide processing on backside (repeat steps #24.1-24.5 and #24.8, spin speed 2.0 krpm).

32. Cut finished skins from Si wafer frame using a razor blade.